NASA Technical Memorandum 85663

Reynolds Number Tests of an NPL 9510 Airfoil in the Langley 0.3-Meter Transonic Cryogenic Tunnel

Renaldo V. Jenkins
Langley Research Center
Hampton, Virginia

National Aeronautics
and Space Administration

**Scientific and Technical
Information Branch**

1983

INTRODUCTION

An airfoil having a maximum thickness to chord ratio of 0.11, a blunt trailing edge of 0.005 chord thickness, aft camber, and designed for a cruise lift coefficient of 0.6 at a Mach number above 0.75 was tested in the British National Physics Laboratory (NPL) 36 transonic wind tunnel (ref. 1). The airfoil tested was designed at the British NPL by combining a "peaky" upper-surface pressure distribution with rear loading. The airfoil, designated the NPL 9510, exhibited an unusual variation of drag coefficient with Mach number. (See ref. 1.) The chief problem was "drag creep," which is defined as a significant increase in drag occurring below the drag-rise Mach number. The data presented in reference 1 were obtained at low Reynolds numbers (2.65×10^6 to 3.65×10^6) and were thought to be Reynolds number sensitive. In order to determine the aerodynamic characteristics of this airfoil at higher values of Reynolds number as well as to determine the possible effects of condensation on this type of airfoil, a model of the NPL 9510 airfoil was tested at both low and high Reynolds numbers in the Langley 0.3-Meter Transonic Cryogenic Tunnel (0.3-m TCT).

SYMBOLS

Values are given in SI Units. Measurements and calculations were made in U.S. Customary Units.

c_p pressure coefficient, $\dfrac{p_l - p_\infty}{q_\infty}$

$c_{p,sonic}$ pressure coefficient for $M_l = 1$

c model chord, 152.4 mm

c_c section chord-force coefficient, $\oint c_p \, d\left(\frac{z}{c}\right)$

c_d section profile-drag coefficient, $\int_{Wake} c_d' \, d\left(\frac{h}{c}\right)$

c_d' point drag coefficient (ref. 2)

c_l section lift coefficient, $c_n \cos \alpha - c_c \sin \alpha$

c_m section pitching-moment coefficient about quarter-chord point,

$$-\oint c_p\left(\frac{x}{c} - 0.25\right) d\left(\frac{x}{c}\right) + \oint c_p\left(\frac{z}{c}\right) d\left(\frac{z}{c}\right)$$

c_n section normal-force coefficient, $-\oint c_p \, d\left(\frac{x}{c}\right)$

h vertical height in wake profile, mm

M Mach number

M_l local Mach number

M_∞ free-stream Mach number

p_l local static pressure, atm (1 atm = 101.325 kPa)

p_t total pressure, atm

p_∞ free-stream static pressure, atm

q_∞ free-stream dynamic pressure, atm

R Reynolds number based on model chord and free-stream conditions

T_t total temperature, K

x airfoil abscissa, mm

z airfoil ordinate, mm

α angle of attack, deg

Abbreviations:

AOA angle of attack (see fig. 2(a))

0.3-m TCT 0.3-Meter Transonic Cryogenic Tunnel

NPL National Physics Laboratory

APPARATUS AND TESTS

Model

The wind-tunnel model of the NPL 9510 had a chord of 152.4 mm (6.0 in.), a span of 201.42 mm (7.93 in.), and was constructed of HP 9-4-20 alloy steel. All pressure tubing was internal to the model. Fifty flush surface static pressure orifices were installed on the model in chordwise rows swept at 9.46°. The upper-surface row contained 32 orifices and the lower-surface row contained 18 orifices. The orifices were connected to a high-precision capacitive potentiometer-type pressure transducer (ref. 3) through a scanning valve system. The diameter of each orifice was 0.254 mm (0.010 in.) in order to minimize orifice-induced pressure errors. The coordinates of the model are presented in table I, and the shape is shown in figure 1. The model orifice locations are contained in table II. In general, the measured coordinates are within 0.0254 mm (0.001 in.) of the design values, and the surface finish is in the range of 0.102 to 0.203 μm (4×10^{-6} to 8×10^{-6} in.).

Langley 0.3-Meter Transonic Cryogenic Tunnel

The investigation was conducted in the Langley 0.3-Meter Transonic Cryogenic Tunnel (0.3-m TCT) with its 203.2- by 609.6-mm two-dimensional test section installed. This continuous-flow tunnel uses nitrogen gas as the test medium and can be operated over wide ranges of both pressure and temperature to obtain an extensive range of Reynolds number. For a 152.4-mm (6.0 in.) chord model, the 0.3-m TCT can obtain Reynolds numbers from 1.3×10^6 at a Mach number of 0.35 to greater than 45×10^6 at a Mach number of 0.80. Liquid nitrogen is injected into the tunnel circuit to control temperature in conjunction with independent control of pressure and fan speed to obtain this range of test conditions. Details on the cryogenic concept and the operation of the 0.3-m TCT are to be found in references 4 to 10. The validity of using cryogenic nitrogen as the test medium has been documented in references 8, 9, 11, and 12. Shown in figure 2 are the test section and other significant components of the 0.3-m TCT.

Wake Rake

The airfoil drag coefficient was determined by using a wake rake described in reference 13 and shown in figure 2(c). For the present tests, the rake contained five active pitot tubes. As viewed in figure 2(a), pitot tube 1 is 12.7 mm to the right of the tunnel midspan. Pitot tube 2 is on the tunnel midspan; tube 3 is 12.7 mm to the left of midspan; tube 4 is 38.1 mm to the left of midspan, and tube 5 is 50.8 mm to the left of midspan. The tubes had an outside diameter of 1.52 mm (0.06 in.) and an inside diameter of 1.02 mm (0.04 in.). The three static tubes of the wake rake were not used. However, nine static pressures were measured on the sidewall opposite the wake rake. The nine static pressure ports are arranged with one port midway between the tunnel floor and the ceiling and with four each, spaced 25.4 mm apart, above and below this midpoint. Both the pitot and static pressure measurements were made in a plane located 112 mm (0.736c) downstream of the trailing edge of the airfoil at zero angle of attack.

Tests and Methods

The test envelope for the 0.3-Meter Transonic Cryogenic Tunnel and the actual test points are depicted in figure 3. The upper boundary of the test envelope is fixed by a maximum total pressure of 6 atm and total temperatures (96.6 K to 106.6 K) which would give free-stream saturation at a given Mach number. The lower boundary is fixed by the maximum total temperature of 327 K at a total pressure of 1.2 atm. The Mach number for the present two-dimensional test section is limited to approximately 0.9. The filled-in symbol is the two-dimensional equivalent of the cruise point based on mean aerodynamic chord for a full-scale present-day wide-body transport. The flagged symbols at a Reynolds number of 30×10^6 and Mach number of 0.75 represent a special condensation effects study to be discussed later.

The model had 240-mesh carborundum-grit transition strips in place for all but one test at Reynolds numbers less than 6×10^6. These strips extended from 4 to 6 percent chord on the upper surface and from 6 to 8 percent chord on the lower surface to correspond to the locations of the strips in the NPL tests. The grit sizing and transition-strip placement was performed in accordance with the methods detailed in reference 14. The transition strips were placed in the following manner. The model was masked to expose the area intended for treatment. An adhesive was sprayed on the model, and the grit was then blown on the treated area to a coverage

of 5 to 10 percent. Once dried, the mask was removed, and any adhesive build-up that occurred along the mask edges was scraped off and polished to deter two-dimensional tripping.

The airfoil surface pressure distributions measured in the tests were numerically integrated to generate the normal-force coefficient and the quarter-chord pitching-moment coefficient.

These standard measurements were supplemented with wall static pressure measurements along both the floor and ceiling of the tunnel. These floor and ceiling measurements are designed to be used in conjunction with a wall interference correction method described in references 15, 16, and 17. The coefficient data presented herein, however, have not been corrected. Tube displacement effect correction has not been included in the airfoil drag coefficients presented herein.

PRESENTATION OF RESULTS

The integrated values of normal-force coefficient c_n, quarter-chord pitching-moment coefficient c_m, and profile-drag coefficient c_d are given herein. Because the variation in drag coefficient across the tunnel, as determined with the five individual pitot tubes, is slight until drag rise is reached, only the drag coefficient derived from the midspan tube (tube 2) is presented.

The uncorrected data are presented as plots of angle of attack α, profile-drag coefficient c_d, and quarter-chord pitching-moment coefficient c_m versus normal-force coefficient c_n. An index to the data figures follows:

Reynolds number, R	Mach number, M	p_t, atm	T_t, K	Figure
1.36×10^6	0.3511	1.20	300	4(a)
1.49	.3913	↓	↓	4(b)
1.86	.5005			4(c)
1.99	.5492			4(d)
2.11	.5974			4(e)
2.23	.6474			4(f)
2.20	.4019		227	5(a)
2.66	.4991		↓	5(b)
3.06	.5991			5(c)
3.38	.6974			5(d)
3.44	.7156			5(e)
3.49	.7358			5(f)
3.55	.7553			5(g)
3.60	.7763	↓	↓	5(h)
3.60	.6977	1.69	280	6(a)
6.27	.3989	3.47	230	6(b)
7.02	.3980	3.91	↓	7(a)
7.07	.4986	3.25		7(b)
6.99	.5960	2.83		7(c)
7.04	.6944	2.56	↓	7(d)

Reynolds number, R	Mach number, M	p_t, atm	T_t, K	Figure
7.03×10^6	0.7143	2.51	230	7(e)
7.02	.7338	2.48	↓	7(f)
7.02	.7527	2.44	↓	7(g)
7.04	.7729	2.40	↓	7(h)
7.04	.7925	2.37	↓	7(i)
7.06	.8096	2.34	↓	7(j)
15.02	.3977	5.57	170	8(a)
14.94	.4975	4.59	↓	8(b)
14.89	.5968	3.99	↓	8(c)
14.88	.6933	3.59	↓	8(d)
14.94	.7133	3.53	↓	8(e)
14.98	.7336	3.48	↓	8(f)
15.25	.7536	3.48	↓	8(g)
14.48	.7727	3.37	↓	8(h)
14.94	.7921	3.34	↓	8(i)
14.90	.8112	3.28	↓	8(j)
30.03	.4993	5.57	120	9(a)
30.13	.5987	4.84	↓	9(b)
30.20	.6970	4.31	↓	9(c)
30.09	.7145	4.27	↓	9(d)
30.04	.7351	5.29	140	9(e)
29.62	.7575	2.86	94	9(f)
30.07	.7561	5.21	140	9(g)
29.88	.7743	4.08	120	9(h)
30.03	.7933	4.01	120	9(i)
30.04	.8155	3.97	120	9(j)
47.63	.6990	5.81	107	10(a)
47.72	.7188	5.71	↓	10(b)
47.60	.7366	5.60	↓	10(c)
47.55	.7580	5.50	↓	10(d)
47.47	.7763	5.43	↓	10(e)

DRAG CHARACTERISTICS

Free and Fixed Transition

The results of an investigation of fixing transition is presented in figure 11. The dashed line is a theoretical calculation (ref. 18) which assumes fully turbulent flow from the 1-percent-chord location rearward. These results would indicate that there is considerable laminar flow at a Reynolds number of 3.60×10^6. In addition, it appears that natural transition moves well forward for a Reynolds number of 7×10^6 or at most 10×10^6. This forward location of transition for the higher Reynolds numbers eliminates the need for transition fixing at these values of Reynolds number.

Effects of Reynolds Number

Drag polars.- Figure 12 is a summary plot for a Mach number of 0.755. For those Reynolds numbers where normal-force coefficient c_n is greater than 0.6, section drag coefficient c_d is greater than 0.016. This figure also shows the expected decrease in c_d with increase in Reynolds number. For $c_n = 0.18$, the difference in c_d between the 7.02×10^6 and 47.55×10^6 conditions is 0.0023. This value is comparable to the difference in computed skin frictions for a flat plate at these two Reynolds numbers.

Drag rise.- Cross-plotting the data of figures 4 to 10 at constant normal-force coefficient c_n and Reynolds number R allows an investigation of the effects of Reynolds number on drag-rise Mach number. Examples of this cross-plotting are presented in figure 13. If the definition that drag-rise Mach number is the Mach number for which $\frac{dc_d}{dM} = 0.1$ is applied, the drag rise occurs below $M = 0.65$ at $c_n = 0.35$ and below $M = 0.55$ at $c_n = 0.55$. There were insufficient data at $c_n = 0.55$ to cross-plot the data for 47.6×10^6; however, two test points are directly plotted.

PRESSURE DISTRIBUTIONS

Comparison of Data

A comparison of the present data with the NPL data of reference 1 is presented in figure 14. The drag values from NPL are slightly greater for c_n below 0.6 for the lower Mach numbers (fig. 14(a)) and below 0.5 for the higher Mach numbers (fig. 14(b)). Above c_n of 0.6 and 0.5 for the low and high Mach numbers, respectively, the present data have higher drag; however, there is variation in the drag coefficients measured across the tunnel under these high-lift test conditions. The quarter-chord pitching-moment coefficient has very similar characteristics for the present and reference data.

From the drag-coefficient and angle-of-attack curves (fig. 14), it is apparent that the two tunnels (the British NPL 36 and the Langley 0.3-m TCT) have quite different interaction between the tunnel walls and the model. This difference in wall interference is expected since the two tunnels have different geometries. The NPL 36 tunnel has a width of 355.6 mm, a height of 762 mm, and an open area ratio of 0.033. The 0.3-m TCT, on the other hand, has a width of 203.2 mm, a height of 609.6 mm, and an open area ratio of 0.05. This difference in interaction produces a difference in α of about 0.5° for c_n in the range of 0.35 to 0.55. This 0.5° difference is confirmed when pressure distributions are compared, as in figure 15, for the same values of c_n and M. In figure 15(a), the normal-force coefficient is 0.44, Mach number is 0.5, and Reynolds number is 2.6×10^6. The reference data have an angle of attack of 2.0°, and the present data have an angle of attack of 2.51°. Figure 15(b) gives a comparison for normal-force coefficient of 0.42, Mach number of 0.7, and Reynolds number of 3.3×10^6. The present data have an angle of attack of 2.00°, and the reference data have an angle of attack of 1.5°. In both cases, only the reference data are faired; the agreement in the pressure-distribution results is considered to be very good.

Comparison of Theory and Experiment

In figure 16, experimental and theoretical (ref. 17) pressure distributions are shown for Mach numbers in the midrange (0.7 to 0.78) and in the upper range (0.78 to 0.82). Test points in these two ranges were chosen for comparison because they fall very near the 30×10^6 Reynolds number curve of figure 13(b). The test points at a Mach number of 0.736 (fig. 16(a)) have a strong shock well forward on the airfoil. The theory of reference 17 has been used to produce the theoretical pressure distribution by specifying Mach number and normal-force coefficient. The agreement is rather good considering the fact that shock-wave entropy changes are not included in the theoretical computation. The upper-surface shock strength is underestimated; thus, the region immediately downstream of the shock is also incorrect. The test point at a Mach number of 0.792 (fig. 16(b)) has a slightly weaker shock farther back on the airfoil. In this case, the theory underestimated the strength and misplaced the location of the upper-surface shock and overpredicted the extent of the supersonic region for the lower surface. These two test points ($M = 0.736$ and $M = 0.792$) were then corrected for blockage by the program of reference 16 to obtain the free-air Mach number. These corrected Mach numbers and the measured normal-force coefficients were then specified to compute the pressure distributions. The results of these computations are shown in figure 17. The Mach number has been corrected to 0.726 from 0.736, and the angle of attack has been computed as 1.88° instead of 1.78° for the midrange case (geometric α being 2.47°). These are small corrections which make minimal changes in the computed pressure distribution. However, they are sufficient to improve the agreement for the lower surface and to slightly improve the predicted value of the strength of the upper-surface shock. In the upper-range case, the Mach number has been corrected to 0.777 from 0.792, and the angle of attack has been computed as 1.58° instead of 1.40° (geometric α being 2.23°). These corrections are slightly larger and make significant changes in the computed pressure distribution. The lower-surface computed distribution is now in excellent agreement with the experimental data. The computed shock strength and location are greatly improved for the upper surface. Note that values of both c_p and c_l have been corrected to take into account the corrected free-stream Mach number. The theoretical predictions corrected for Mach number and lift coefficient give slightly better agreement with the experimental data than the uncorrected predictions.

CONDENSATION

There is considerable benefit to be made in terms of increased Reynolds number capability and reduced operating cost if a cryogenic tunnel is operated as cold as possible. (See ref. 11.) This can be illustrated by referring to figure 18. The saturation curve labeled $M = 0$ is the combinations of total pressure p_t and total temperature T_t for which nitrogen will normally condense if held at static conditions. The curve labeled $M_\infty = 0.7568$ defines the conditions for which saturation would occur in the test section without a model present and with a free-stream Mach number of 0.7568. The curve labeled $M_l = 1.5$ defines the conditions for which saturation would occur when a local Mach number of 1.5 is reached on the model. The dashed line represents all of the possible combinations of total pressure and total temperature that yield a Reynolds number of 30×10^6 based on a 152.4-mm chord for this free-stream Mach number of 0.7568. The test point at 94 K and 2.86 atm (square symbol) is very close to free-stream saturation, and condensation may occur on the model in sufficient amounts to affect the aerodynamic characteristics. On the other hand, the test point at 140 K and 5.21 atm (circle symbol) is chosen such that a local Mach number of 2.18 on the model would be needed for condensation to even be

possible. This latter test point requires 2.22 times as much liquid nitrogen to maintain as does the former test point at 94 K and 2.86 atm. For these two sets of test conditions, the maximum local Mach number on the model was 1.5, and there are no apparent condensation effects for 94 K as indicated by the aerodynamic data presented in figures 19 and 20.

The significance of operating as cold as possible at the same Reynolds and Mach numbers without altering the aerodynamic data is an immediate reduction in operating cost. If it is possible to operate as close to the free-stream saturation curve (temperature wise) as the 94 K condition - but at higher pressure - without altering the aerodynamic data, the gain is in Reynolds number. For example, 101.5 K and 5.21 atm give a Reynolds number of 50×10^6 at a Mach number of 0.7568 (triangle symbol in fig. 18).

CONCLUSIONS

A set of aerodynamic data has been presented for an NPL 9510 airfoil. The test Reynolds number ranged from 1.34×10^6 to 48.23×10^6. Significant conclusions follow:

1. The drag creep detected by the British National Physics Laboratory (NPL) during previous tests at low Reynolds numbers is also present at high Reynolds numbers.

2. The section drag coefficient continued to decrease with Reynolds number to the highest Reynolds number covered during these tests.

3. The model was tested very close to free-stream saturation without altering the aerodynamic data by condensation effects.

4. The present tests produced the same pressure distribution as the previous NPL tests when normal-force coefficient, Mach number, and Reynolds number were matched. The geometric angle of attack between the previous and the present tests is different by about 0.5°.

Langley Research Center
National Aeronautics and Space Administration
Hampton, VA 23665
September 19, 1983

REFERENCES

1. Hall, D. J.; Quincey, V. G.; and Lock, R. C.: Some Results of Wind-Tunnel Tests on an Aerofoil Section (NPL 9510) Combining a 'Peaky' Upper Surface-Pressure Distribution With Rear Loading. C.P. No. 1292, British A.R.C., 1974.

2. Baals, Donald D.; and Mcurhess, Mary J.: Numerical Evaluation of the Wake-Survey Equations for Subsonic Flow Including the Effect of Energy Addition. NACA WR L-5, 1945. (Formerly NACA ARR L5H27.)

3. Bynum, D. S.; Ledford, R. L.; and Smotherman, W. E.: Wind Tunnel Pressure Measuring Techniques. AGARD-AG-145-70, Dec. 1970, pp. 13-16.

4. Goodyer, Michael J.; and Kilgore, Robert A.: The High Reynolds Number Cryogenic Wind Tunnel. AIAA Paper No. 72-995, Sept. 1972.

5. Kilgore, Robert A.: Design Features and Operational Characteristics of the Langley Pilot Transonic Cryogenic Tunnel. NASA TM X-72012, 1974.

6. Kilgore, Robert A.; Goodyer, Michael J.; Adcock, Jerry B.; and Davenport, Edwin E.: The Cryogenic Wind-Tunnel Concept for High Reynolds Number Testing. NASA TN D-7762, 1974.

7. Kilgore, Robert A.: Design Features and Operational Characteristics of the Langley 0.3-Meter Transonic Cryogenic Tunnel. NASA TN D-8304, 1976.

8. Ray, Edward J.; Kilgore, Robert A.; Adcock, Jerry B.; and Davenport, Edwin E.: Analysis of Validation Tests of the Langley Pilot Transonic Cryogenic Tunnel. NASA TN D-7828, 1975.

9. Adcock, Jerry B.: Real-Gas Effects Associated With One-Dimensional Transonic Flow of Cryogenic Nitrogen. NASA TN D-8274, 1976.

10. Ray, Edward J.; Ladson, Charles L.; Adcock, Jerry B.; Lawing, Pierce L.; and Hall, Robert M.: Review of Design and Operational Characteristics of the 0.3-Meter Transonic Cryogenic Tunnel. NASA TM-80123, 1979.

11. Reubush, David E.: Experimental Investigation To Validate Use of Cryogenic Temperatures To Achieve High Reynolds Numbers in Boattail Pressure Testing. NASA TM X-3396, 1976.

12. Hall, Robert M.; and Adcock, Jerry B.: Simulation of Ideal-Gas Flow by Nitrogen and Other Selected Gases at Cryogenic Temperatures. NASA TP-1901, 1981.

13. Ladson, Charles L.; and Kilgore, Robert A.: Instrumentation for Calibration and Control of a Continuous-Flow Cryogenic Tunnel. NASA TM-81825, 1980.

14. Braslow, Albert L.; Hicks, Raymond M.; and Harris, Roy V., Jr.: Use of Grit-Type Boundary-Layer-Transition Trips on Wind-Tunnel Models. NASA TN D-3579, 1966.

15. Kemp, William B., Jr.: Toward the Correctible-Interference Transonic Wind Tunnel. Proceedings - AIAA 9th Aerodynamics Testing Conference, June 1976, pp. 31-38.

16. Kemp, William B., Jr.: Transonic Assessment of Two-Dimensional Wind Tunnel Wall Interference Using Measured Wall Pressures. Advanced Technology Airfoil Research - Volume I, NASA CP-2045, Part 2, 1979, pp. 473-486.

17. Kemp, William B., Jr.: TWINTAN: A Program for Transonic Wall Interference Assessment in Two-Dimensional Wind Tunnels. NASA TM-81819, 1980.

18. Bauer, Frances; Garabedian, Paul; Korn, David; and Jameson, Antony: Supercritical Wing Sections II. Volume 108 of Lecture Notes in Economics and Mathematical Systems, Springer-Verlag, 1975.

TABLE I.- AIRFOIL COORDINATES

Upper Surface

x/c	z/c
.0000	-.00002
.0004	.00392
.0016	.00760
.0025	.00942
.0050	.01277
.0100	.01670
.0150	.01922
.0200	.02100
.0250	.02238
.0300	.02357
.0400	.02553
.0500	.02722
.0600	.02871
.0700	.03007
.0800	.03129
.0900	.03241
.1000	.03343
.1200	.03530
.1400	.03694
.1600	.03839
.1800	.03970
.2000	.04090
.2200	.04205
.2400	.04315
.2600	.04417
.2800	.04507
.3000	.04592
.3200	.04669
.3400	.04741
.3600	.04806
.3800	.04867

x/c	z/c
.4000	.04917
.4200	.04959
.4400	.04990
.4600	.05013
.4800	.05027
.5000	.05031
.5200	.05028
.5400	.05016
.5600	.04995
.5800	.04970
.6000	.04930
.6200	.04879
.6400	.04818
.6600	.04741
.6800	.04655
.7000	.04543
.7200	.04415
.7400	.04263
.7600	.04093
.7800	.03902
.8000	.03688
.8200	.03459
.8400	.03205
.8600	.02933
.8800	.02642
.9000	.02337
.9200	.02009
.9400	.01655
.9600	.01278
.9800	.00888
1.0000	.00490

TABLE I.– AIRFOIL COORDINATES – Concluded

Lower Surface

x/c	z/c
.0000	–.00002
.0004	–.00397
.0016	–.00795
.0025	–.00976
.0050	–.01353
.0100	–.01846
.0150	–.02201
.0200	–.02498
.0250	–.02753
.0300	–.02984
.0400	–.03388
.0500	–.03738
.0600	–.04043
.0700	–.04310
.0800	–.04547
.0900	–.04753
.1000	–.04940
.1200	–.05265
.1600	–.05759
.2000	–.06114
.2400	–.06340
.2800	–.06438
.3200	–.06408
.3607	–.06247
.4000	–.05962
.4400	–.05553
.4800	–.05036
.5200	–.04428
.5600	–.03762
.6000	–.03067
.6400	–.02373

x/c	z/c
.6800	–.01705
.7199	–.01064
.7600	–.00503
.8000	–.00047
.8400	.00299
.8800	.00475
.9200	.00485
.9600	.00322
1.0000	.00002

TABLE II.– ORIFICE LOCATIONS

Upper Surface

x/c	z/c
.00000	.00000
.00752	.01542
.01009	.01712
.01643	.02012
.02003	.02136
.02652	.02310
.03075	.02407
.03642	.02522
.05180	.02785
.07688	.03127
.10185	.03393
.15177	.03814
.20194	.04136
.25185	.04410
.30182	.04633
.40182	.04959
.45194	.05040
.50195	.05065
.52695	.05058
.55201	.05040
.57701	.05009
.60203	.04960
.62695	.04895
.65194	.04810
.67701	.04703
.70197	.04567
.75163	.04203
.80170	.03705
.85194	.03078
.90117	.02353
.95180	.01473
1 .00000	.00245

Lower Surface

x/c	z/c
.00000	.00000
.00997	–.01833
.01768	–.02362
.05263	–.03820
.10228	–.04976
.15266	–.05678
.20203	–.06125
.27703	–.06435
.37565	–.06150
.45068	–.05426
.52567	–.04337
.60065	–.03065
.67547	–.01770
.71730	–.01103
.85073	.00358
.90095	.00503
.95077	.00379
1 .00000	.00245

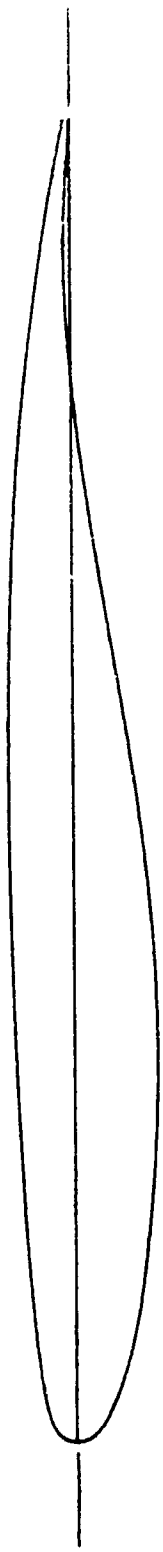

Figure 1.- Shape of the NPL 9510 airfoil.

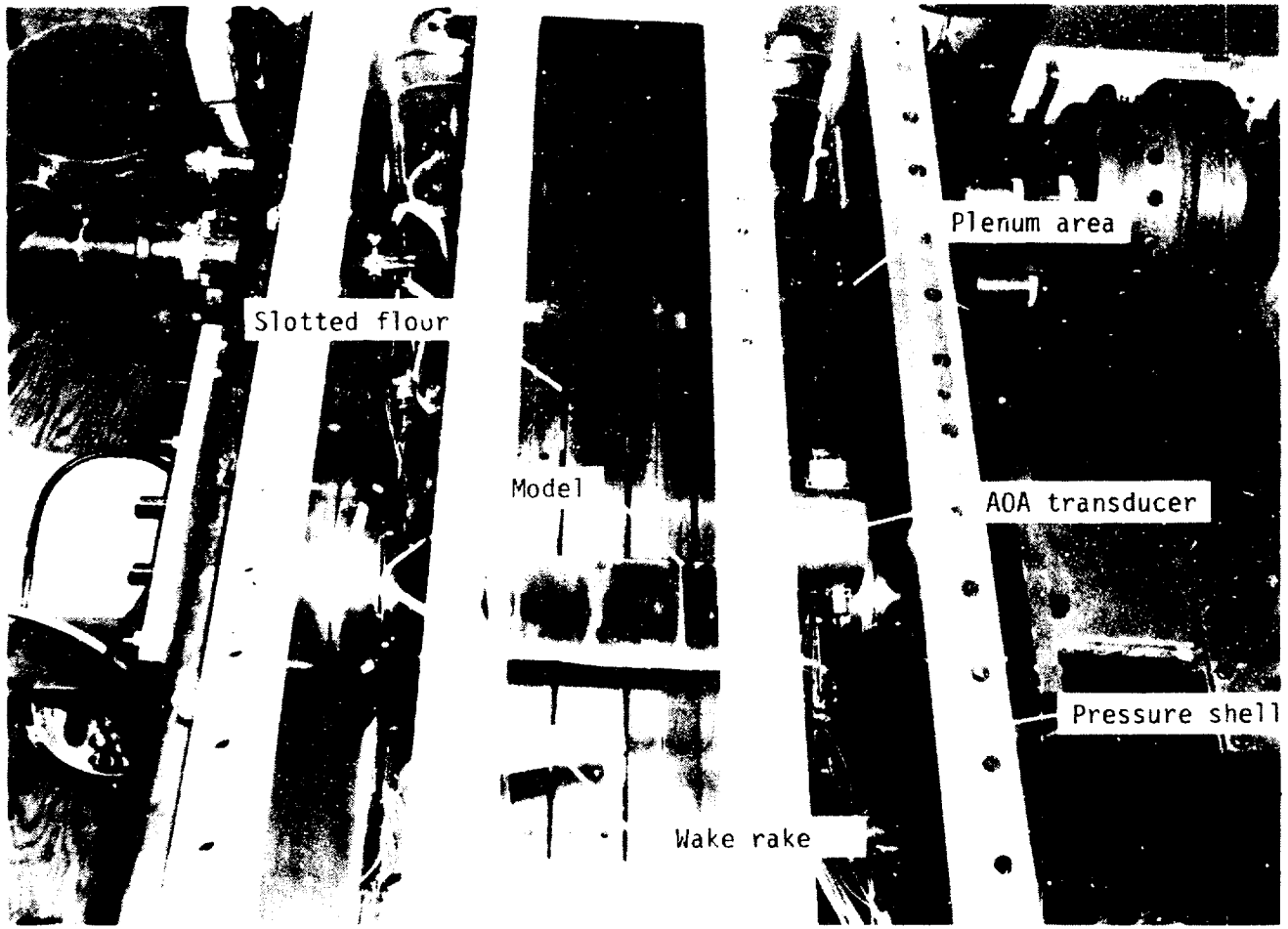

(a) Top view of test section.

Figure 2.- Test section and significant components of Langley 0.3-Meter Transonic Cryogenic Tunnel.

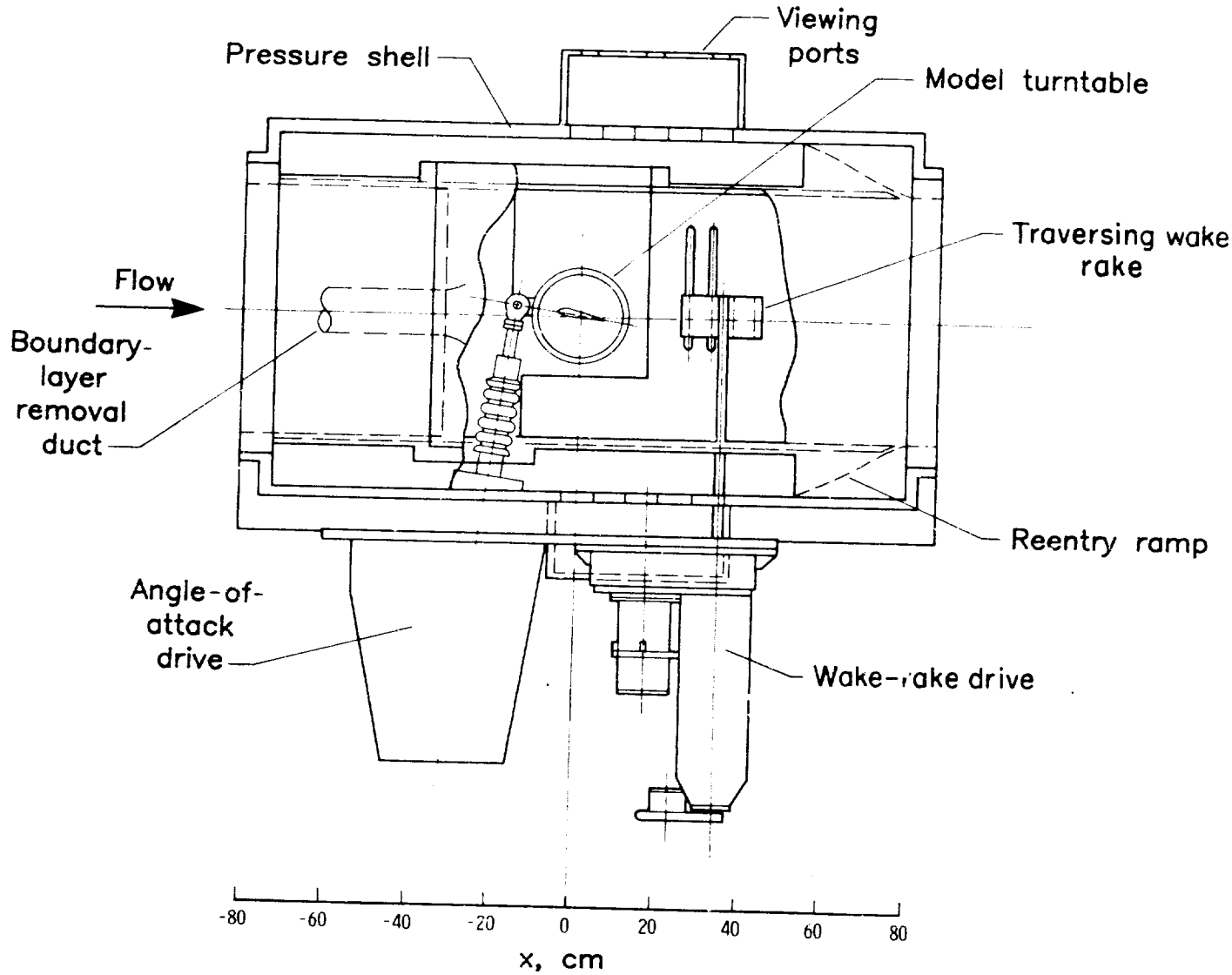

(b) Schematic drawing showing major components.

Figure 2.- Continued.

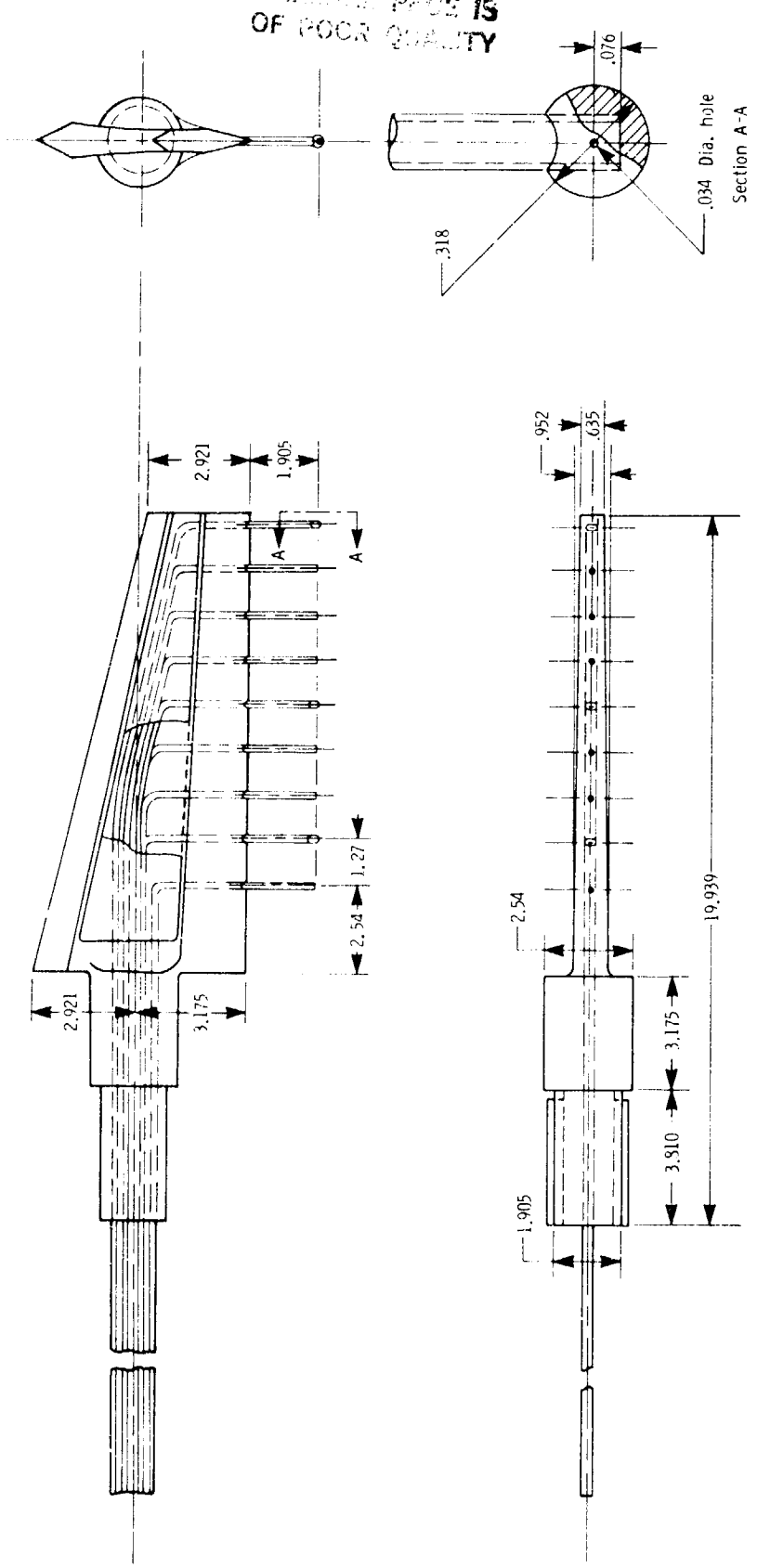

(c) Details of wake survey probe. All dimensions are in centimeters.

Figure 2.- Concluded.

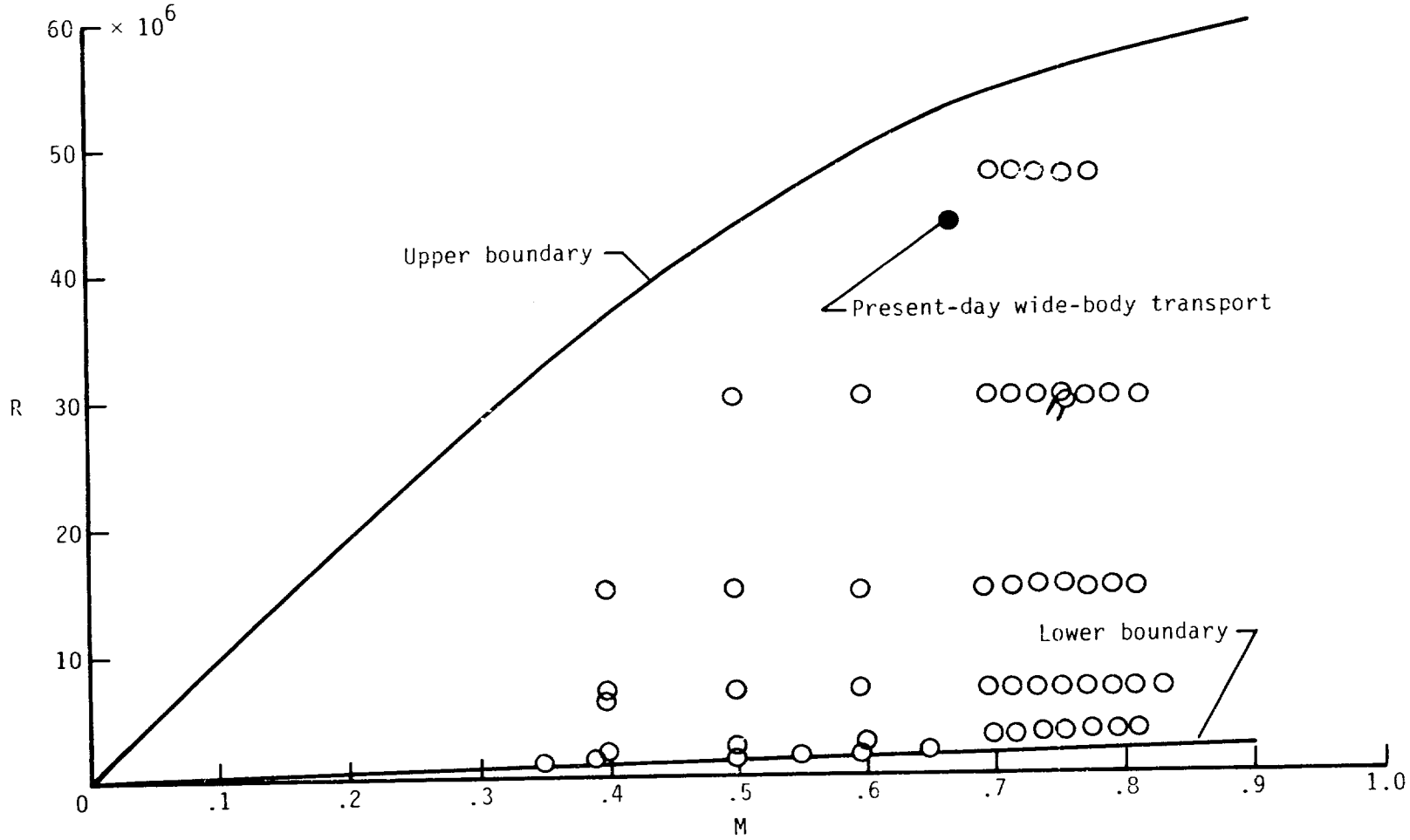

Figure 3.- The 0.3-m TCT test envelope and test points. (Flagged symbols represent special condensation effects study.)

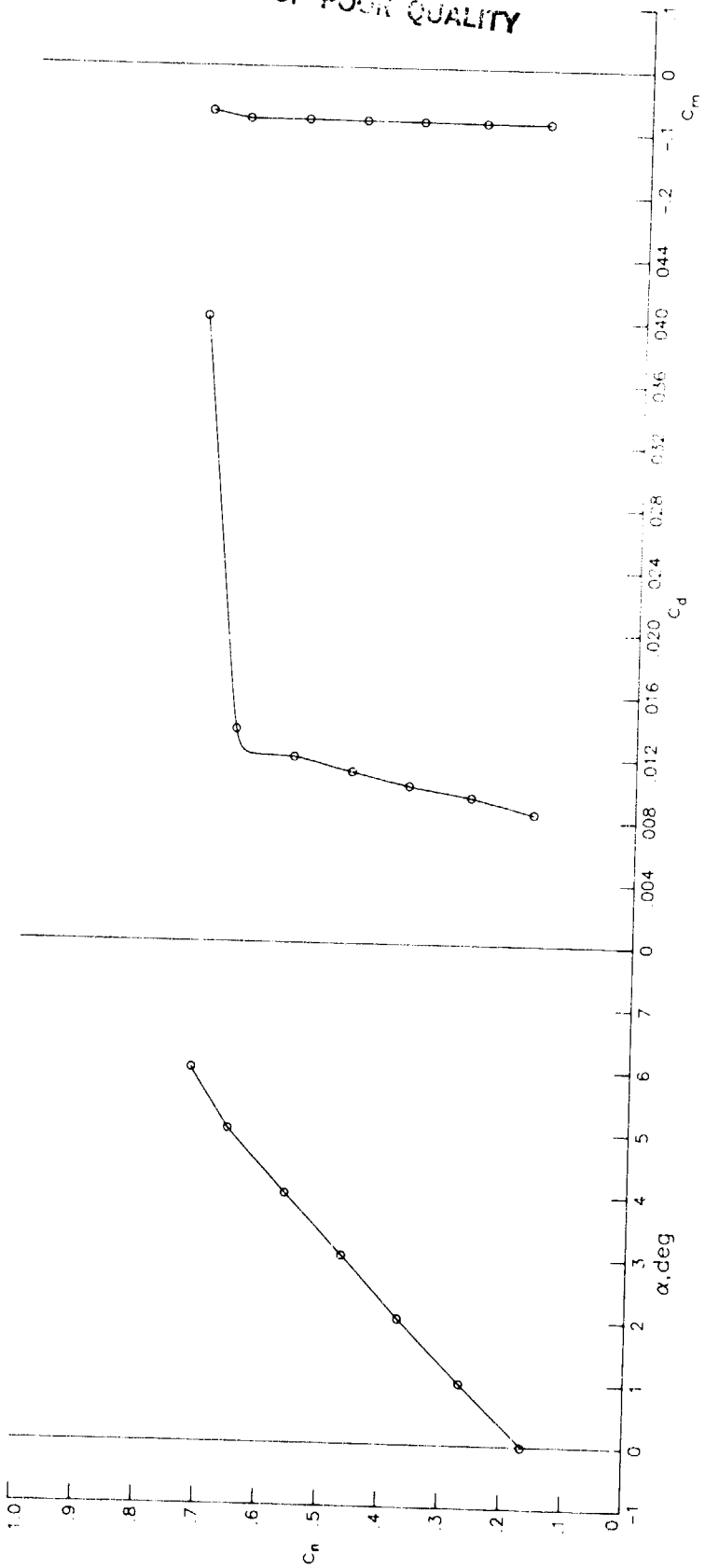

(a) R = 1.36 × 10^6; M = 0.3511.

Figure 4.- Section characteristics for various Reynolds numbers and Mach numbers with p_t = 1.20 atm, T_t = 300 K, and fixed transition.

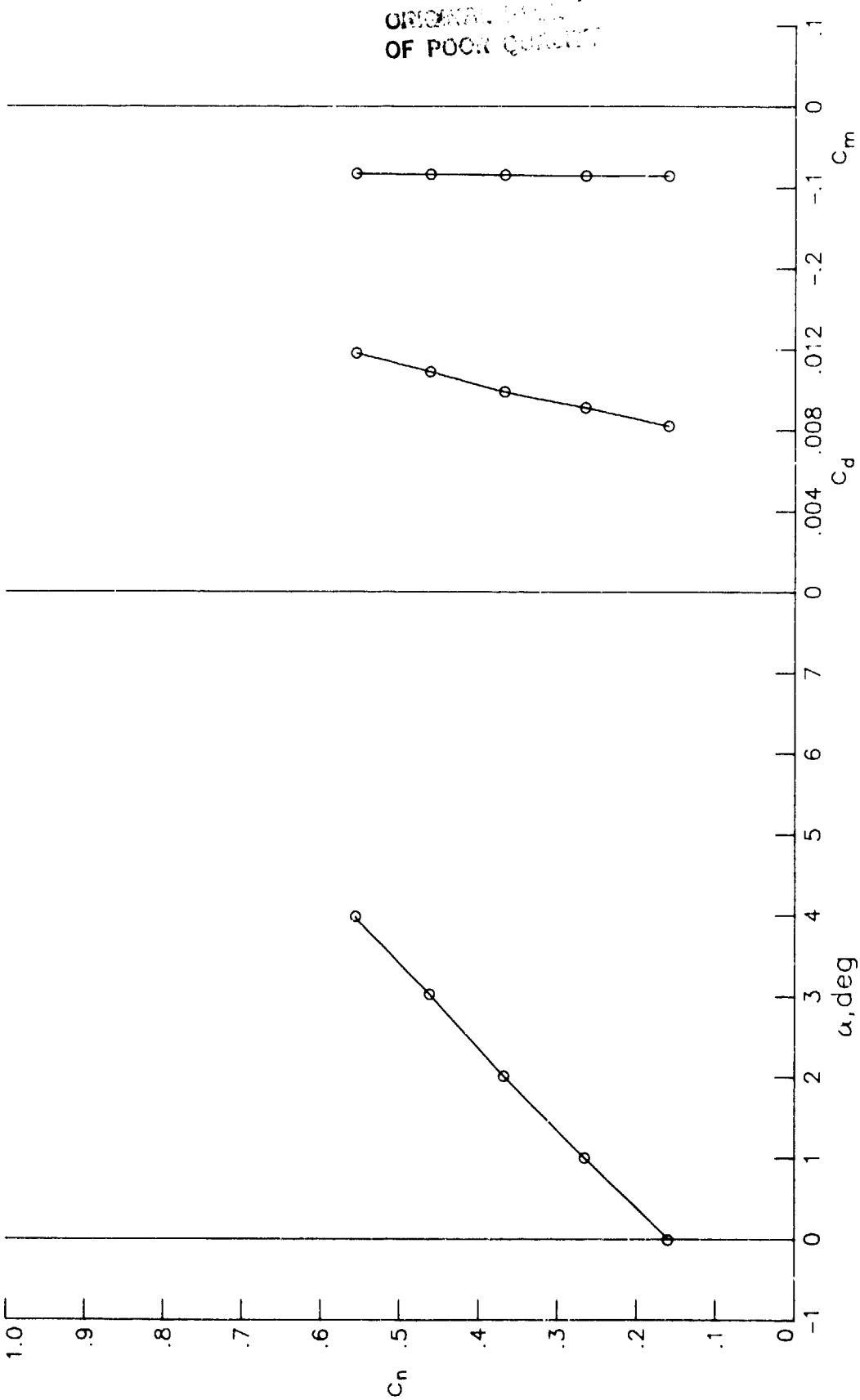

(b) R = 1.49 × 10^6; M = 0.3913.

Figure 4.- Continued.

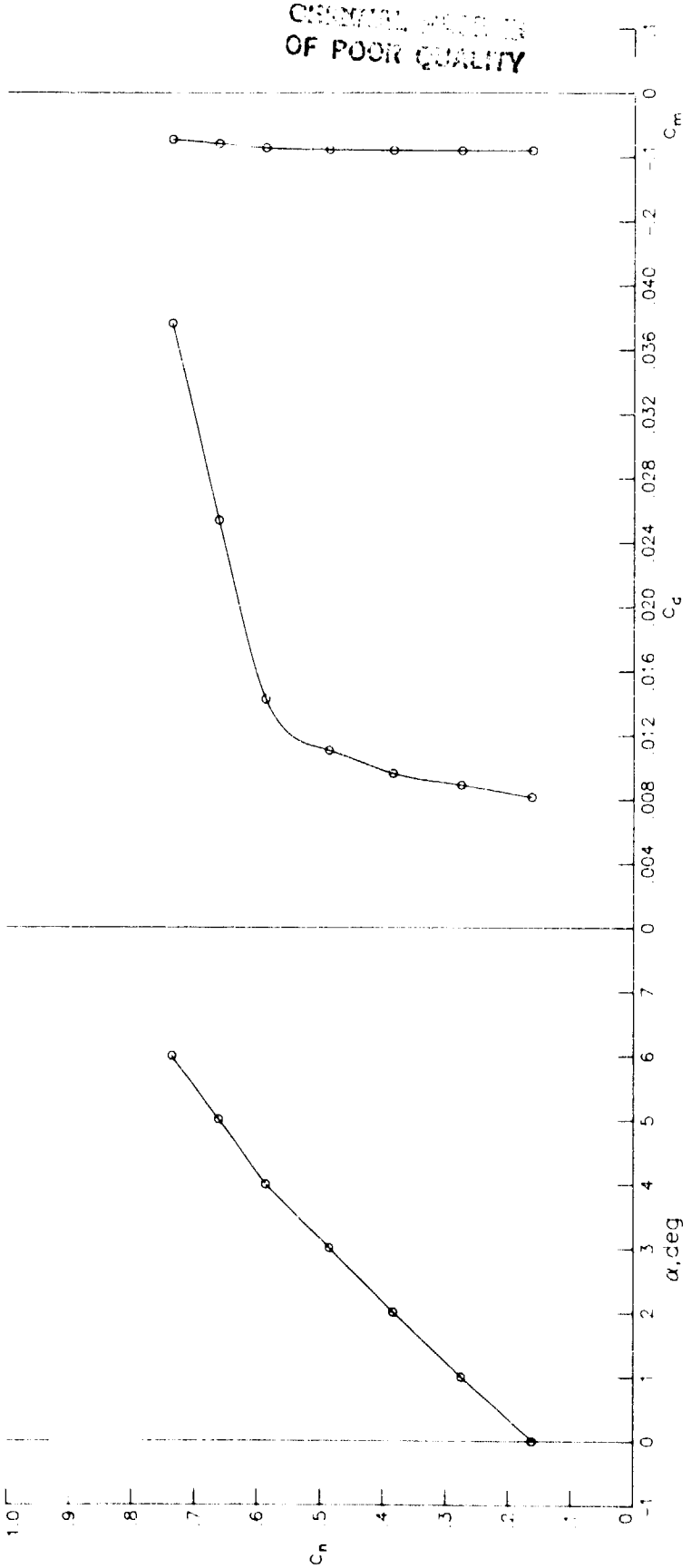

(c) R = 1.86 x 10^6; M = 0.5005.

Figure 4.- Continued.

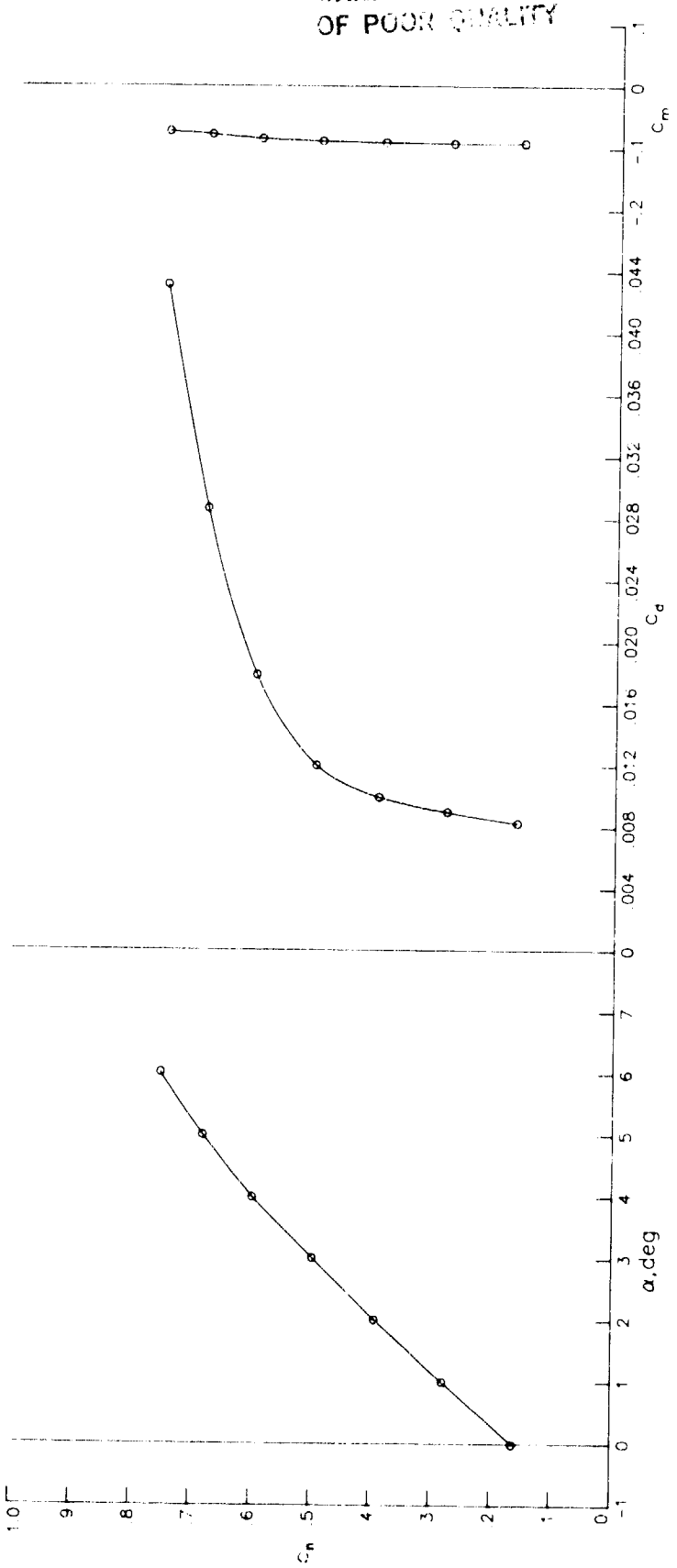

(d) R = 1.99 × 10^6; M = 0.5492.

Figure 4.- Continued.

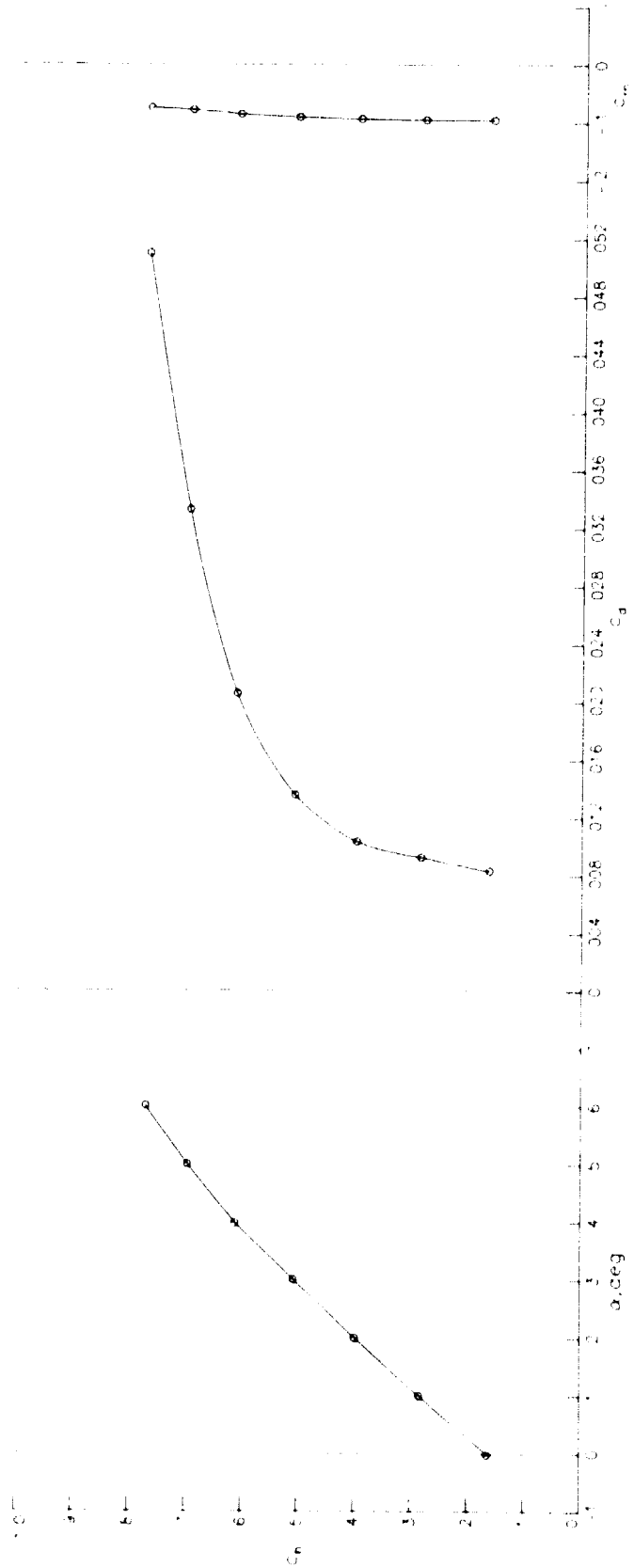

(e) $R = 2.11 \times 10^6$; $M = 0.5974$.

Figure 4.- Continued.

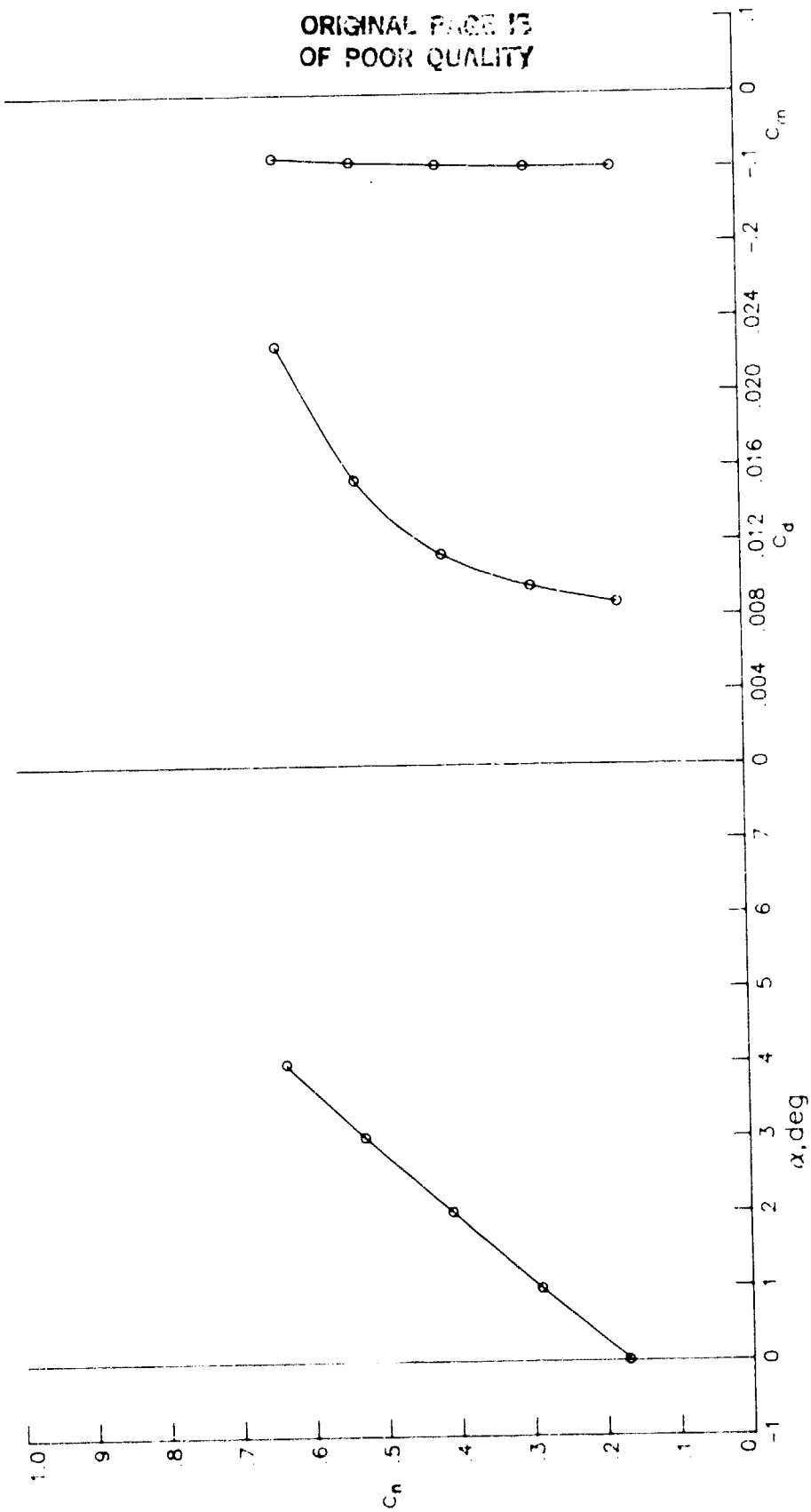

(f) R = 2.23 x 10^6; M = 0.6474.

Figure 4.- Concluded.

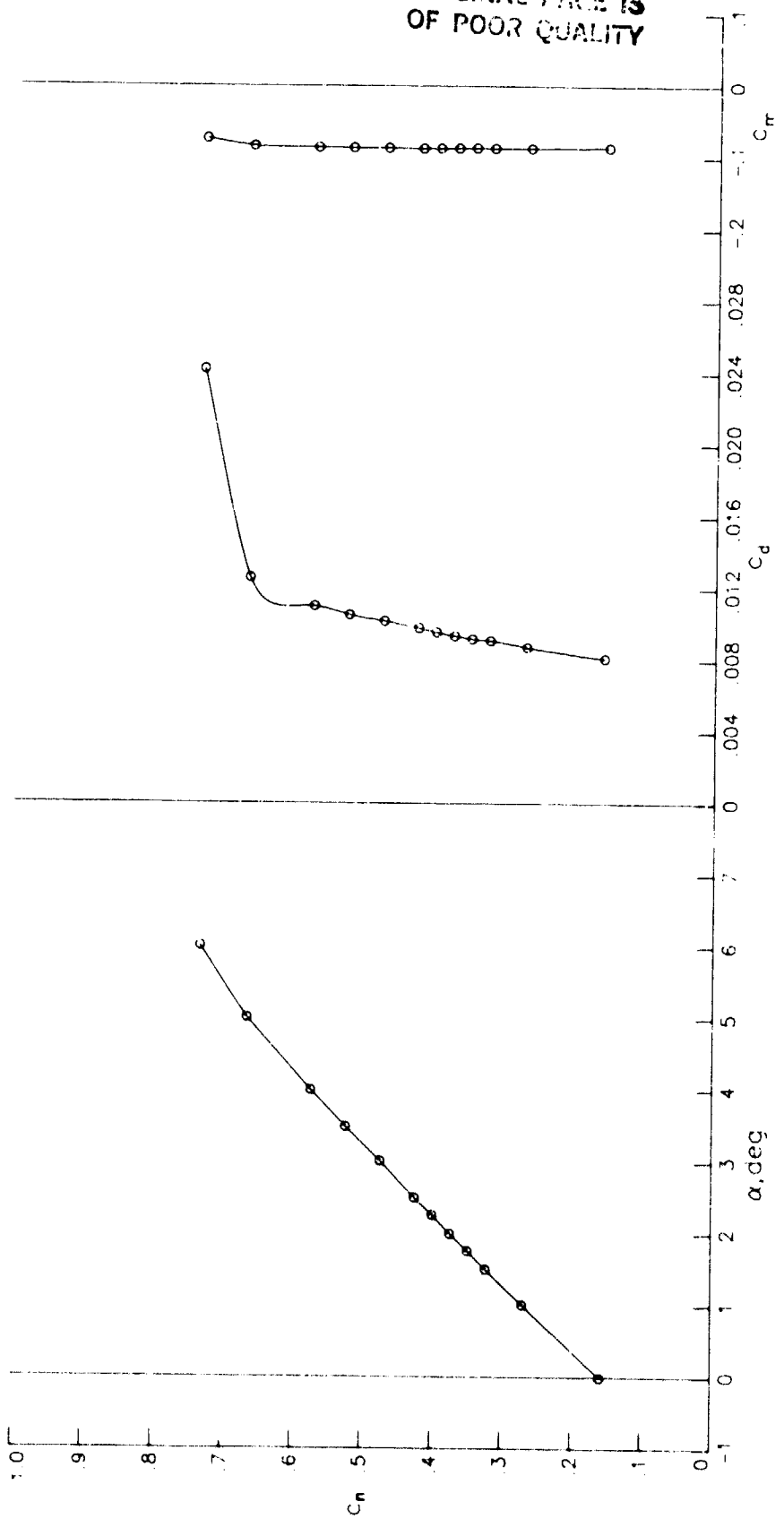

(a) R = 2.20 × 10^6; M = 0.4019.

Figure 5.- Section characteristics for various Reynolds numbers and Mach numbers with P_t = 1.20 atm, T_t = 227 K, and fixed transition.

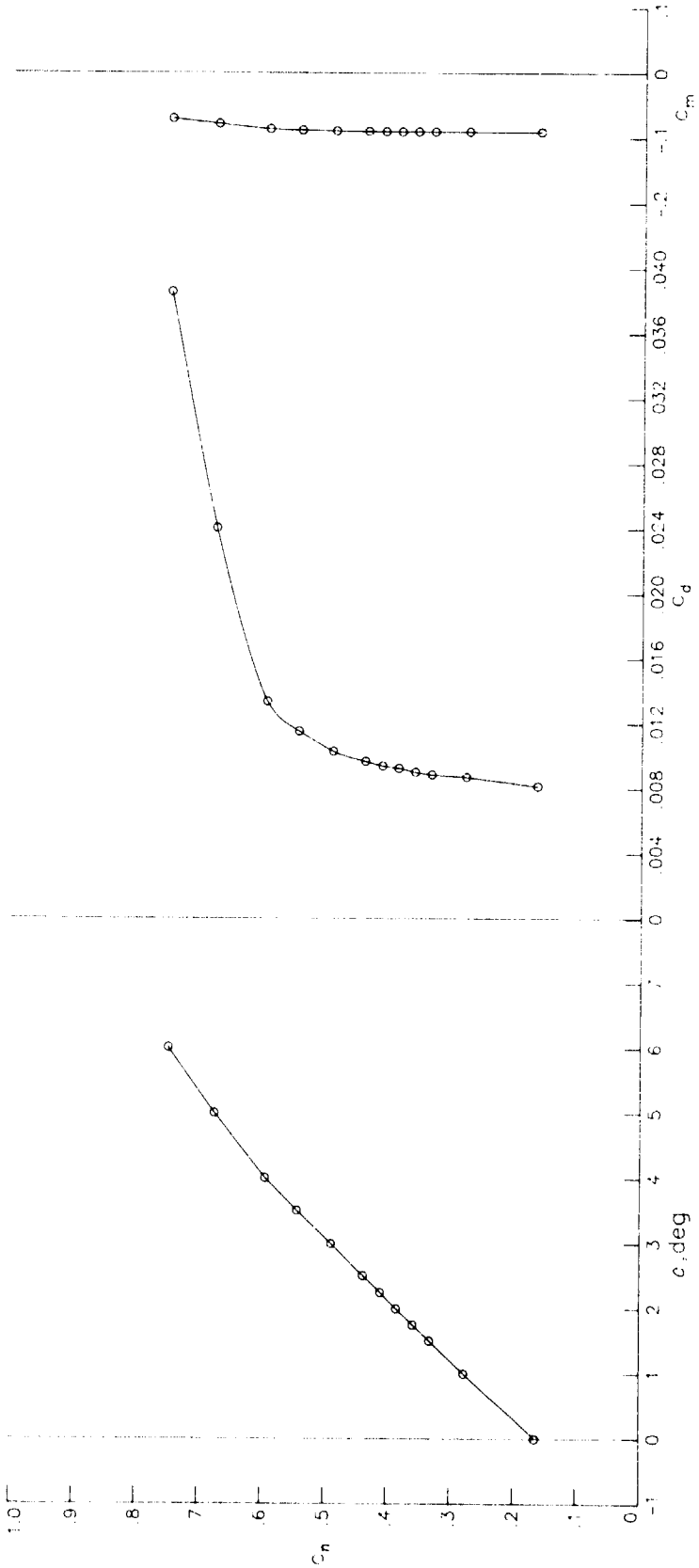

(b) R = 2.66 x 10^6; M = 0.4991.

Figure 5.- Continued.

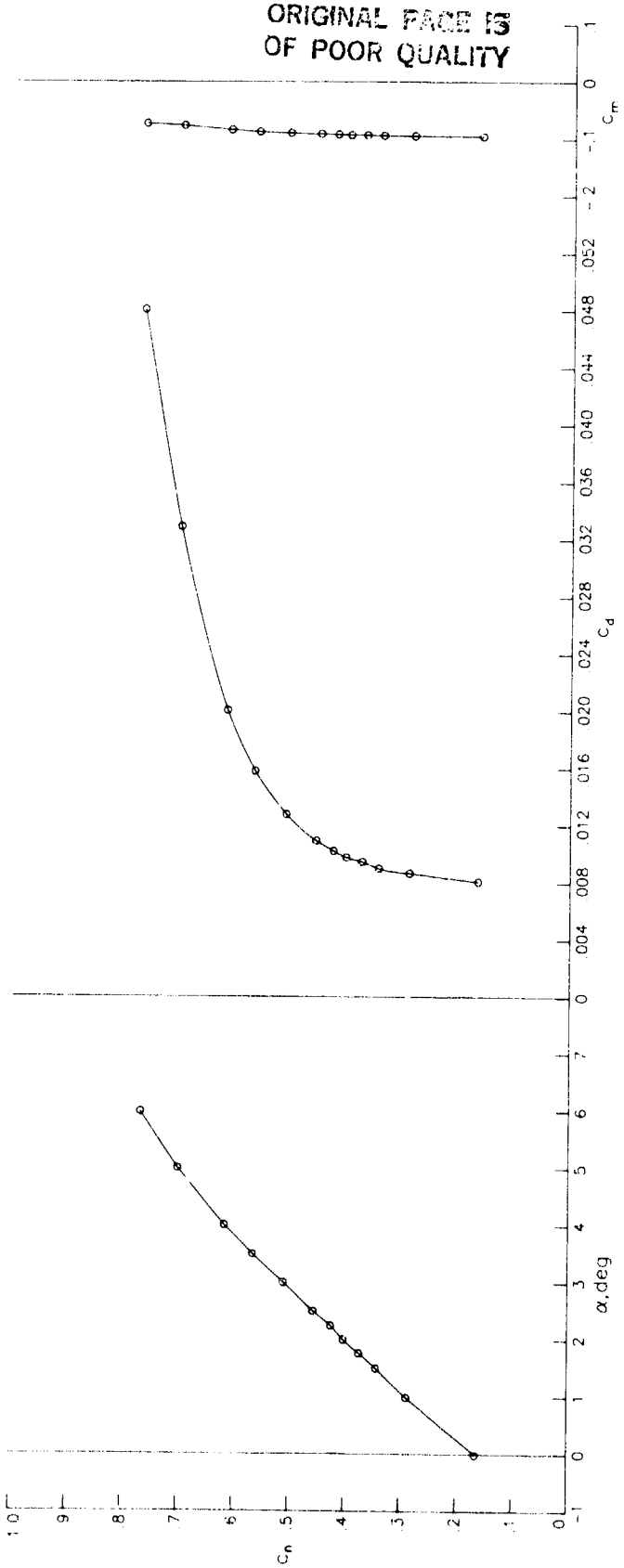

(c) R = 3.06×10^6; M = 0.5991.

Figure 5.- Continued.

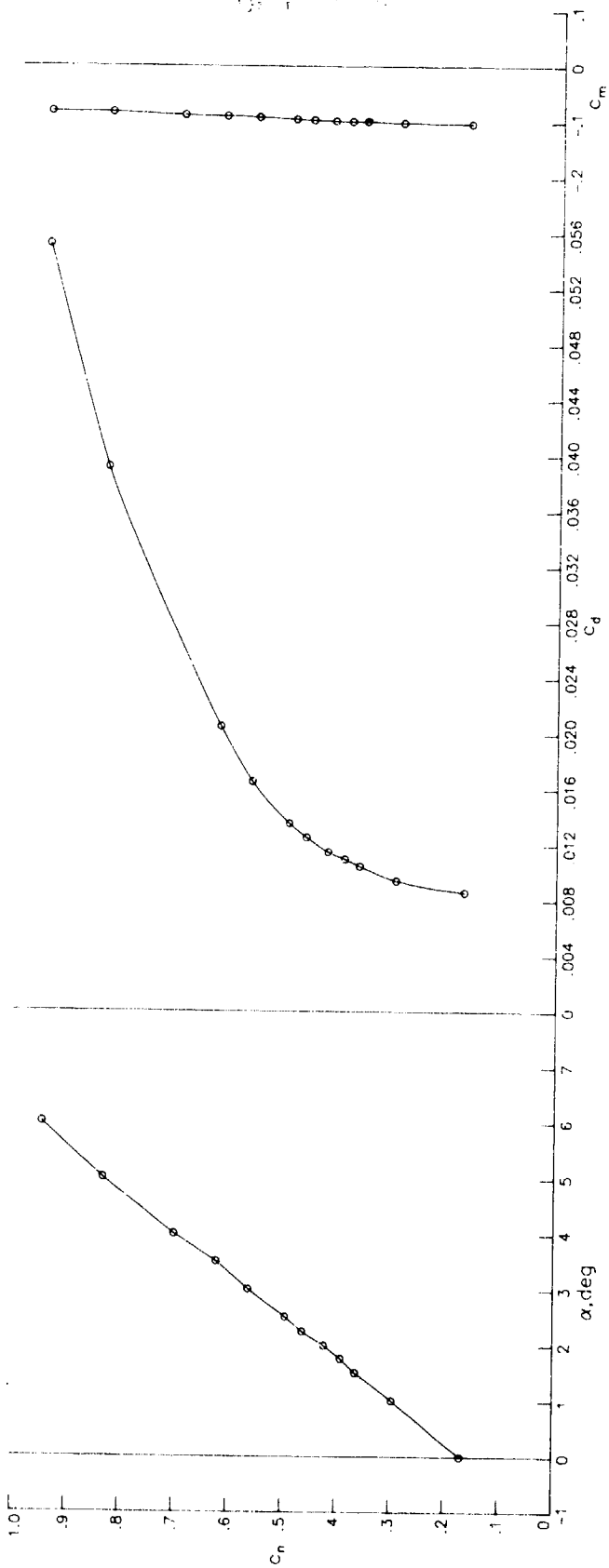

(d) R = 3.38 × 10^6; M = 0.6974.

Figure 5.- Continued.

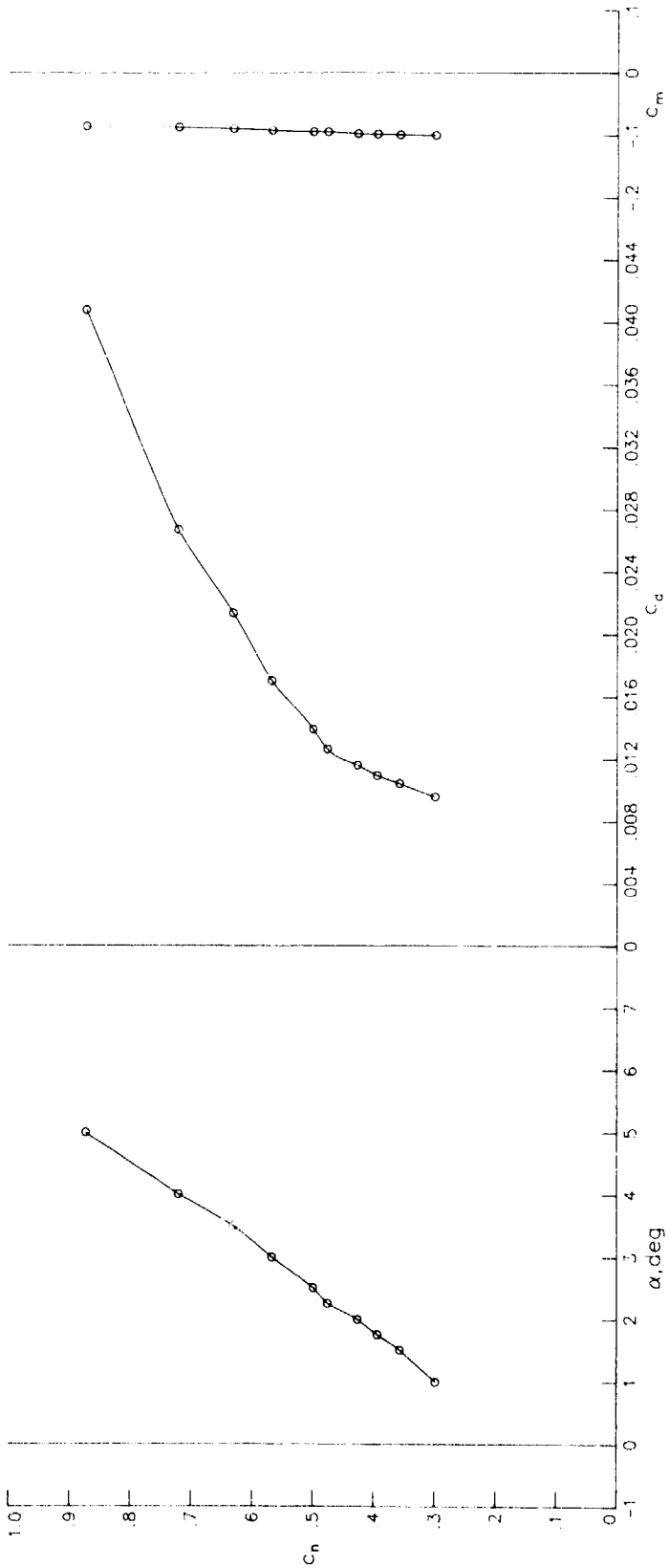

(e) R = 3.44 × 10^6; M = 0.7156.

Figure 5.- Continued.

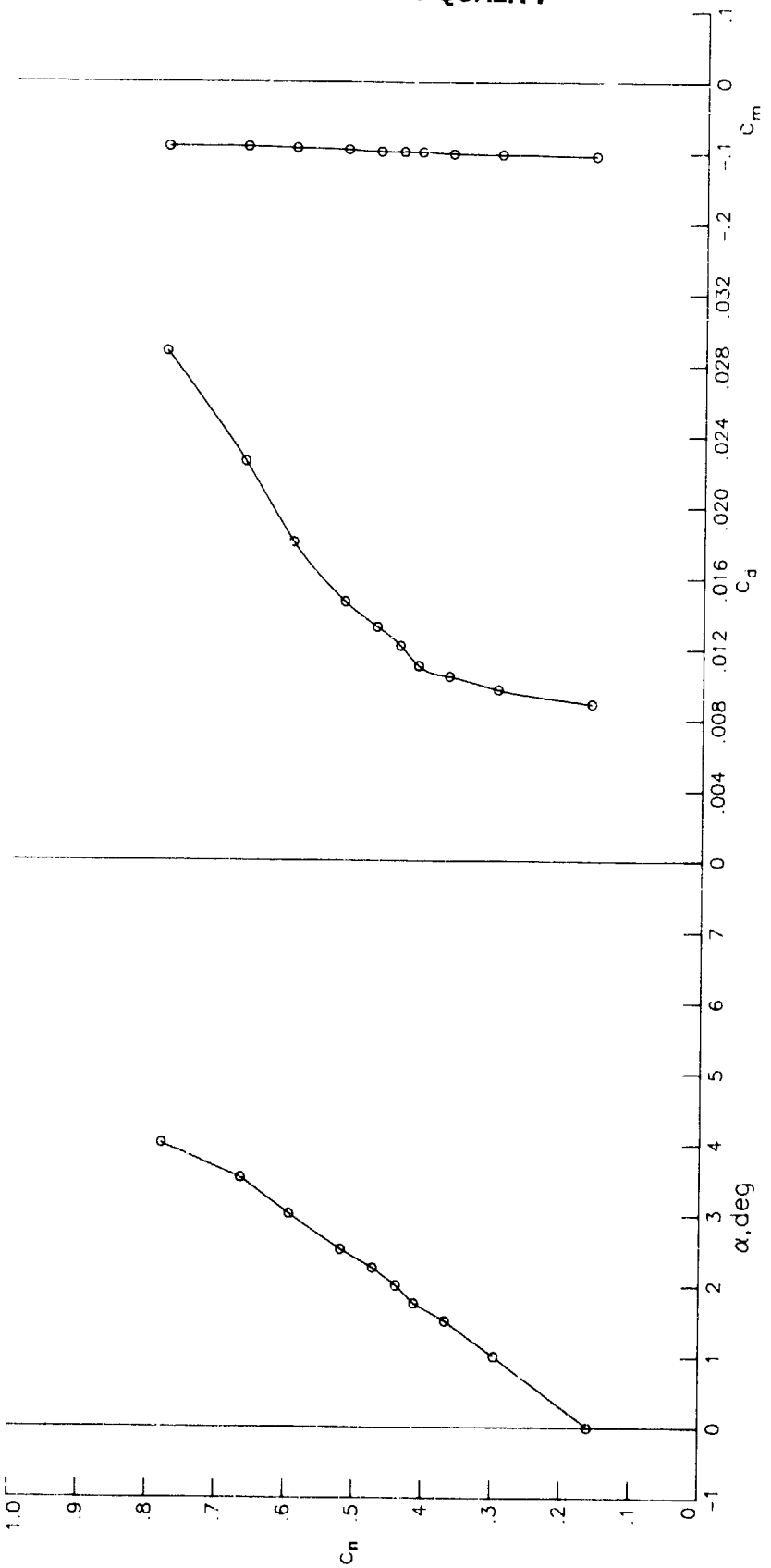

(f) R = 3.49 × 10^6; M = 0.7358.

Figure 5.- Continued.

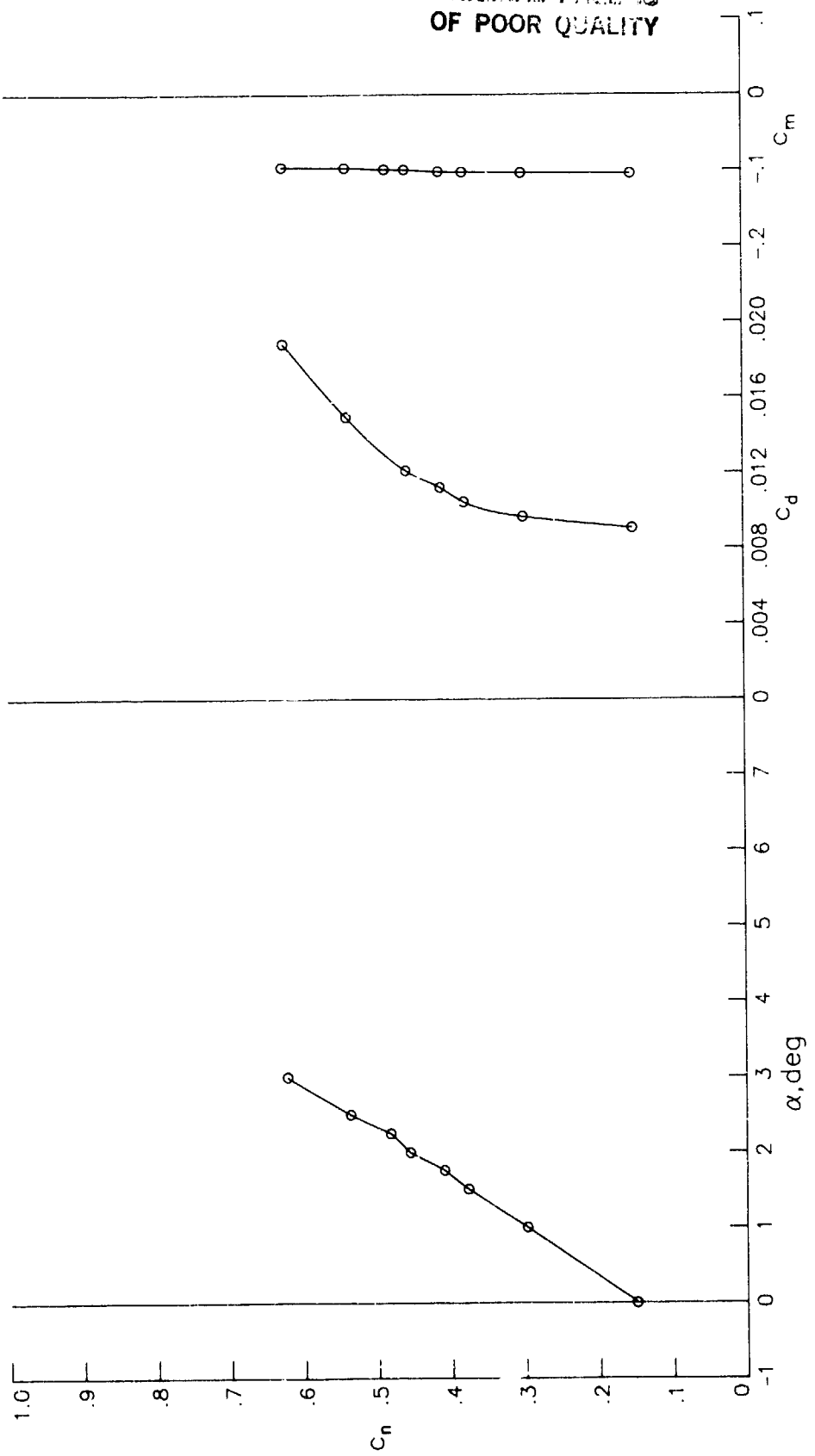

(g) R = 3.55 x 10^6; M = 0.7553.

Figure 5.- Continued.

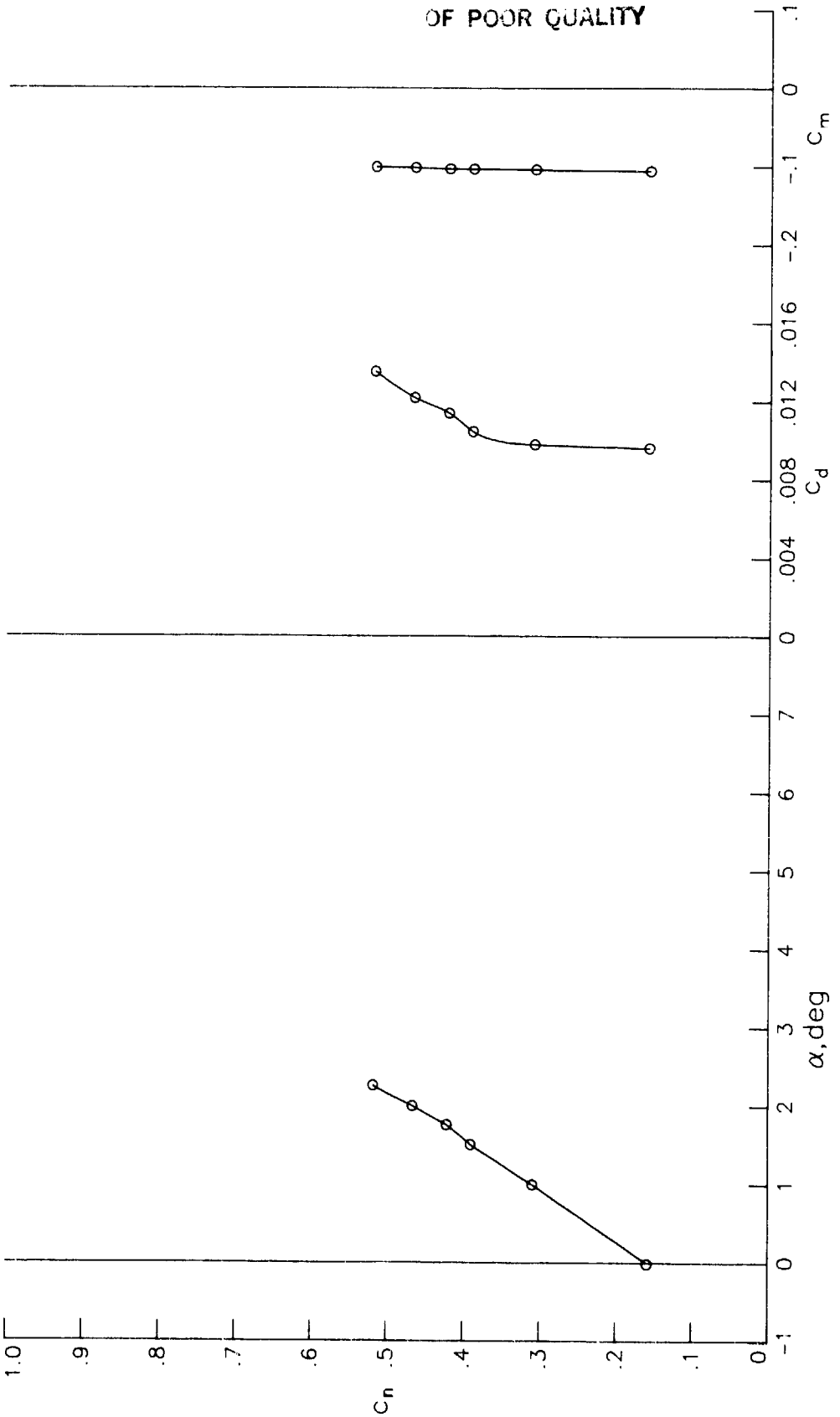

(h) R = 3.60 × 10^6; M = 0.7763.

Figure 5.- Concluded.

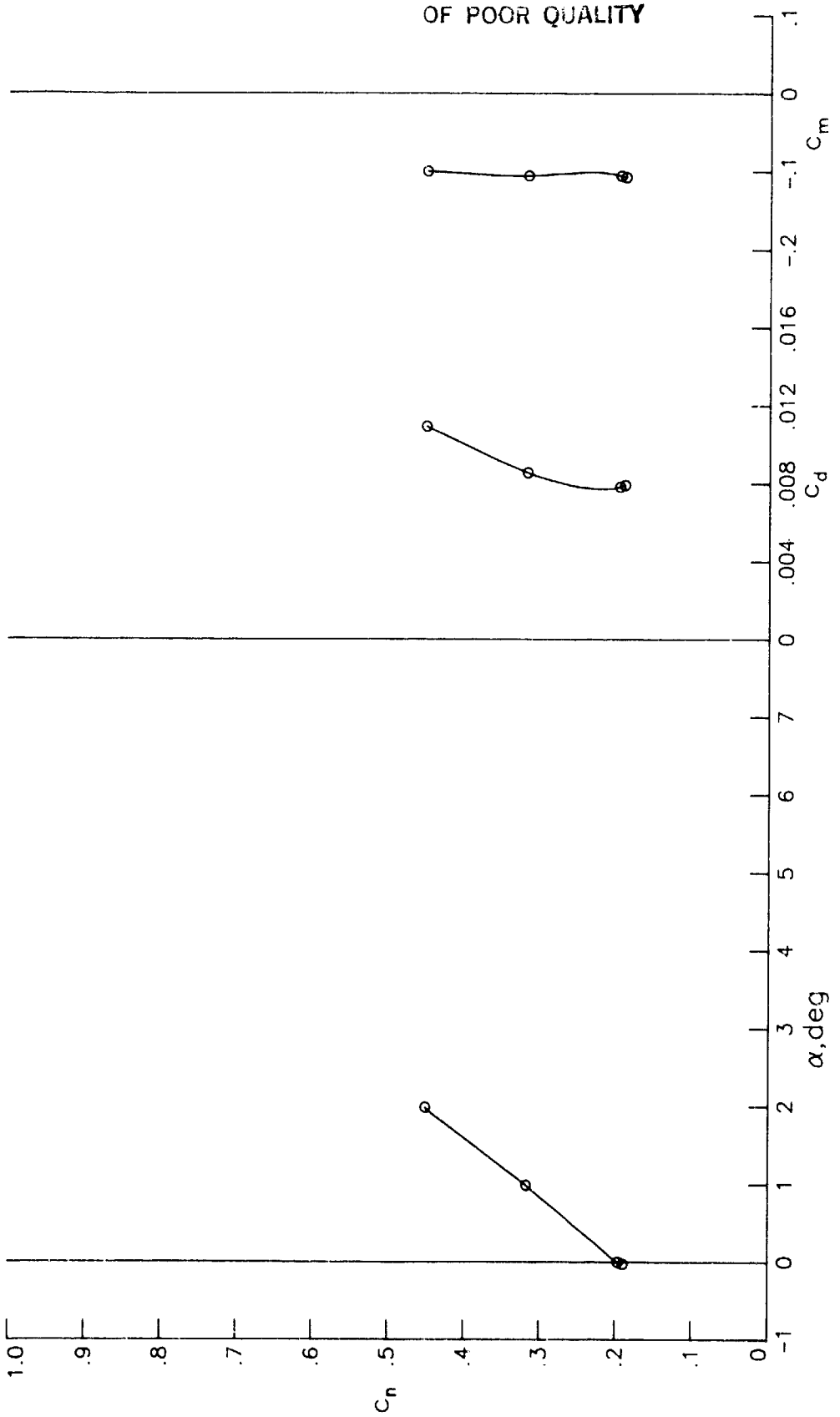

(a) $R = 3.60 \times 10^6$; $M = 0.6977$; $p_t = 1.69$ atm; $T_t = 280$ K.

Figure 6.- Section characteristics for two different values of Reynolds number, Mach number, total pressure, and total temperature with free transition.

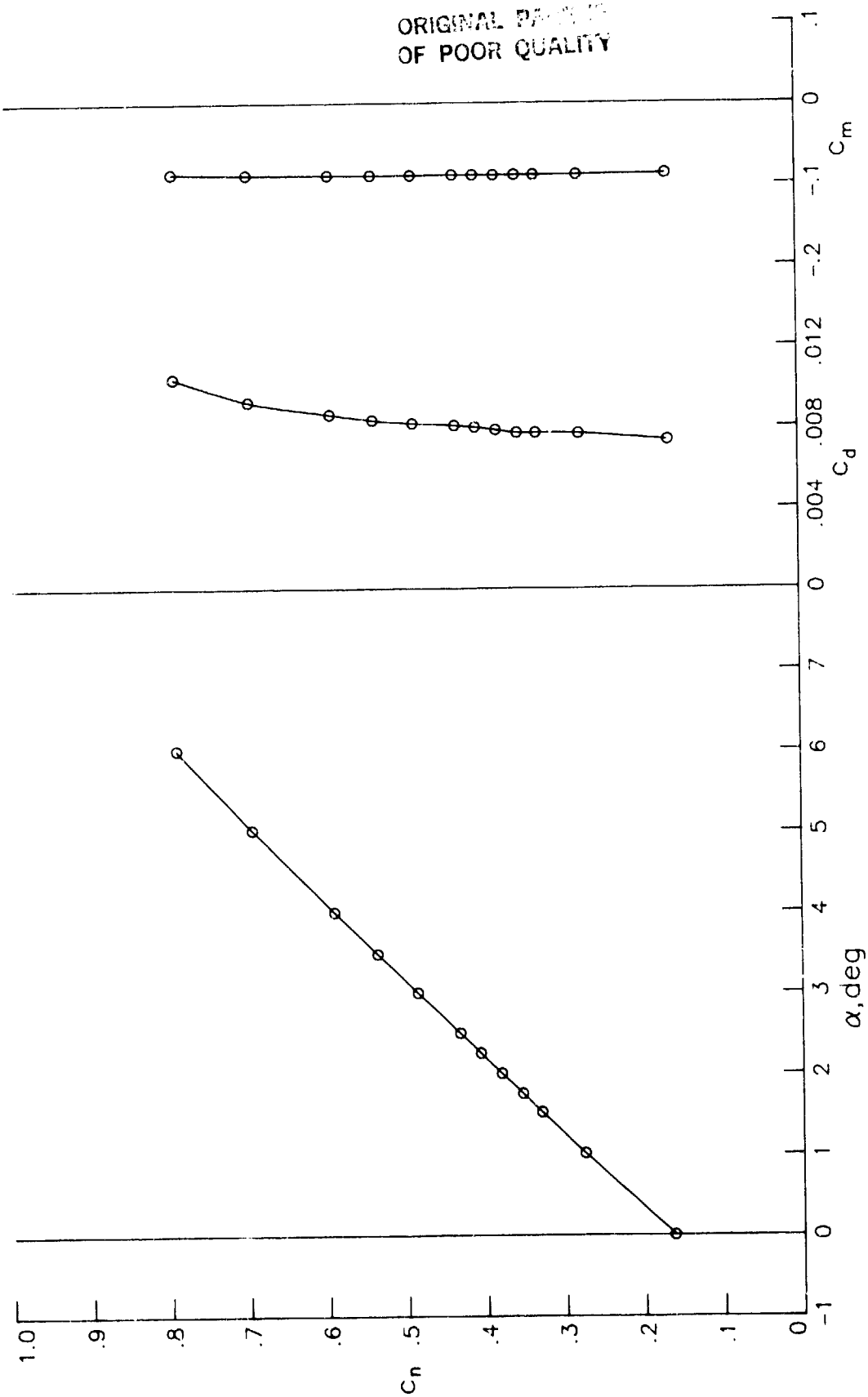

(b) R = 6.27 x 10^6; M = 0.3989; P_t = 3.47; T_t = 230 K.

Figure 6.- Concluded.

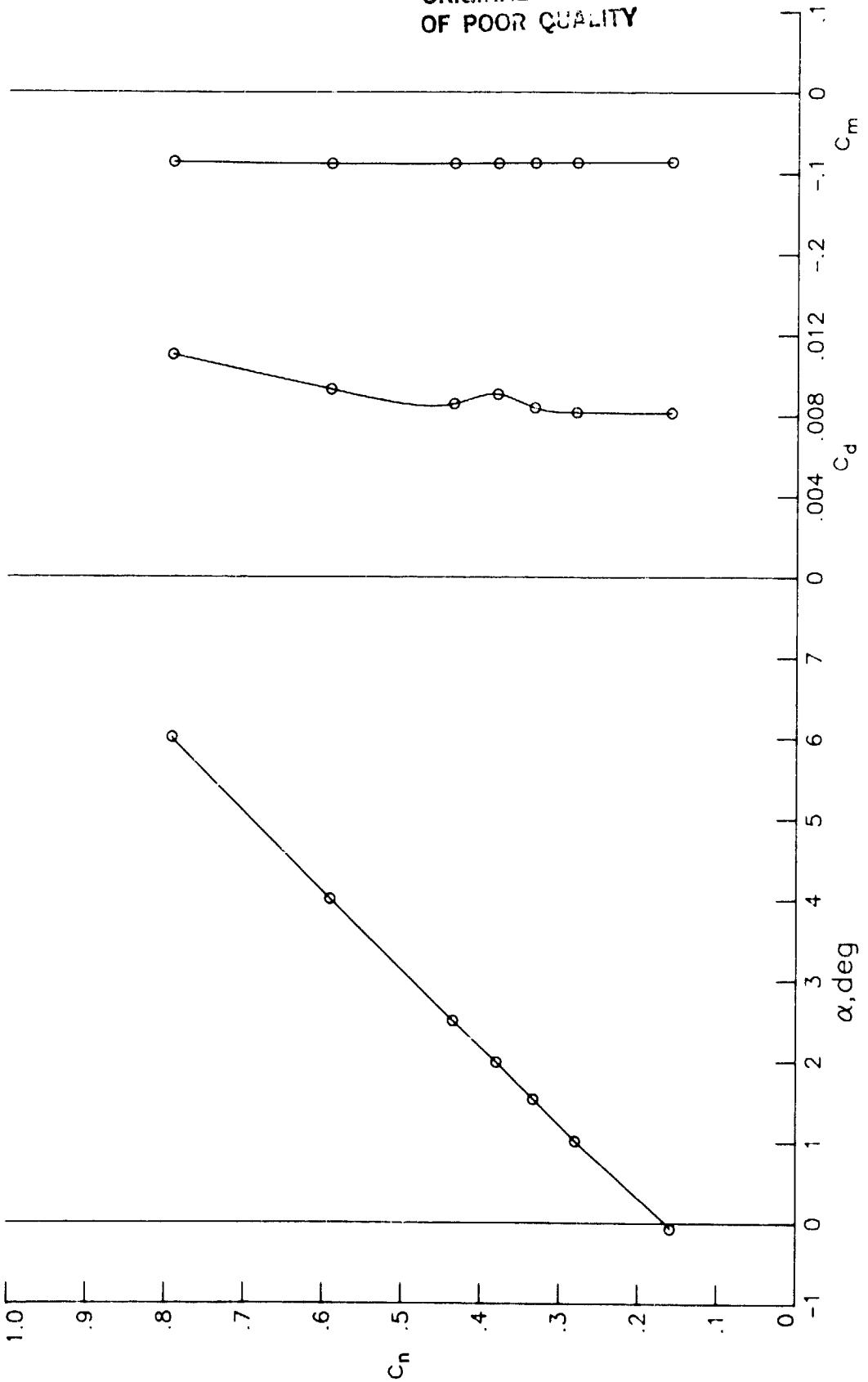

(a) R = 7.02 × 10^6; M = 0.3980.

Figure 7.- Section characteristics at Reynolds numbers of 7 × 10^6.

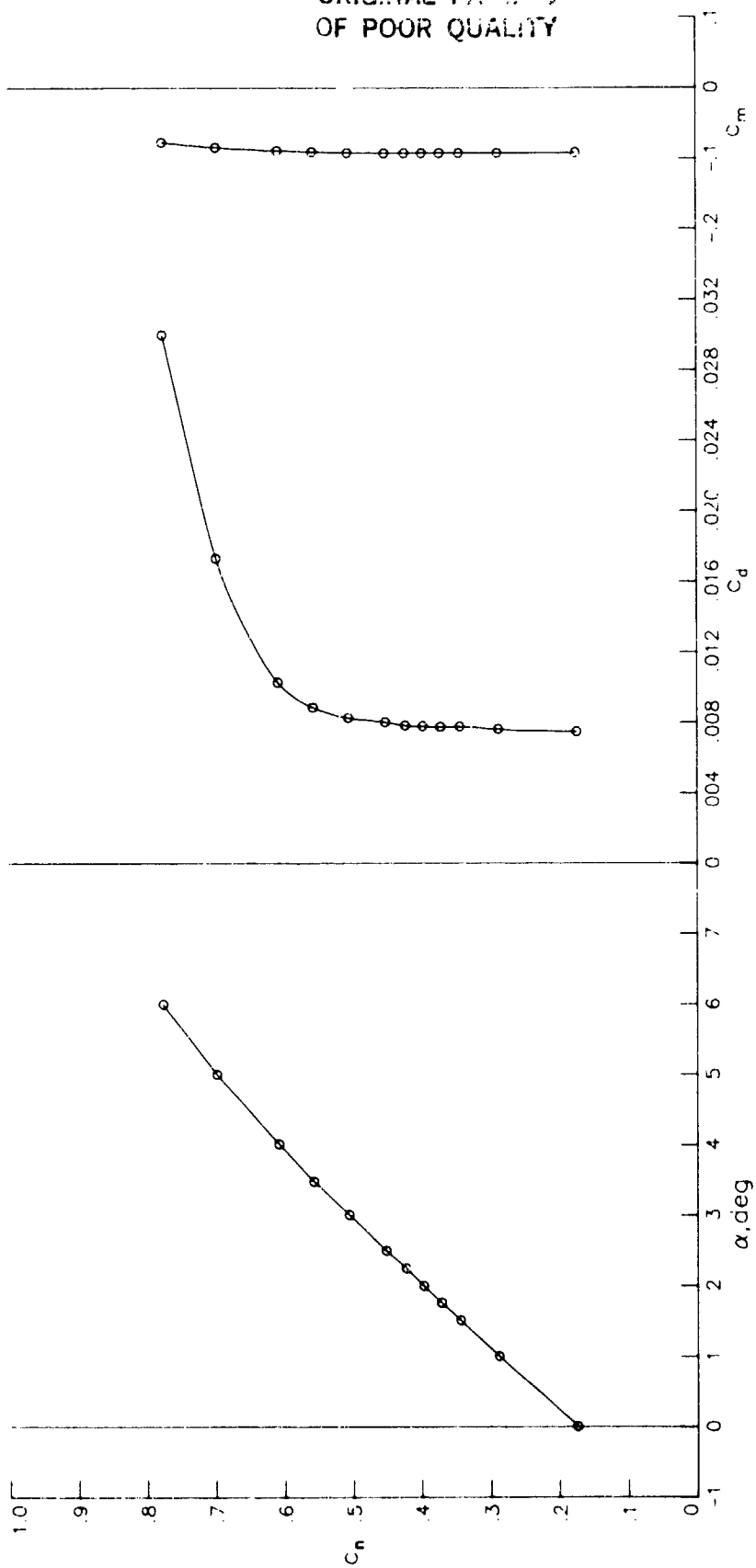

(b) R = 7.07 x 10^6; M = 0.4986.

Figure 7.- Continued.

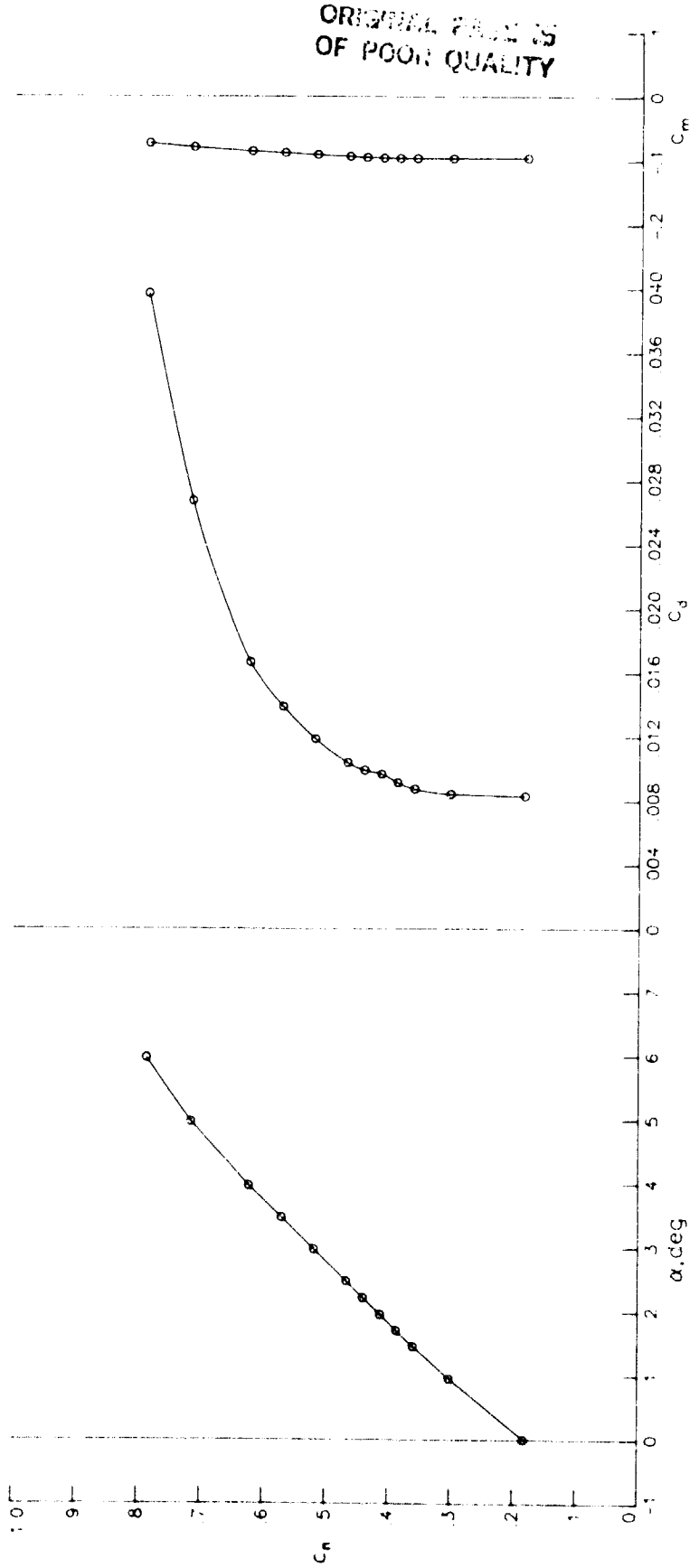

(c) R = 6.99 × 10^6; M = 0.5960.

Figure 7.- Continued.

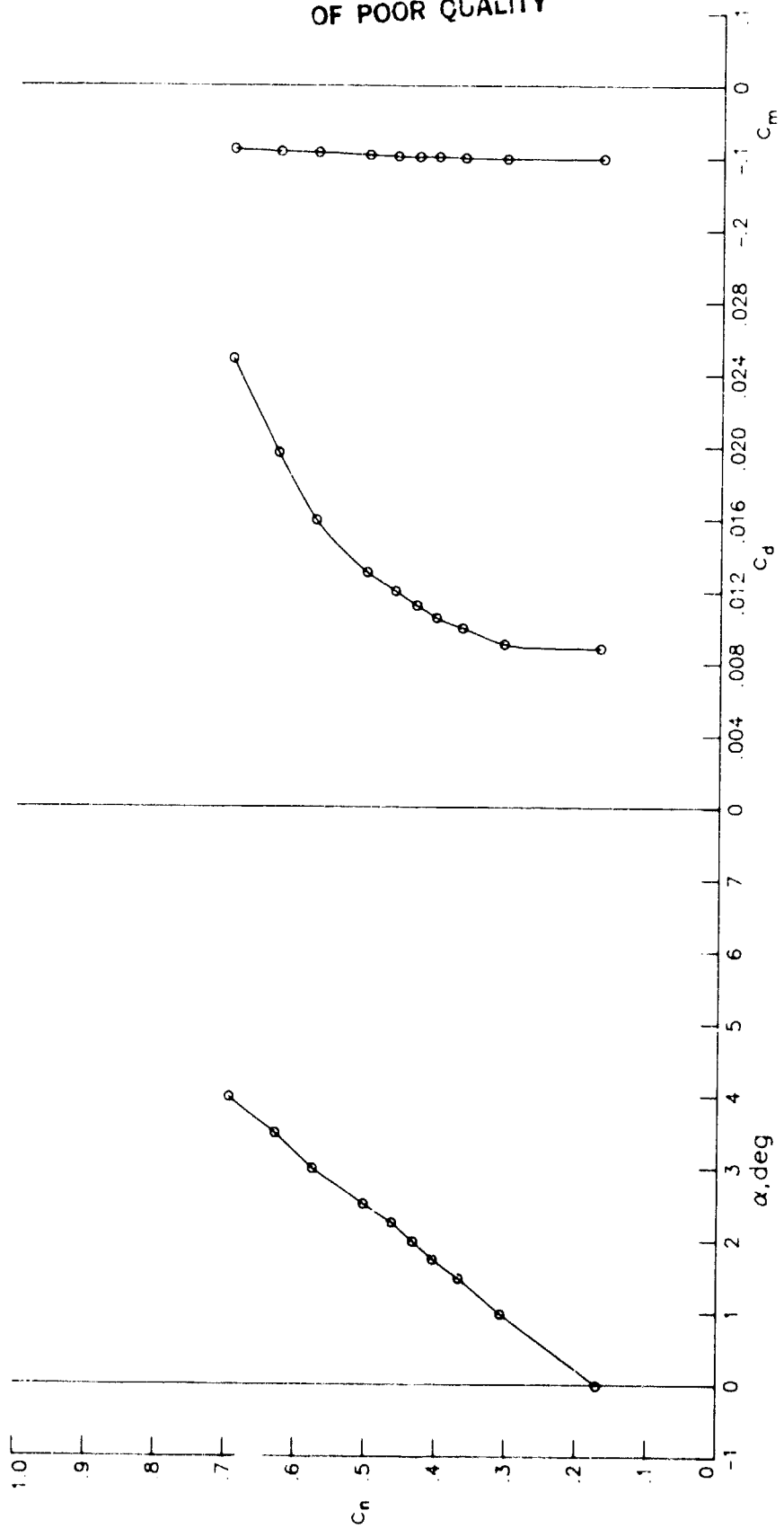

(d) R = 7.04 x 10^6; M = 0.6944.

Figure 7.- Continued.

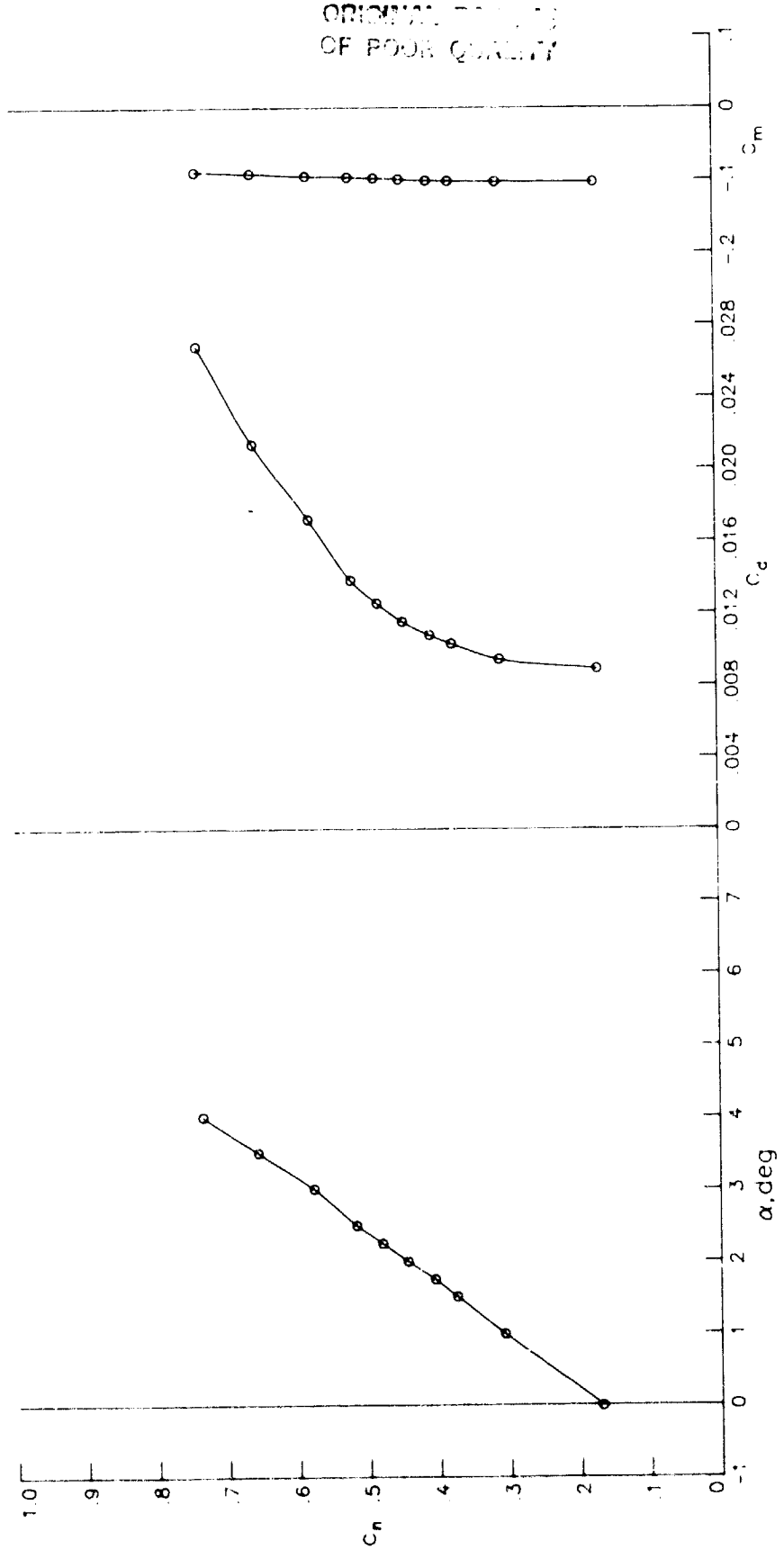

(e) R = 7.03 x 10^6; M = 0.7143.

Figure 7.- Continued.

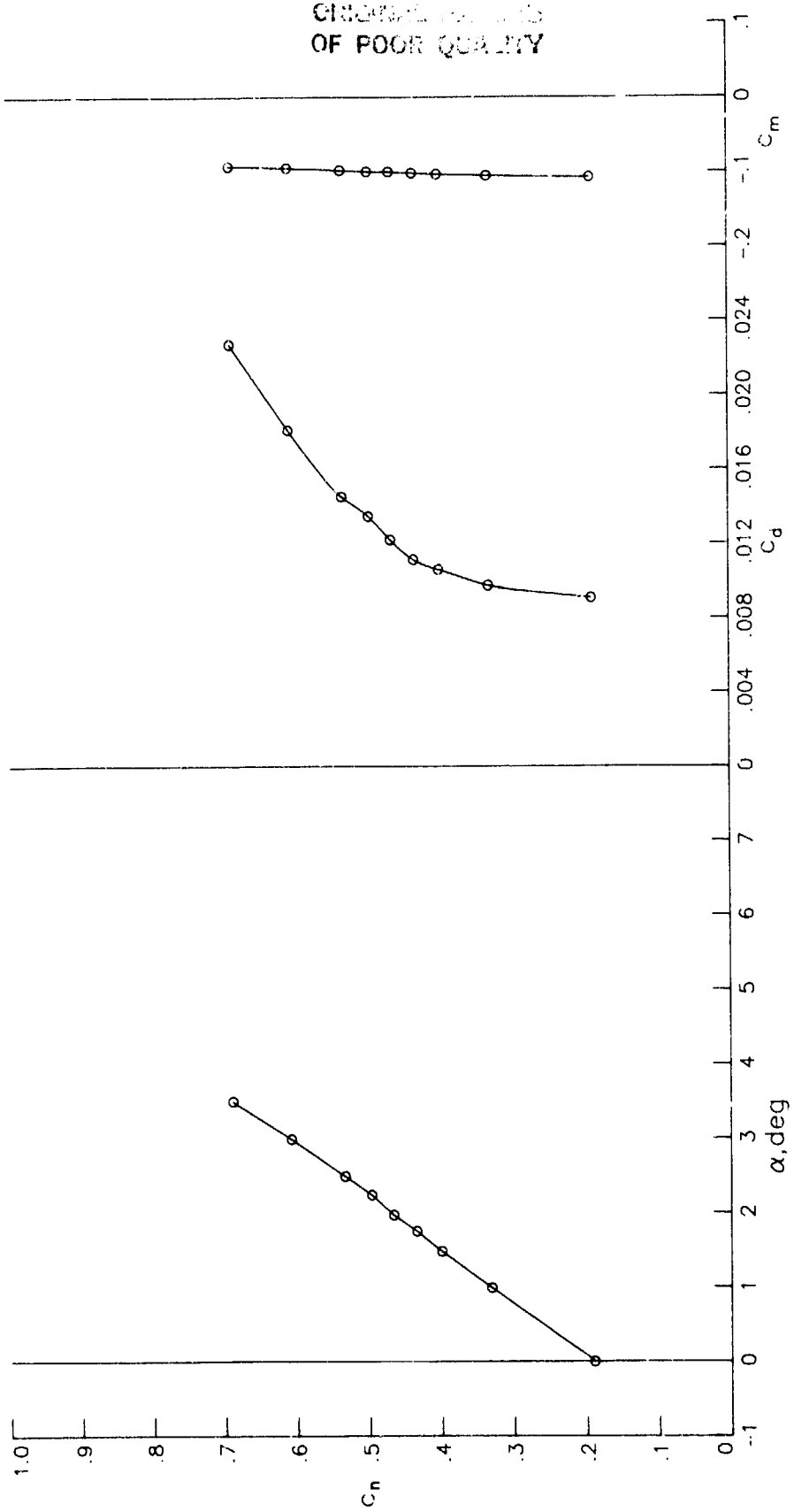

(f) $R = 7.02 \times 10^6$; $M = 0.7338$.

Figure 7.- Continued.

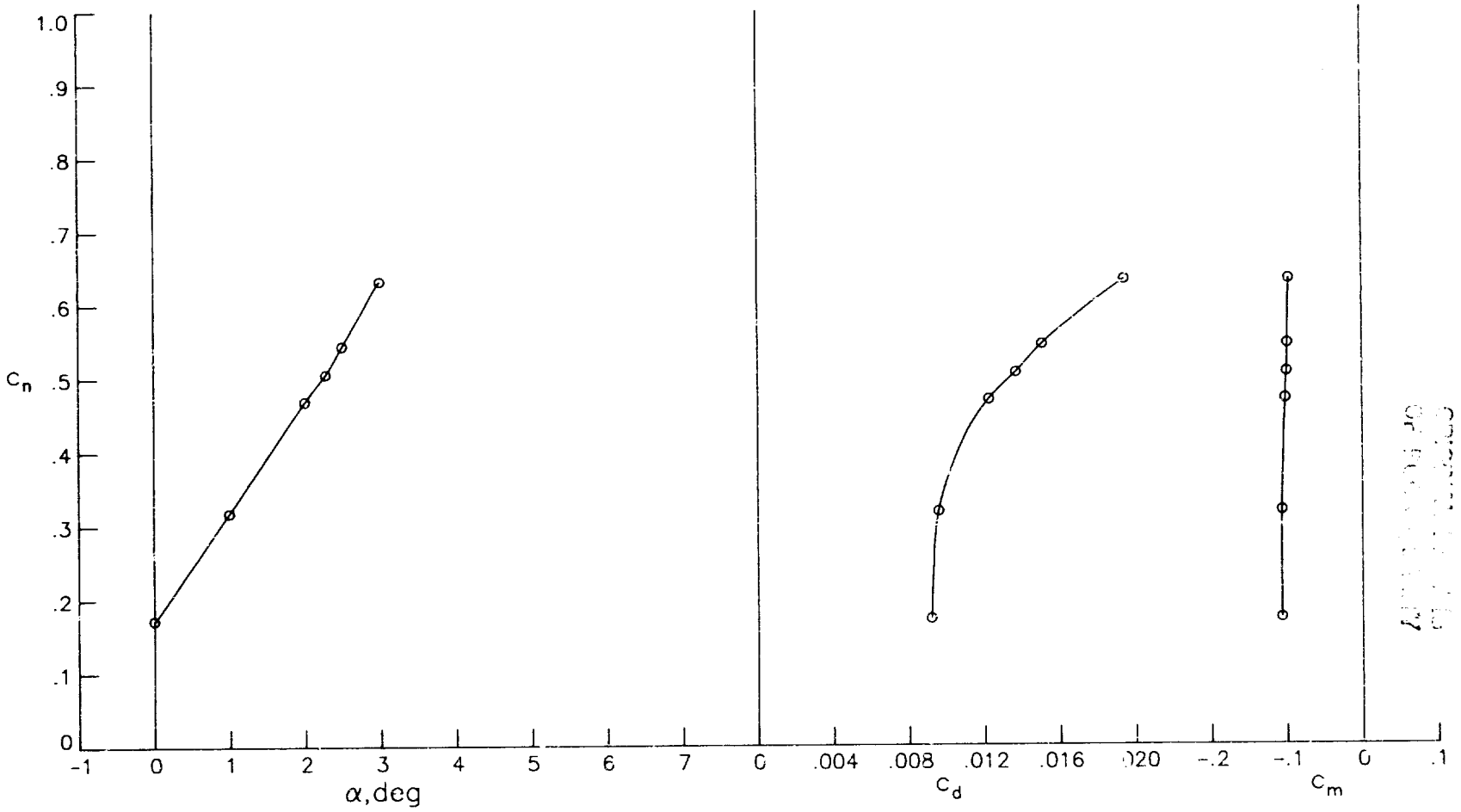

(g) $R = 7.02 \times 10^6$; $M = 0.7527$.

Figure 7.- Continued.

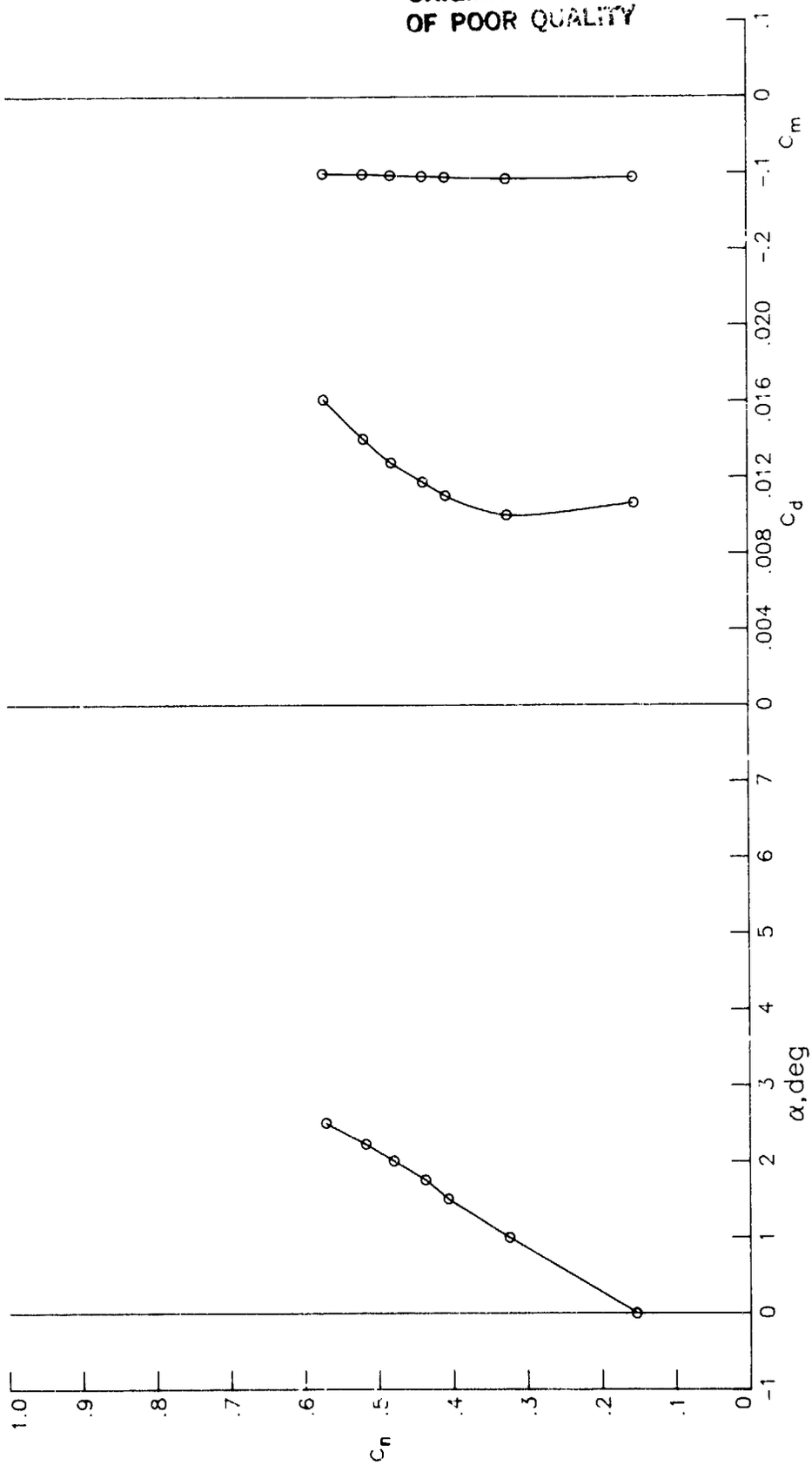

(h) R = 7.04 x 10^6; M = 0.7729.

Figure 7.- Continued.

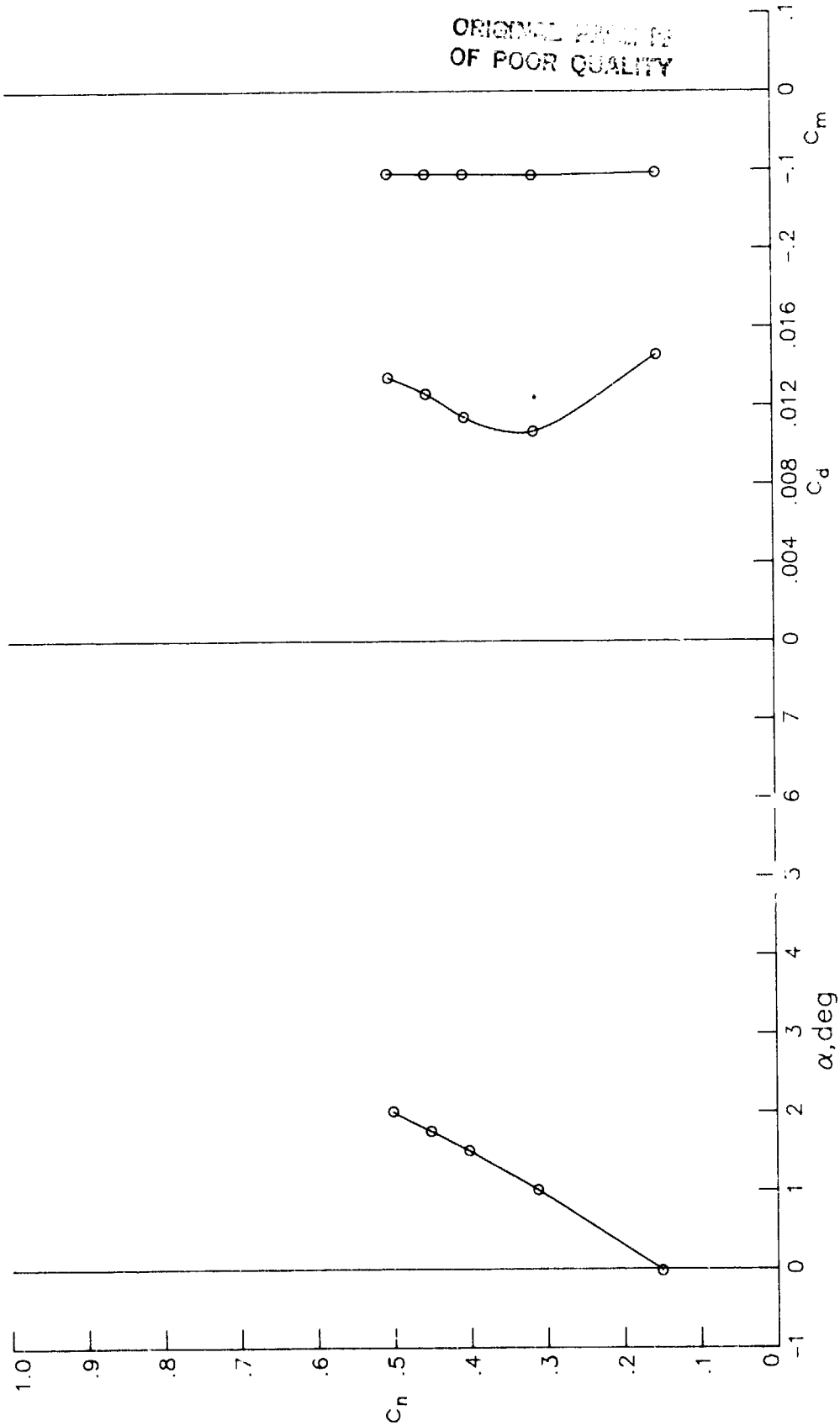

(i) R = 7.04 × 10^6; M = 0.7925.

Figure 7.- Continued.

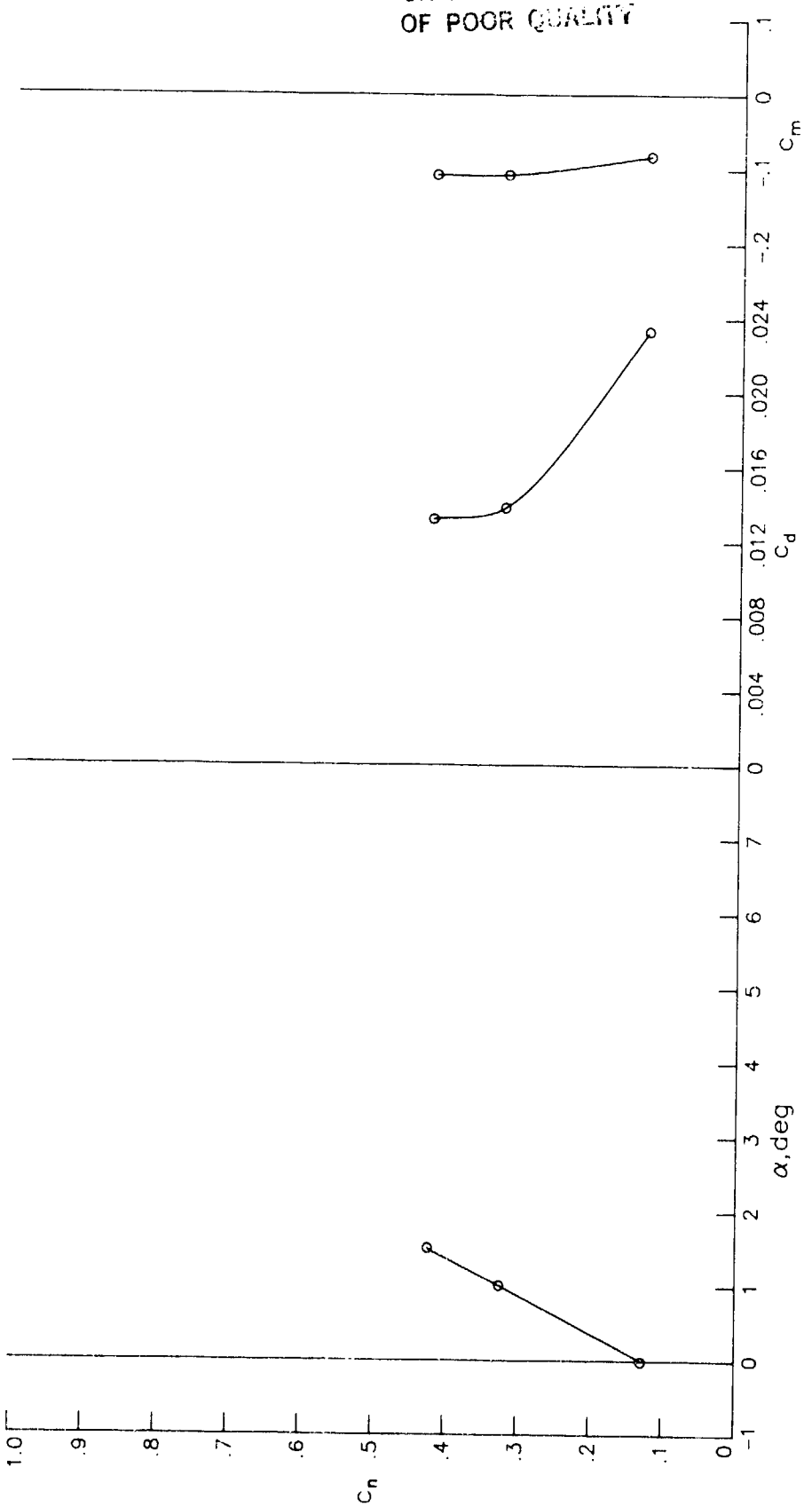

(j) R = 7.06 × 10^6; M = 0.8096.

Figure 7.- Concluded.

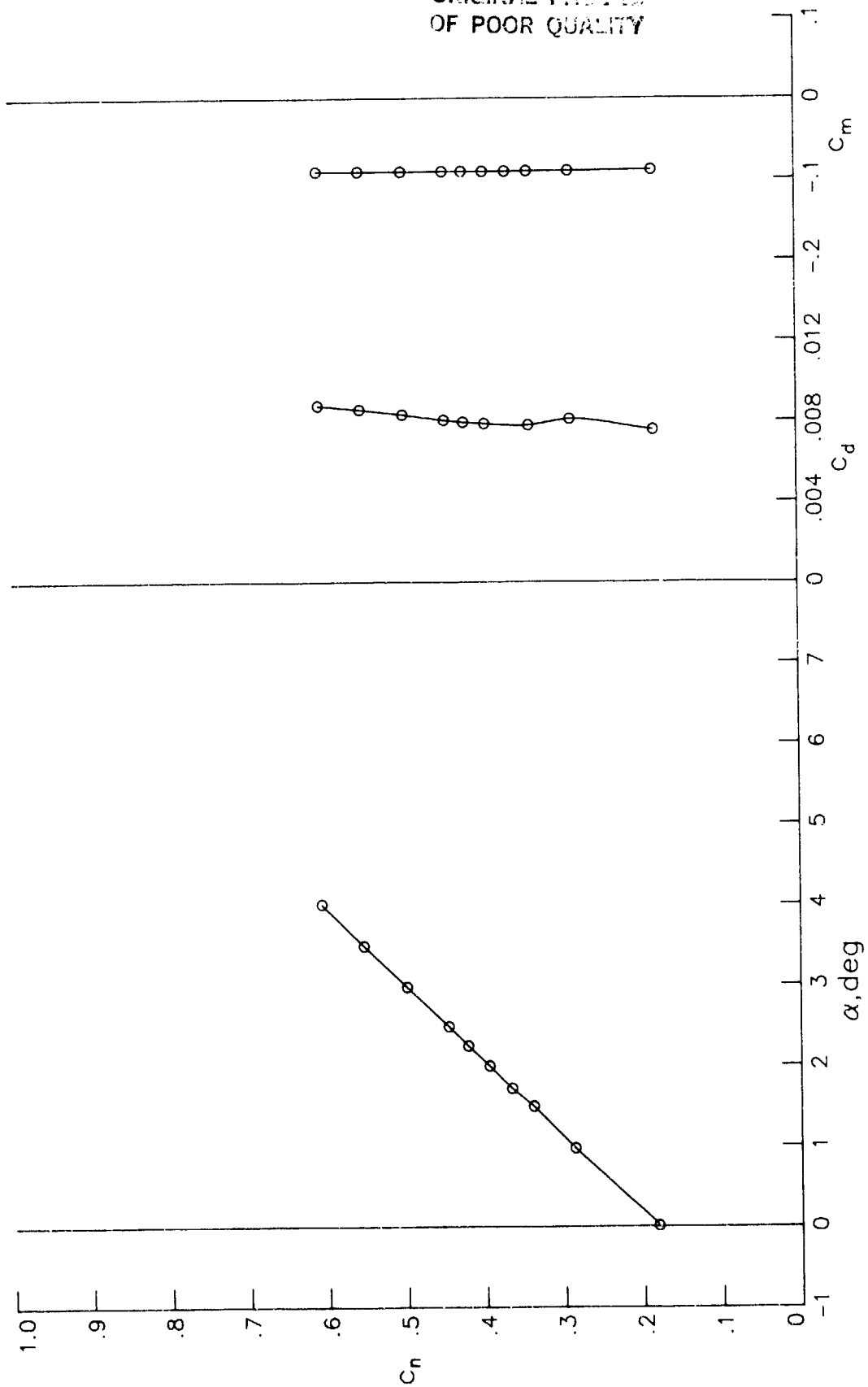

(a) R = 15.02 × 10^6; M = 0.3977.

Figure 8.- Section characteristics at Reynolds numbers of 15 × 10^6.

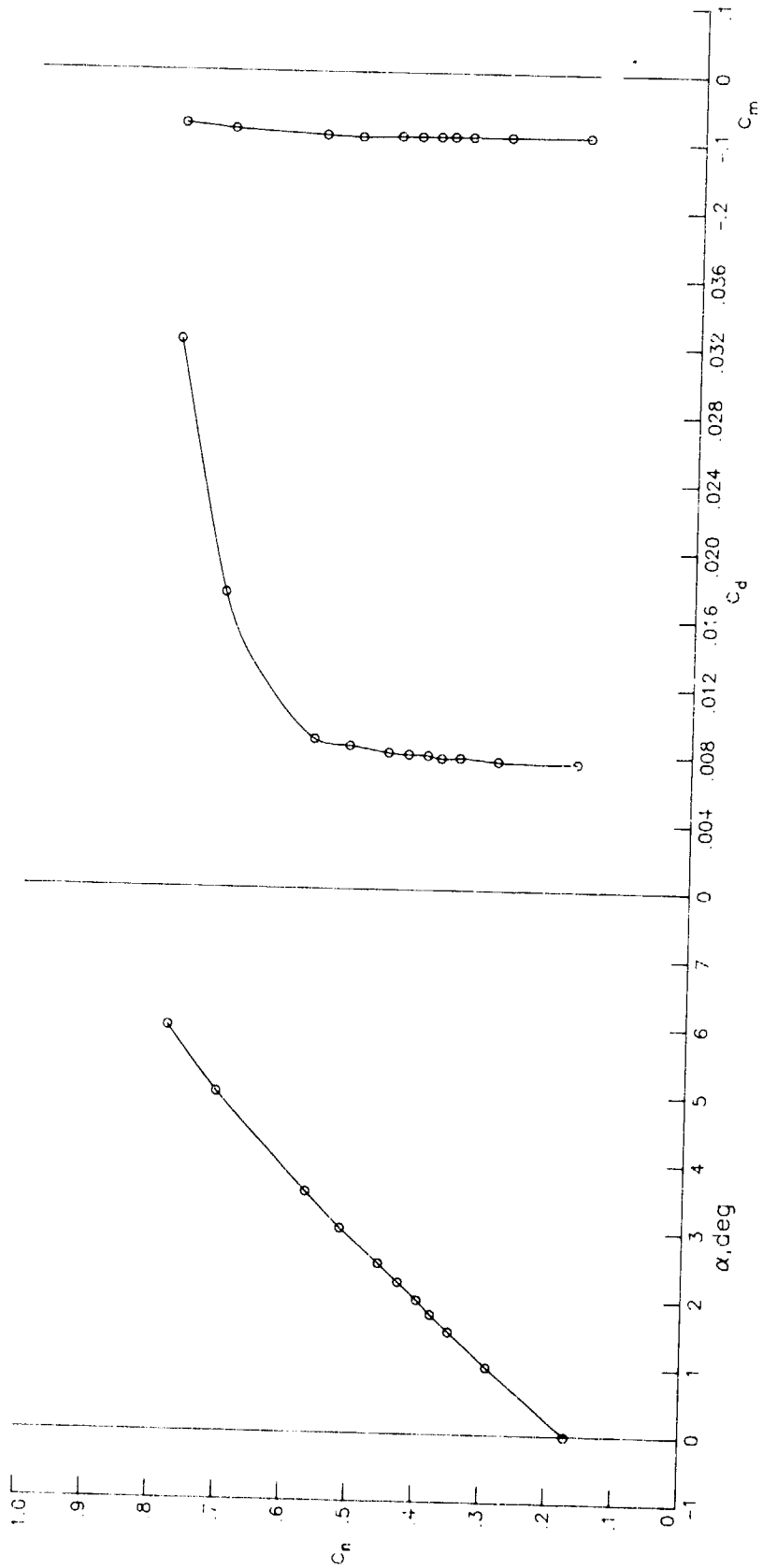

(b) R = 14.94 x 10^6; M = 0.4975.

Figure 8.- Continued.

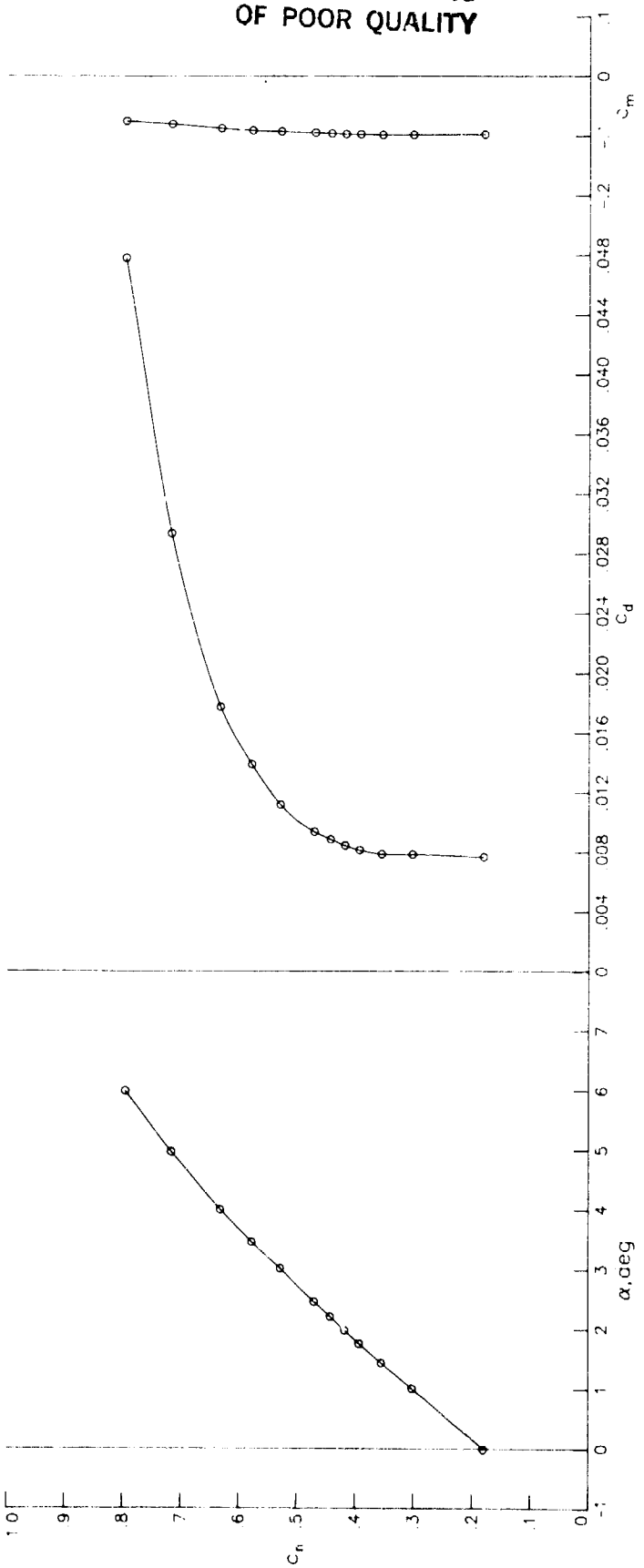

(c) R = 14.89 x 10^6; M = 0.5968.

Figure 8.- Continued.

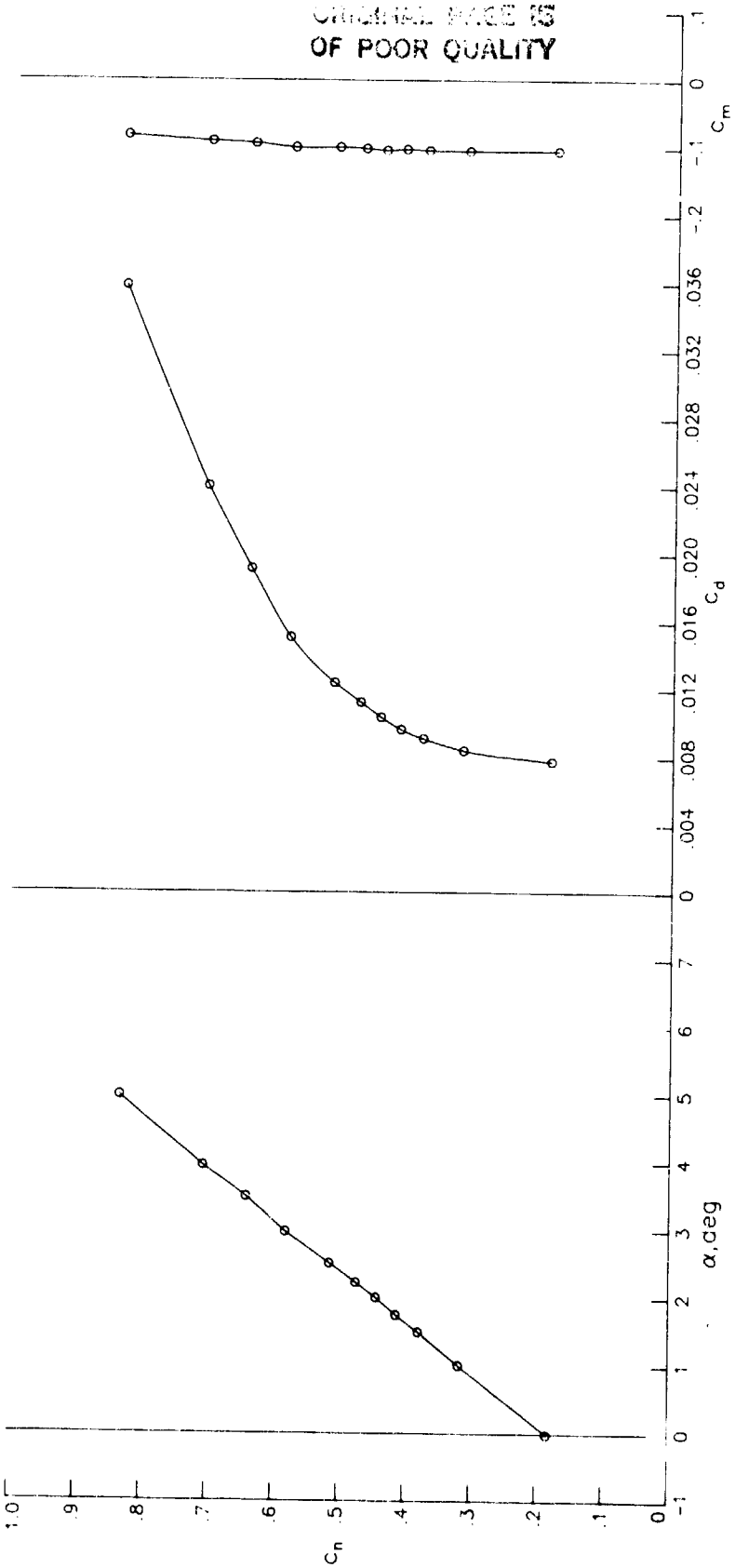

(d) R = 14.88 x 10^6; M = 0.6933.

Figure 8.- Continued.

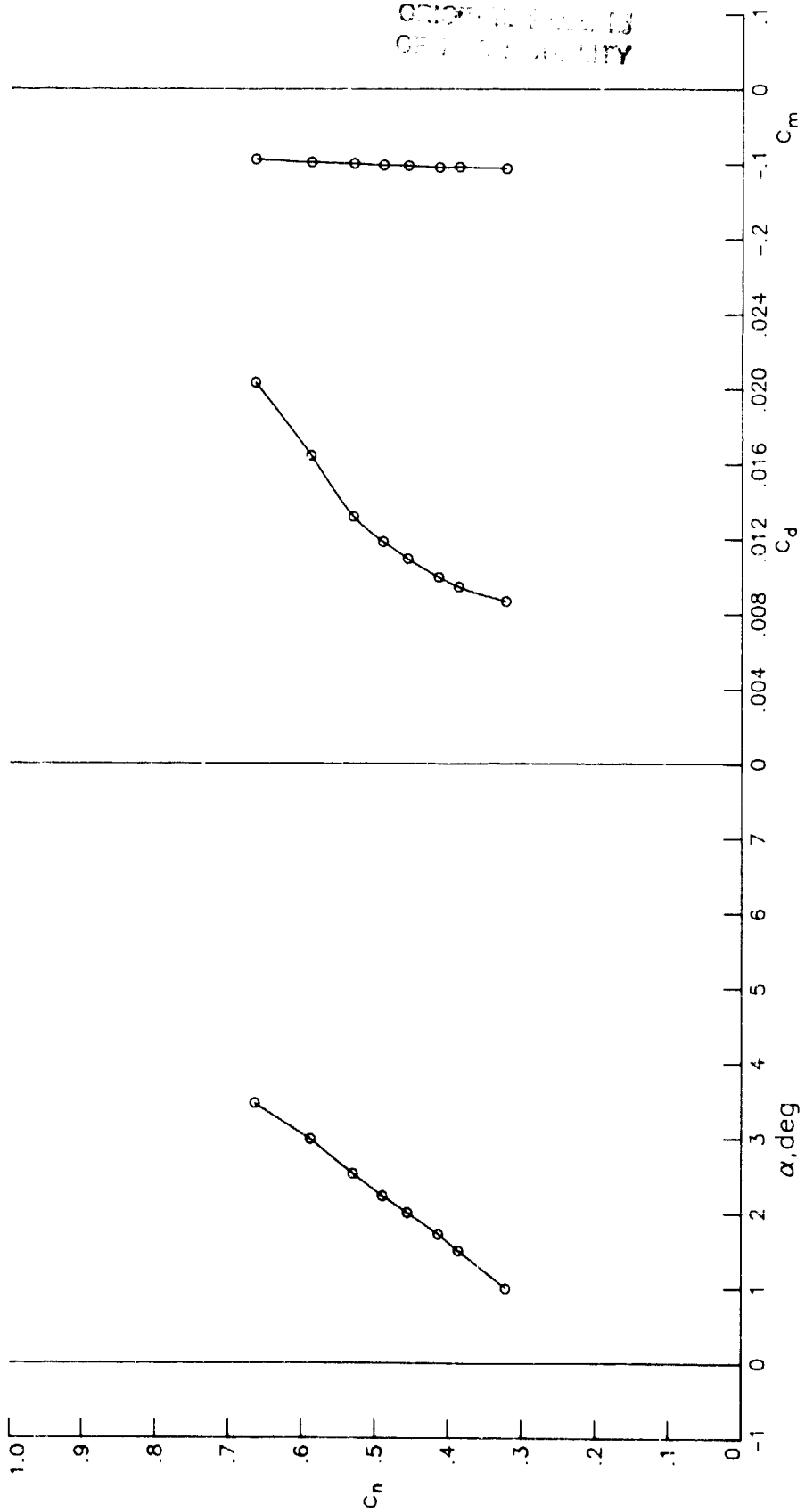

(e) R = 14.94 x 10^6; M = 0.7133.

Figure 8.- Continued.

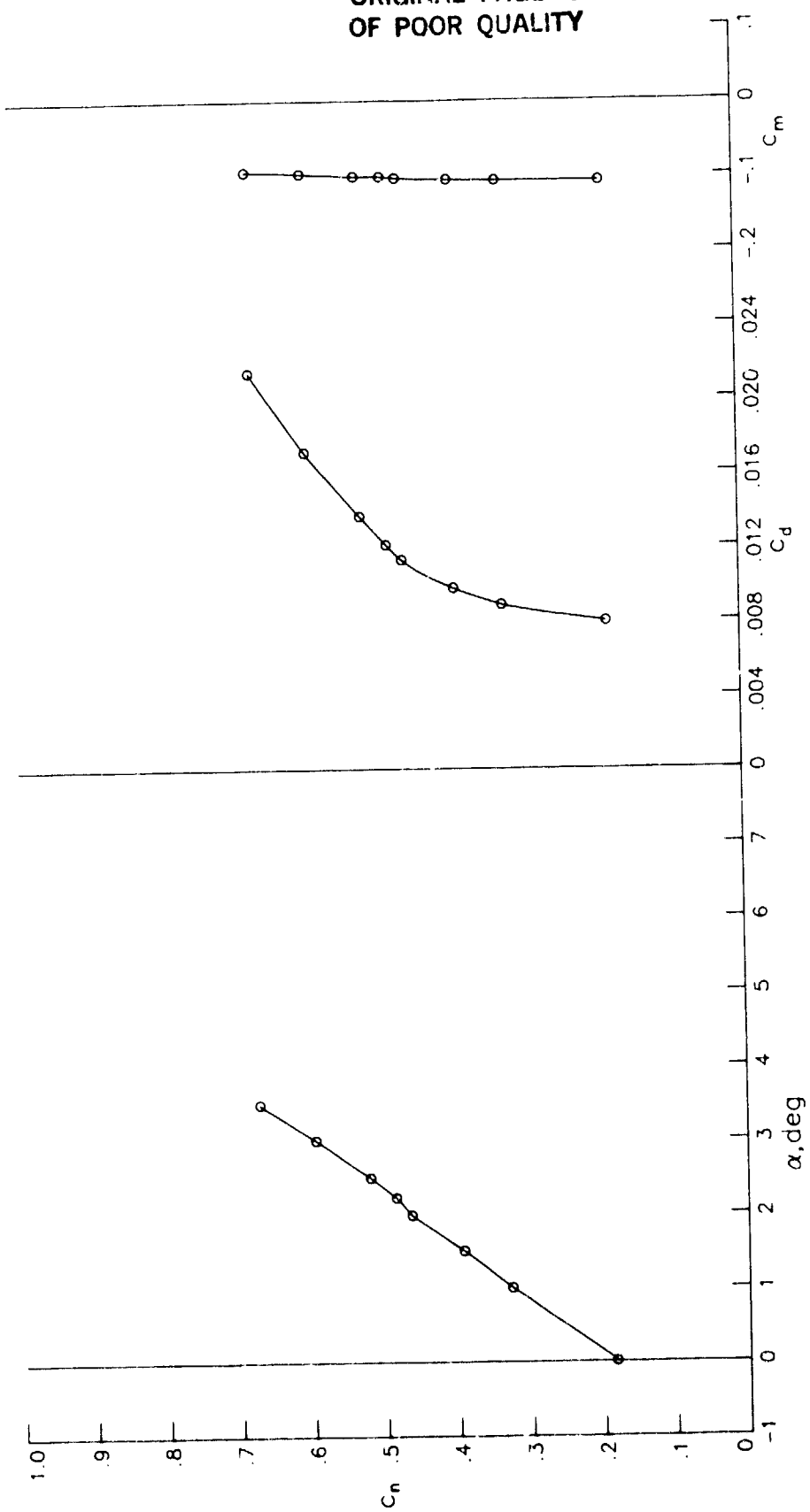

(f) R = 14.98 × 10^6; M = 0.7336.

Figure 8.- Continued.

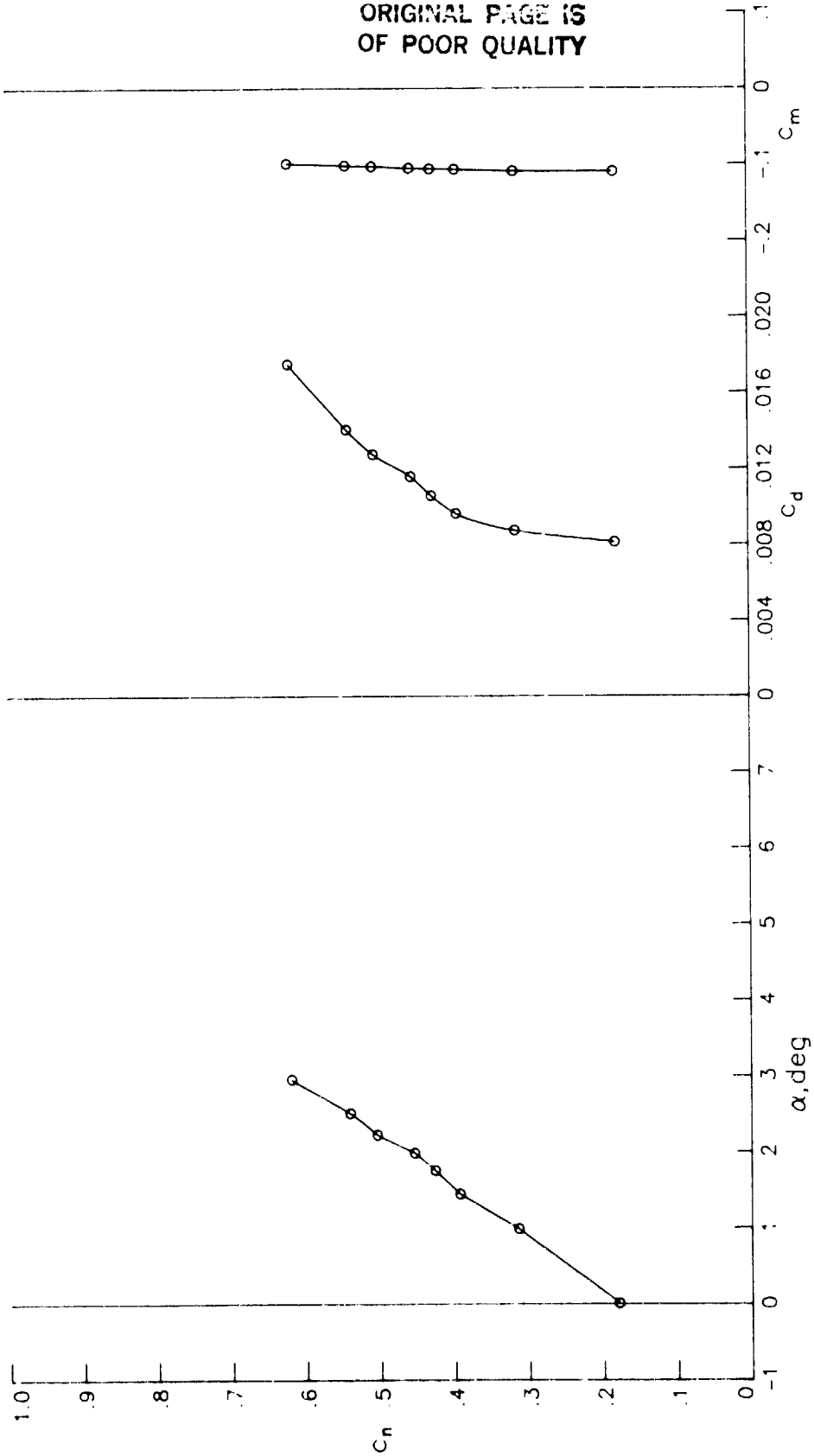

(g) R = 15.25 x 10^6; M = 0.7536.

Figure 8.- Continued.

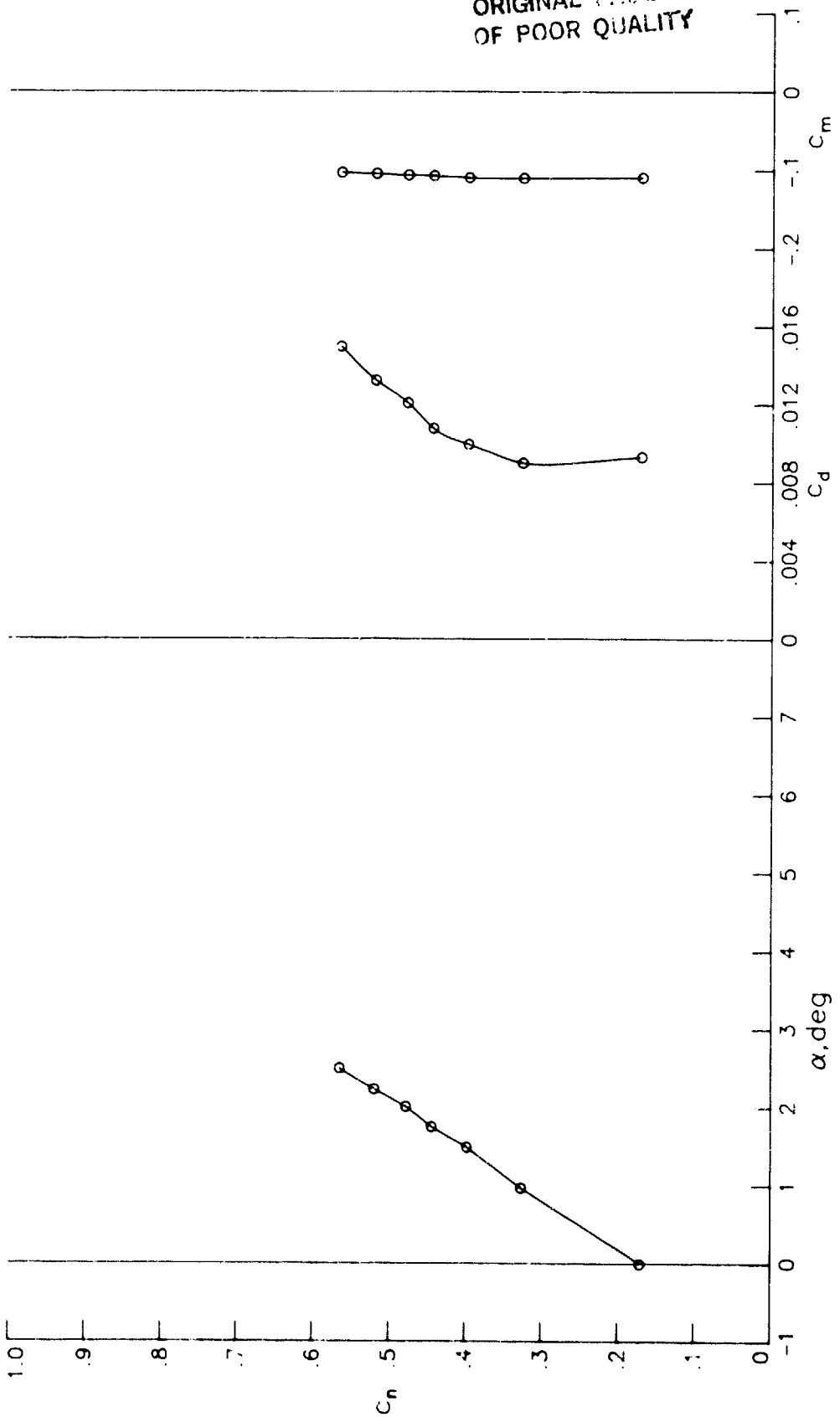

(h) R = 14.88 x 10^6; M = 0.7727.

Figure 8.- Continued.

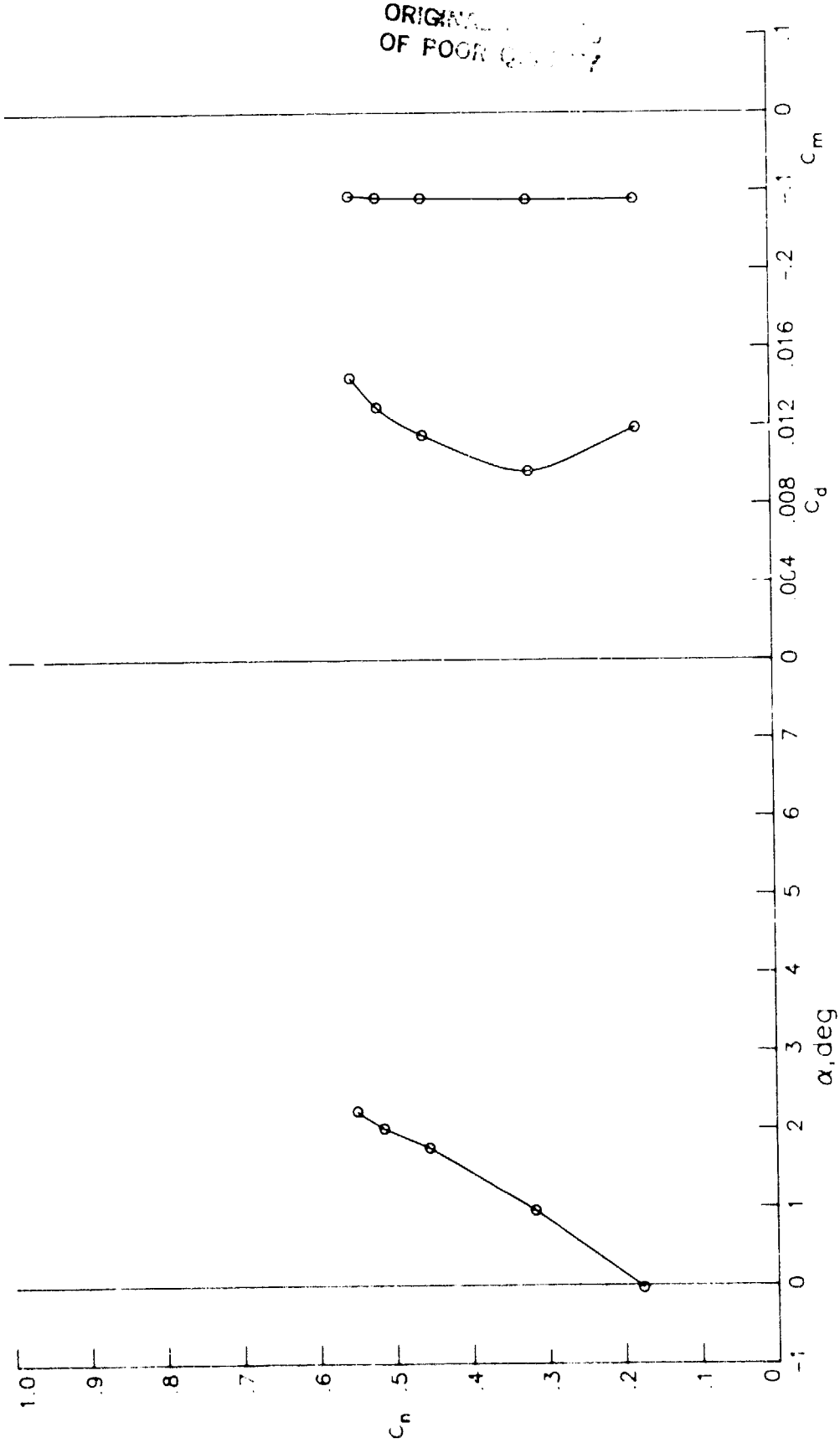

(i) R = 14.94 × 10^6; M = 0.7921.

Figure 8.- Continued.

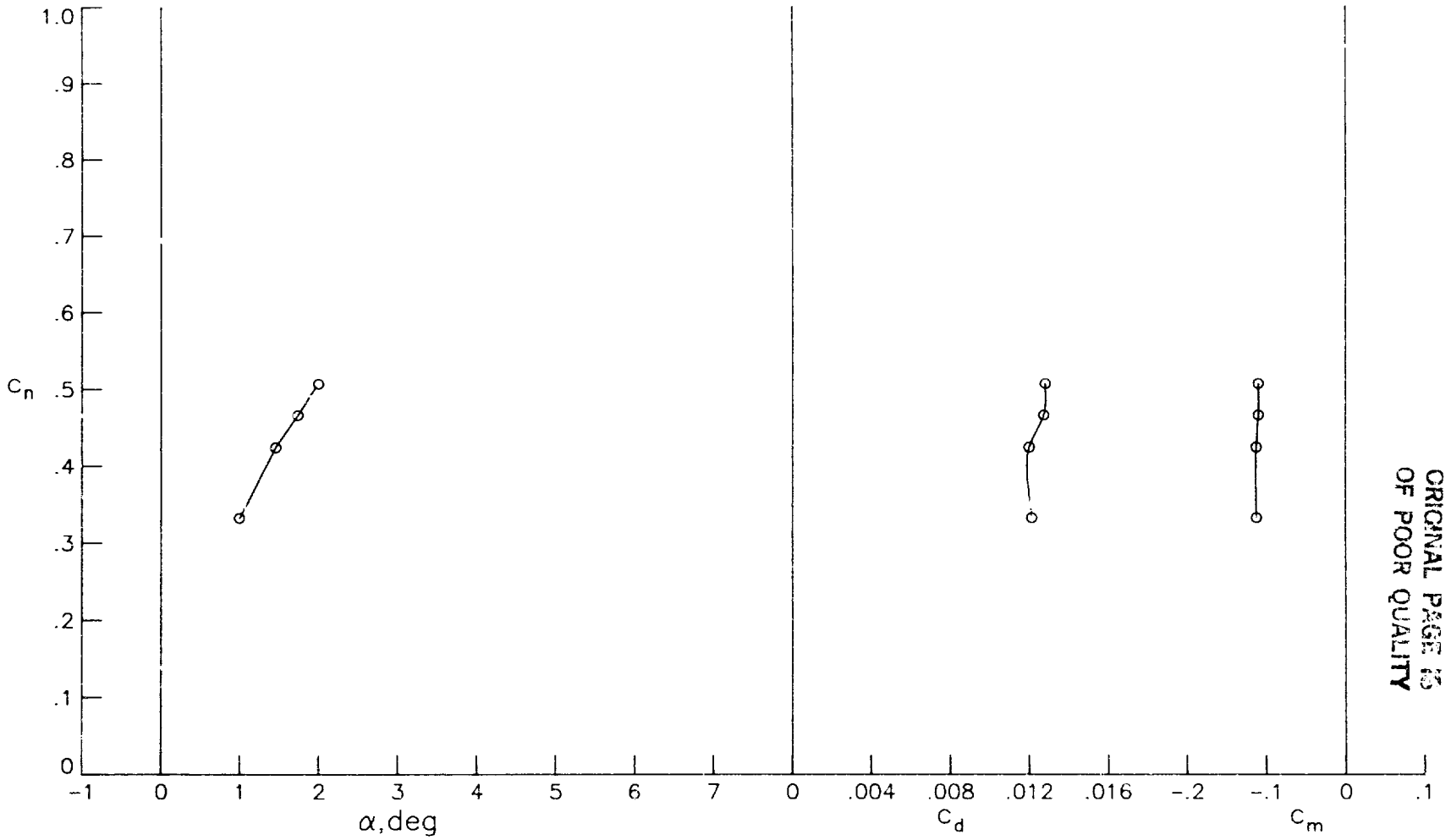

(j) R = 14.90 × 10^6; M = 0.8112.

Figure 8.- Concluded.

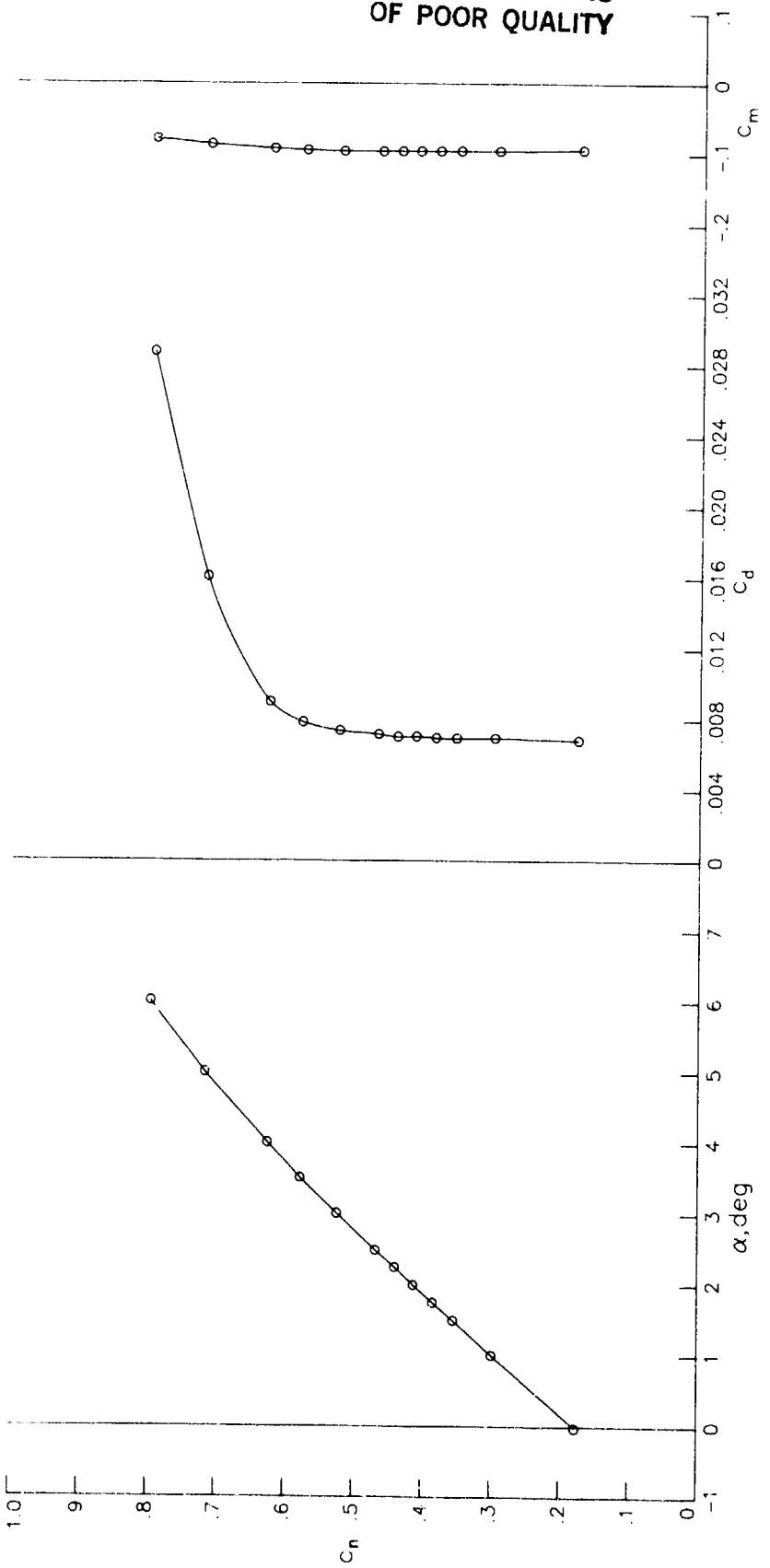

(a) R = 30.03 × 10^6; M = 0.4993.

Figure 9.- Section characteristics at Reynolds numbers of 30 × 10^6.

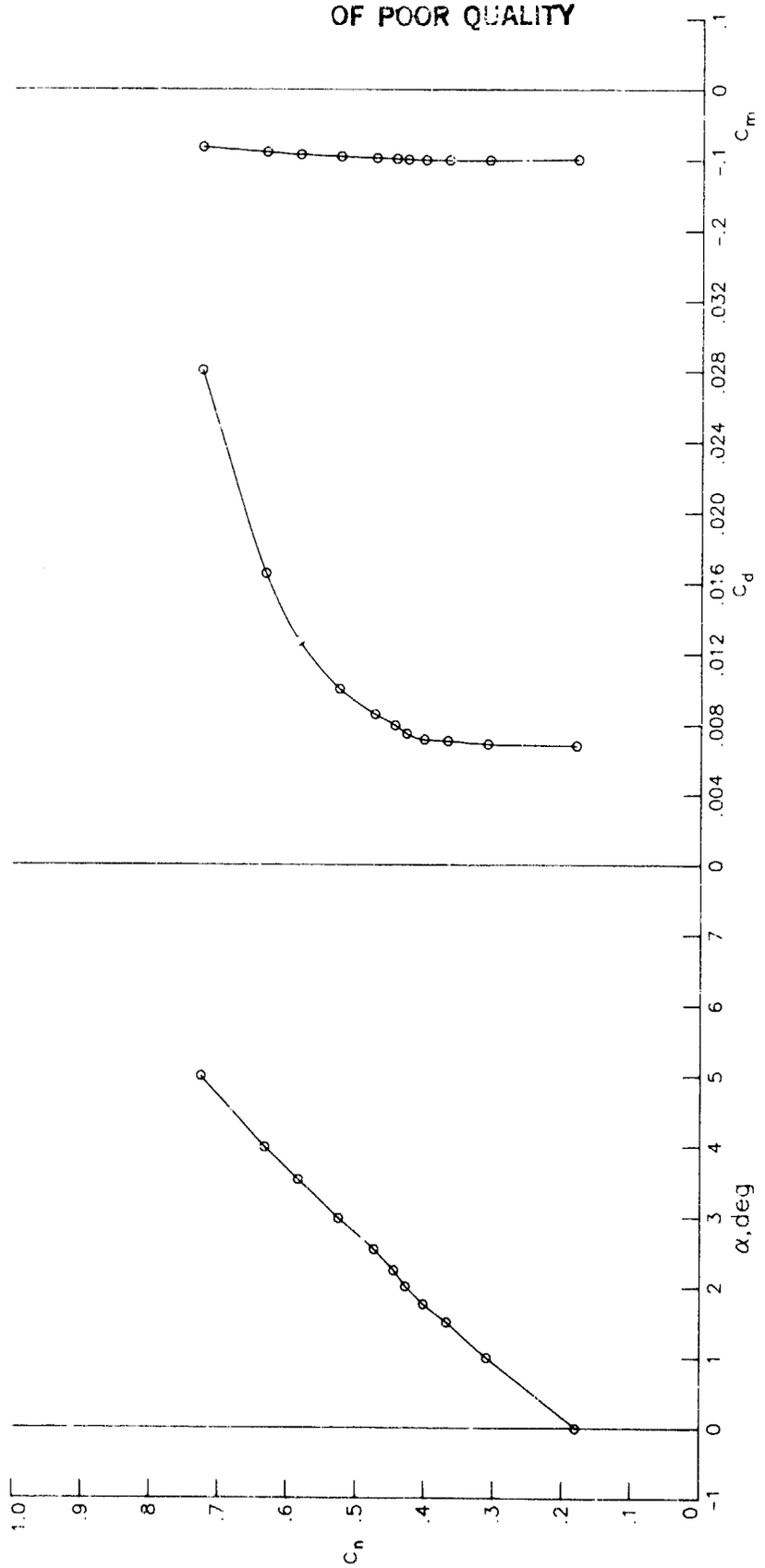

(b) R = 30.13 x 10^6; M = 0.5987.

Figure 9.- Continued.

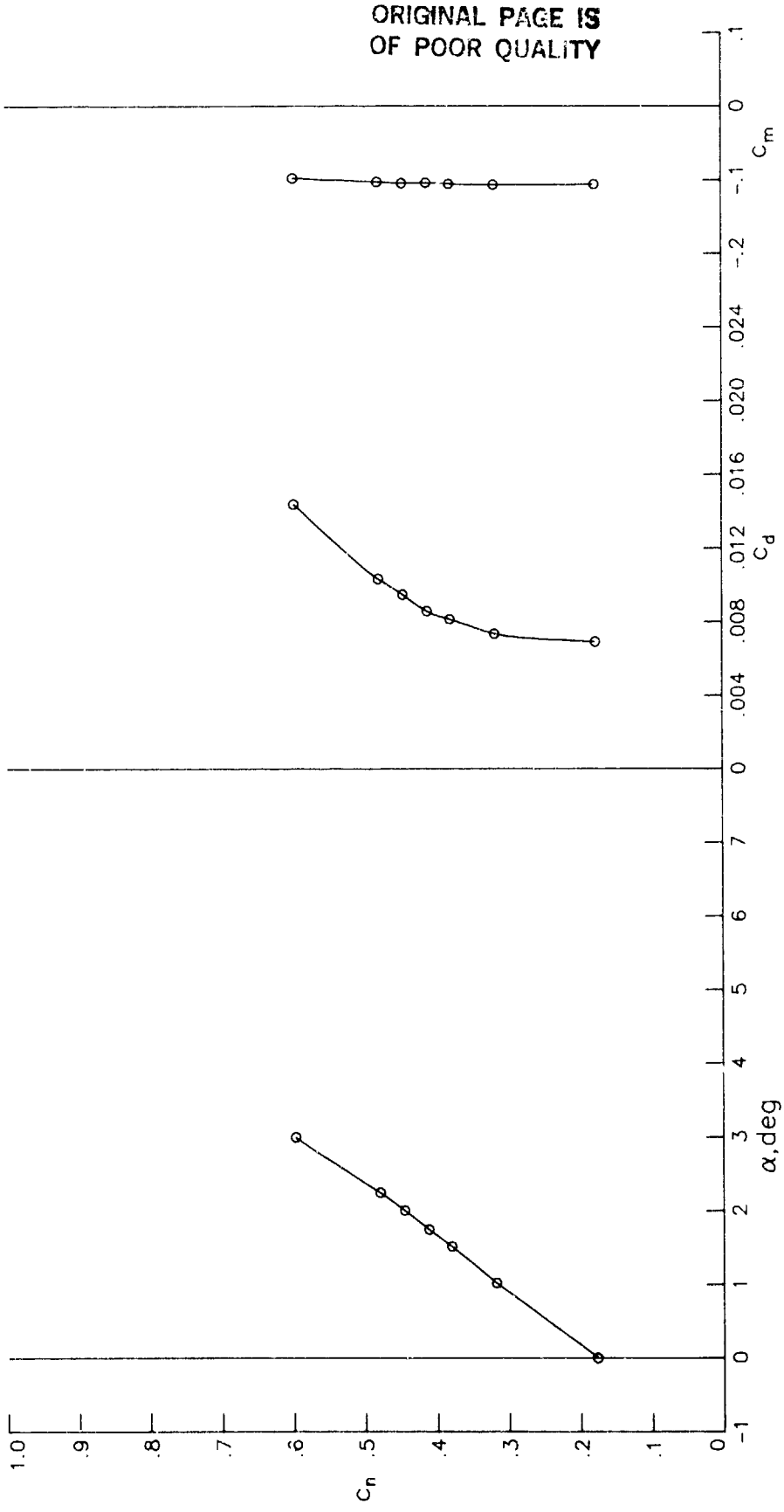

(c) R = 30.20 x 10^6; M = 0.6970.

Figure 9.- Continued.

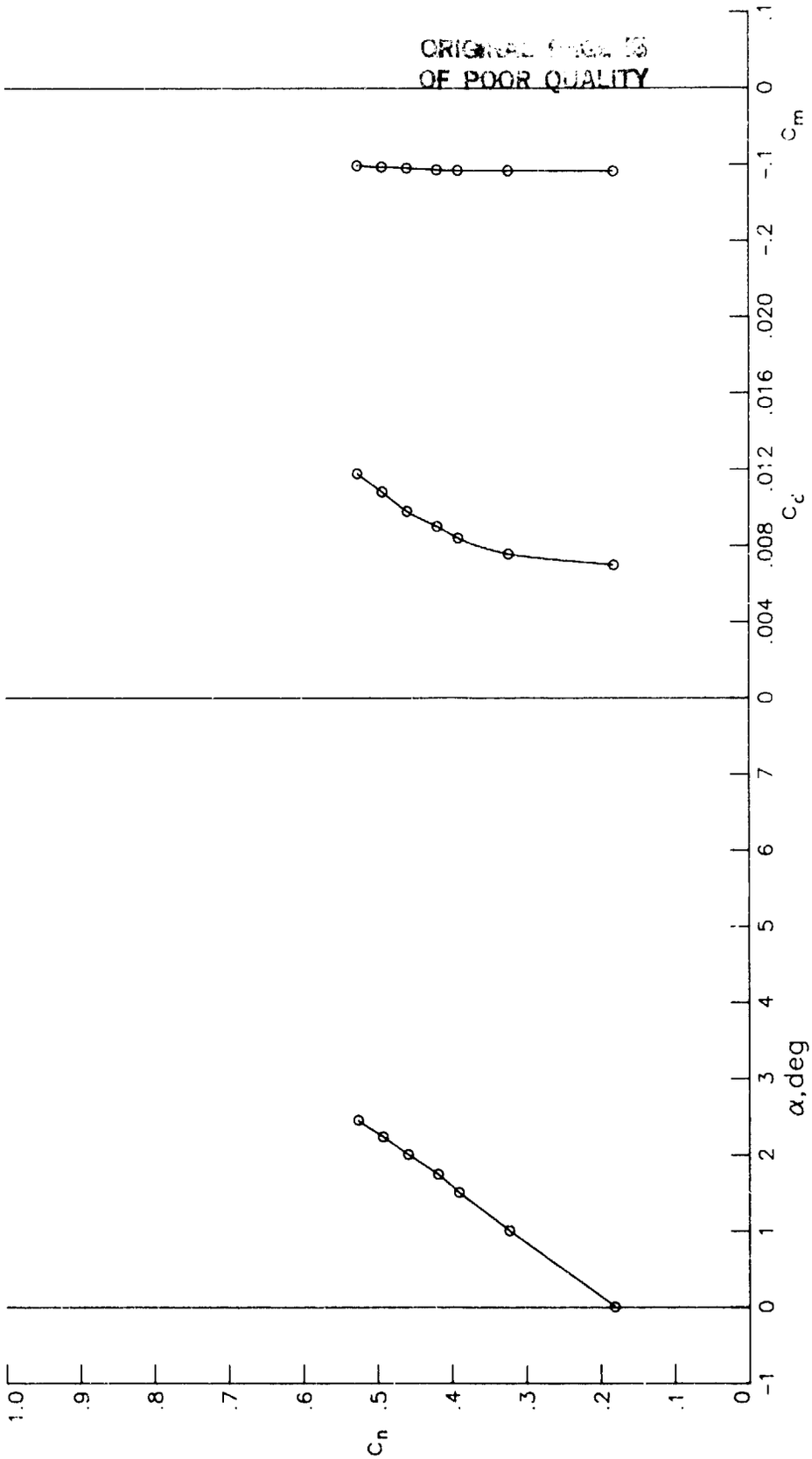

(d) R = 30.09 x 10^6; M = 0.7145.

Figure 9.- Continued.

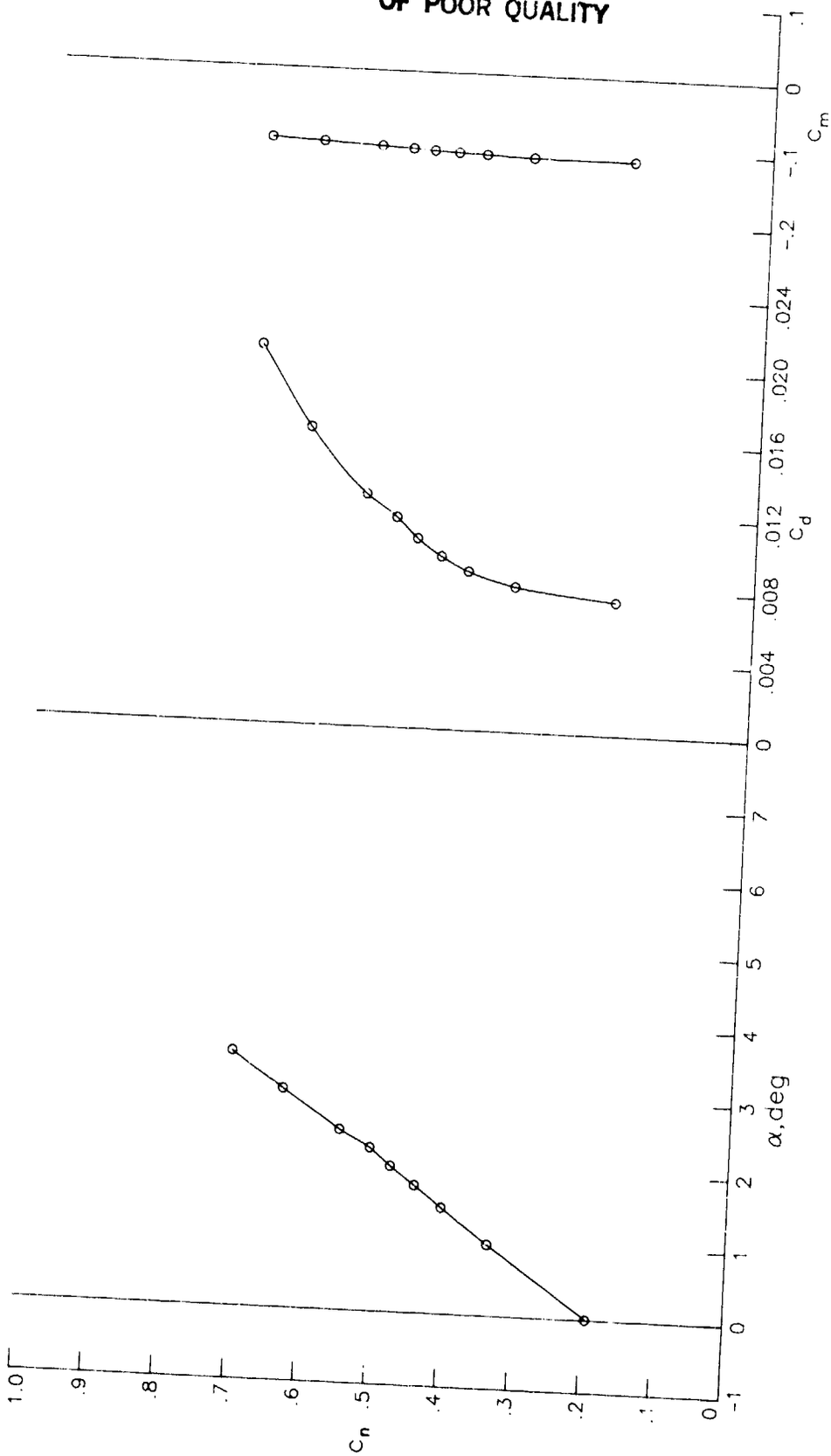

(e) $R = 30.04 \times 10^6$; $M = 0.7351$.

Figure 9.- Continued.

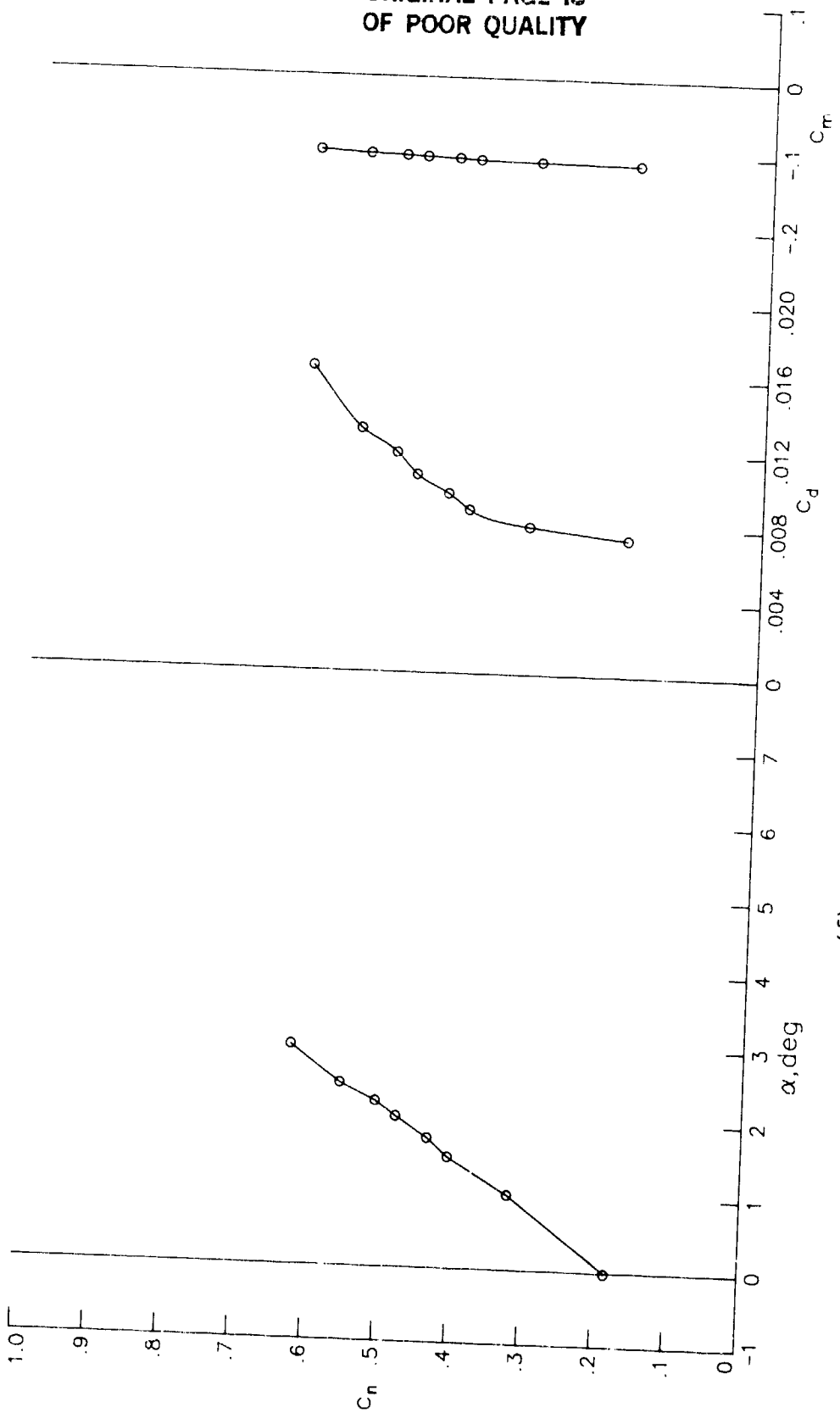

(f) R = 29.62 x 10^6; M = 0.7575.

Figure 9.- Continued.

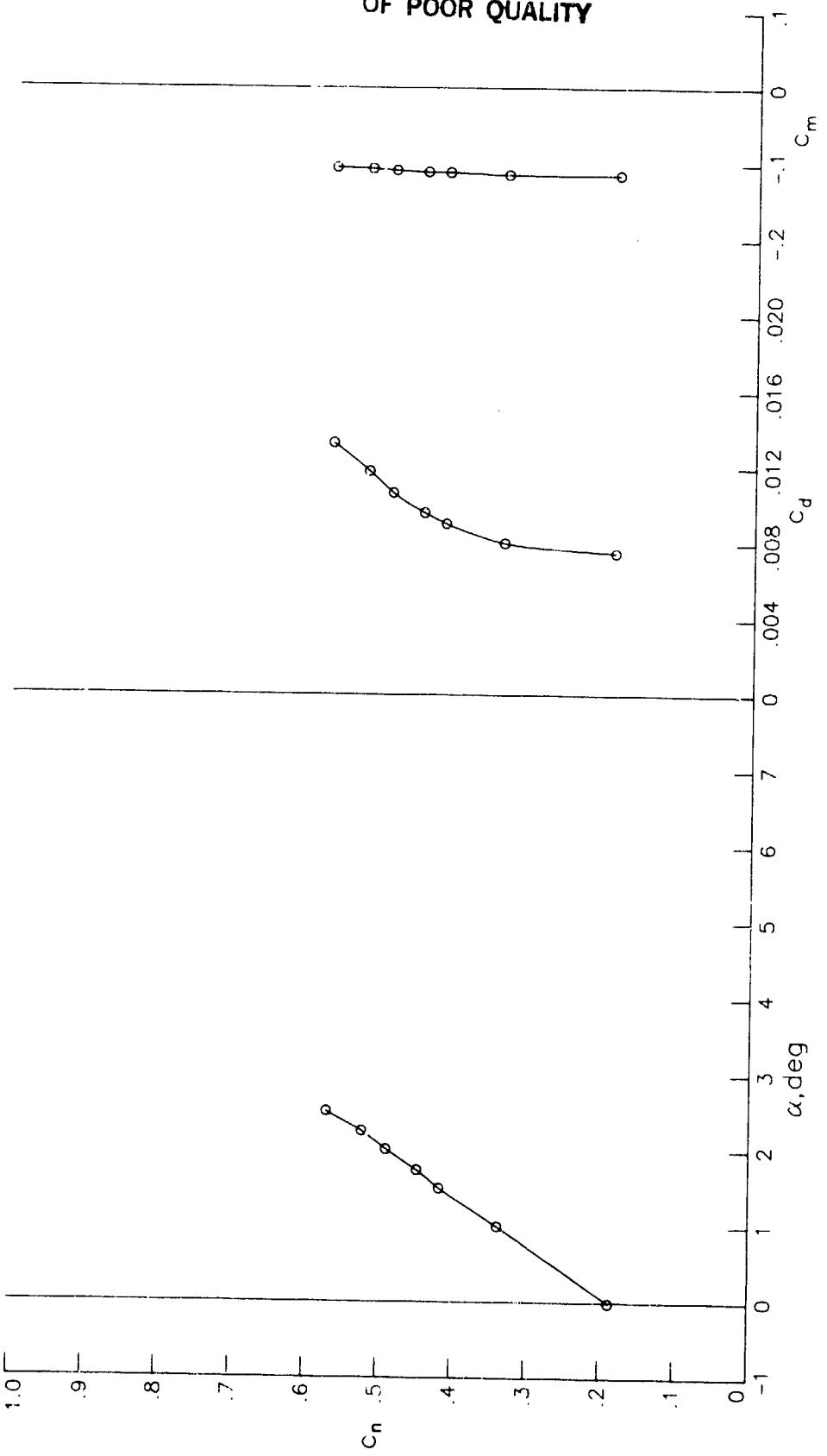

(g) R = 30.07 x 10^6; M = 0.7561.

Figure 9.- Continued.

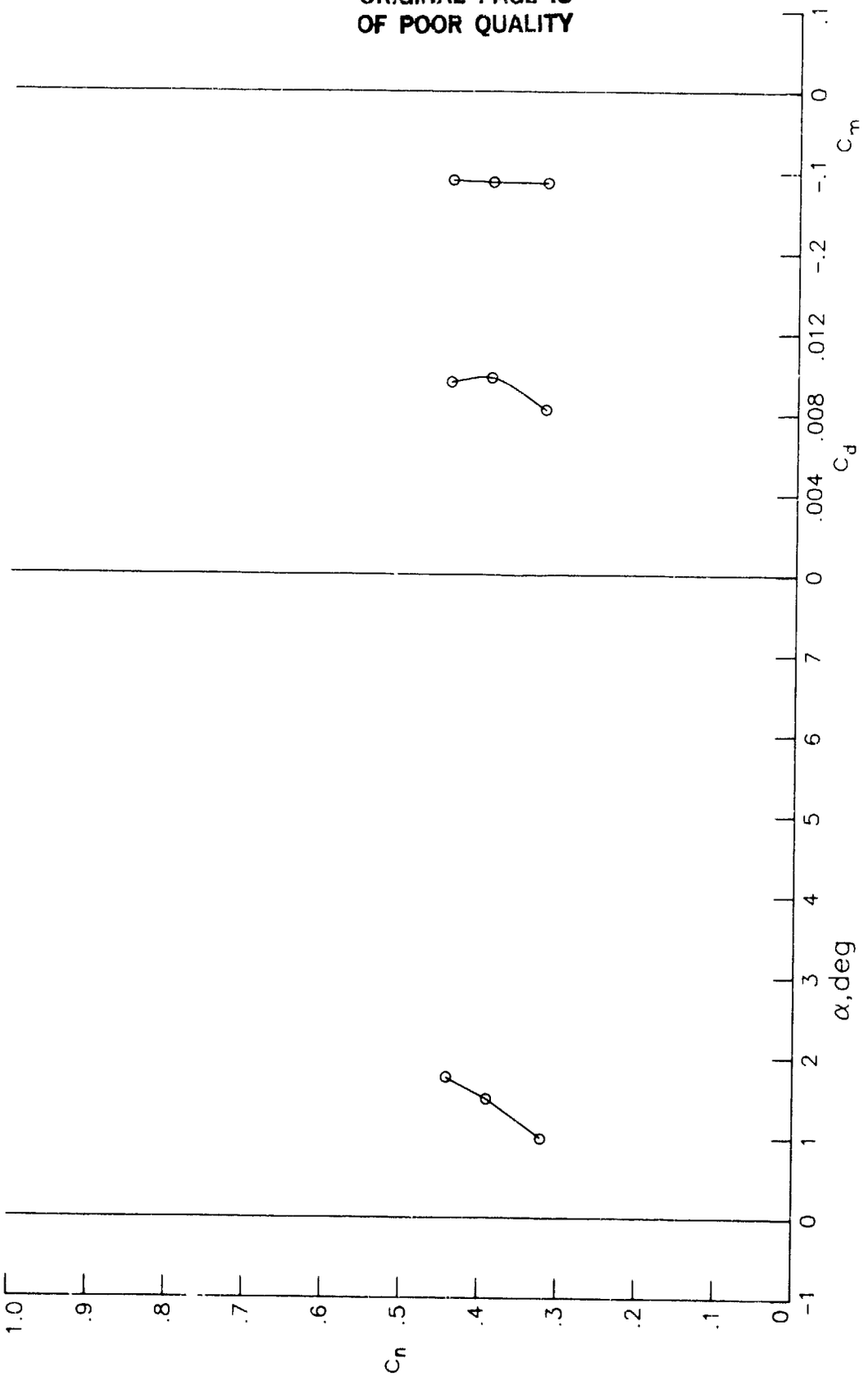

(h) R = 29.88 x 10^6; M = 0.7743.

Figure 9.- Continued.

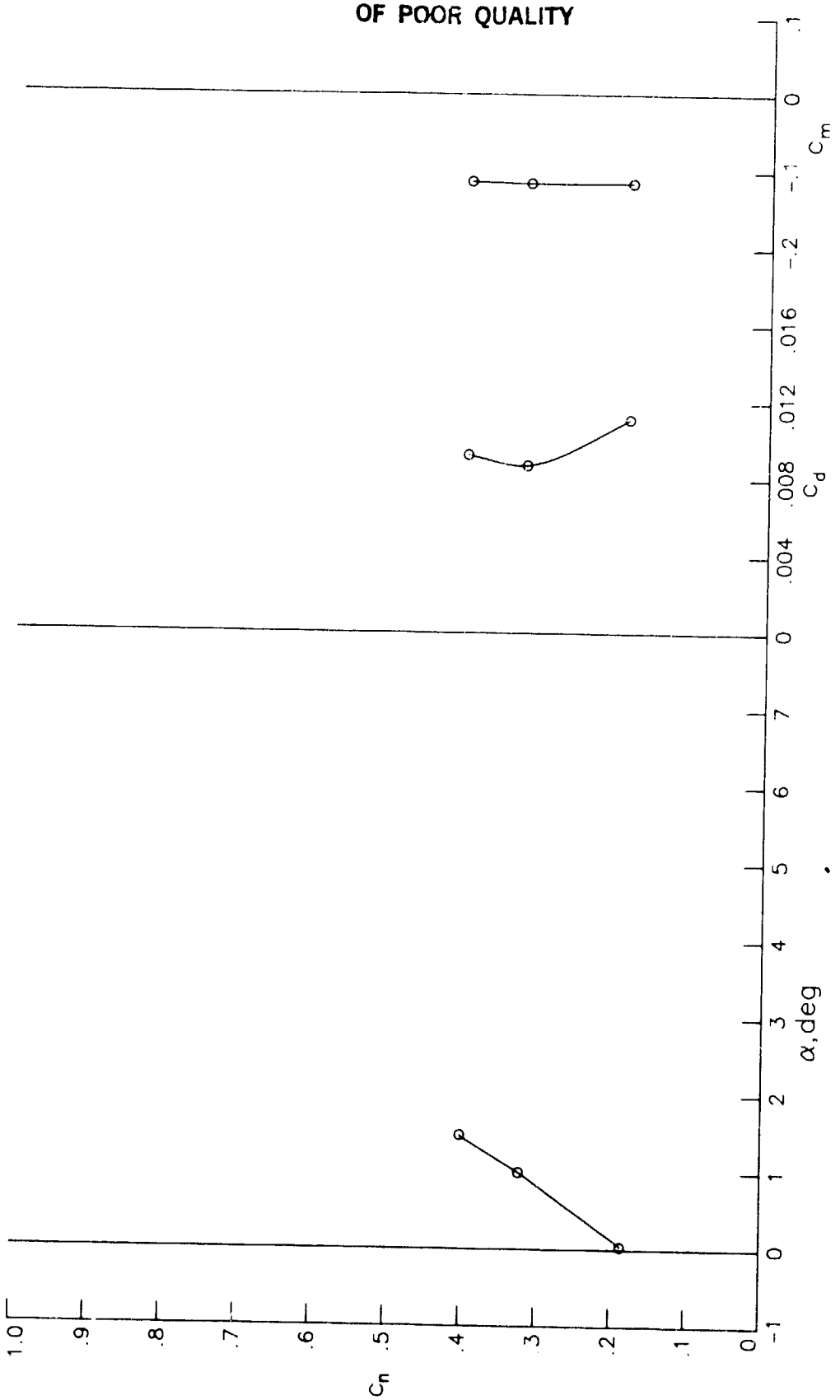

(i) R = 30.03 x 10^6; M = 0.7933.

Figure 9.- Continued.

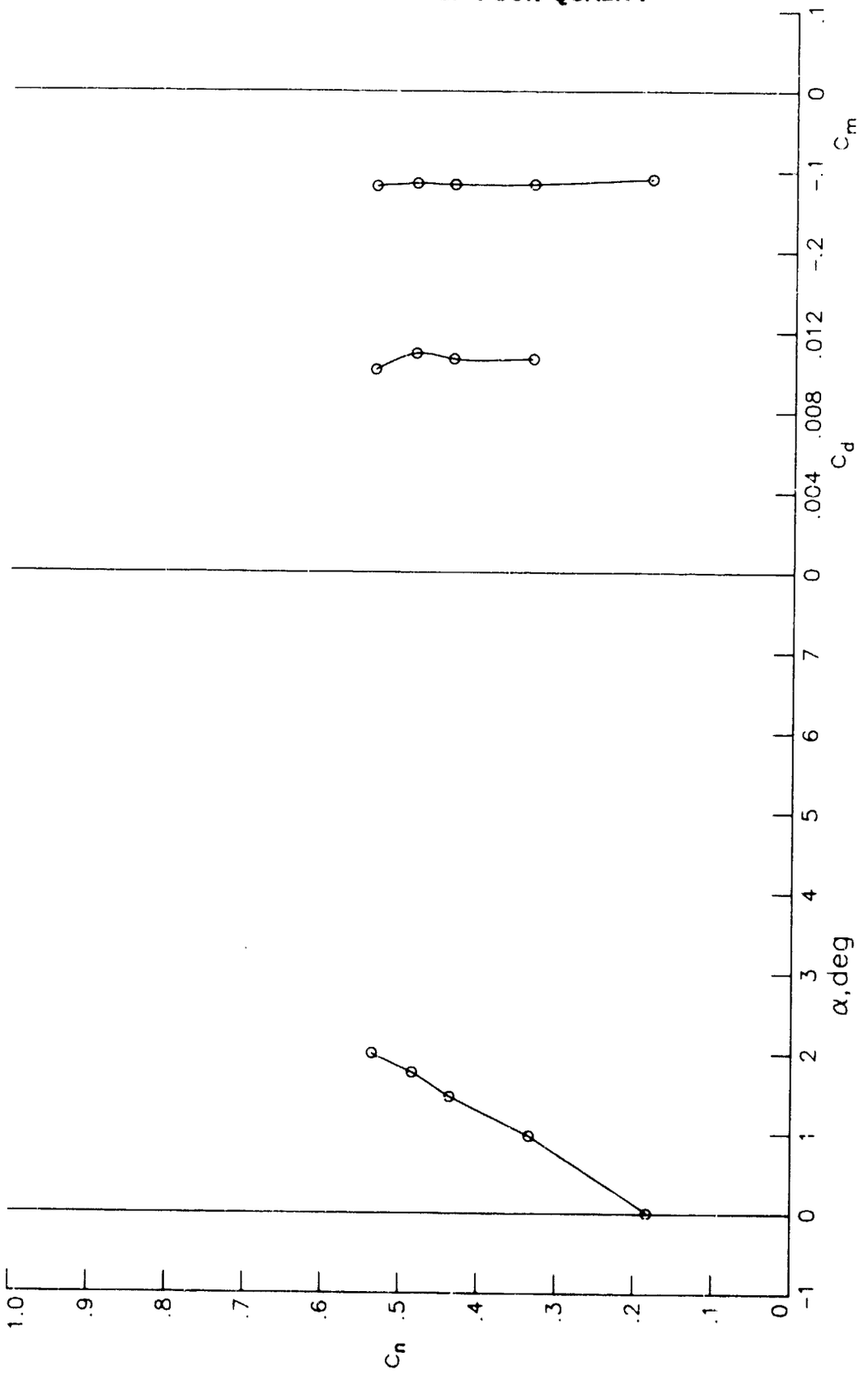

(j) R = 30.04 x 10^6; M = 0.8155.

Figure 9.- Concluded.

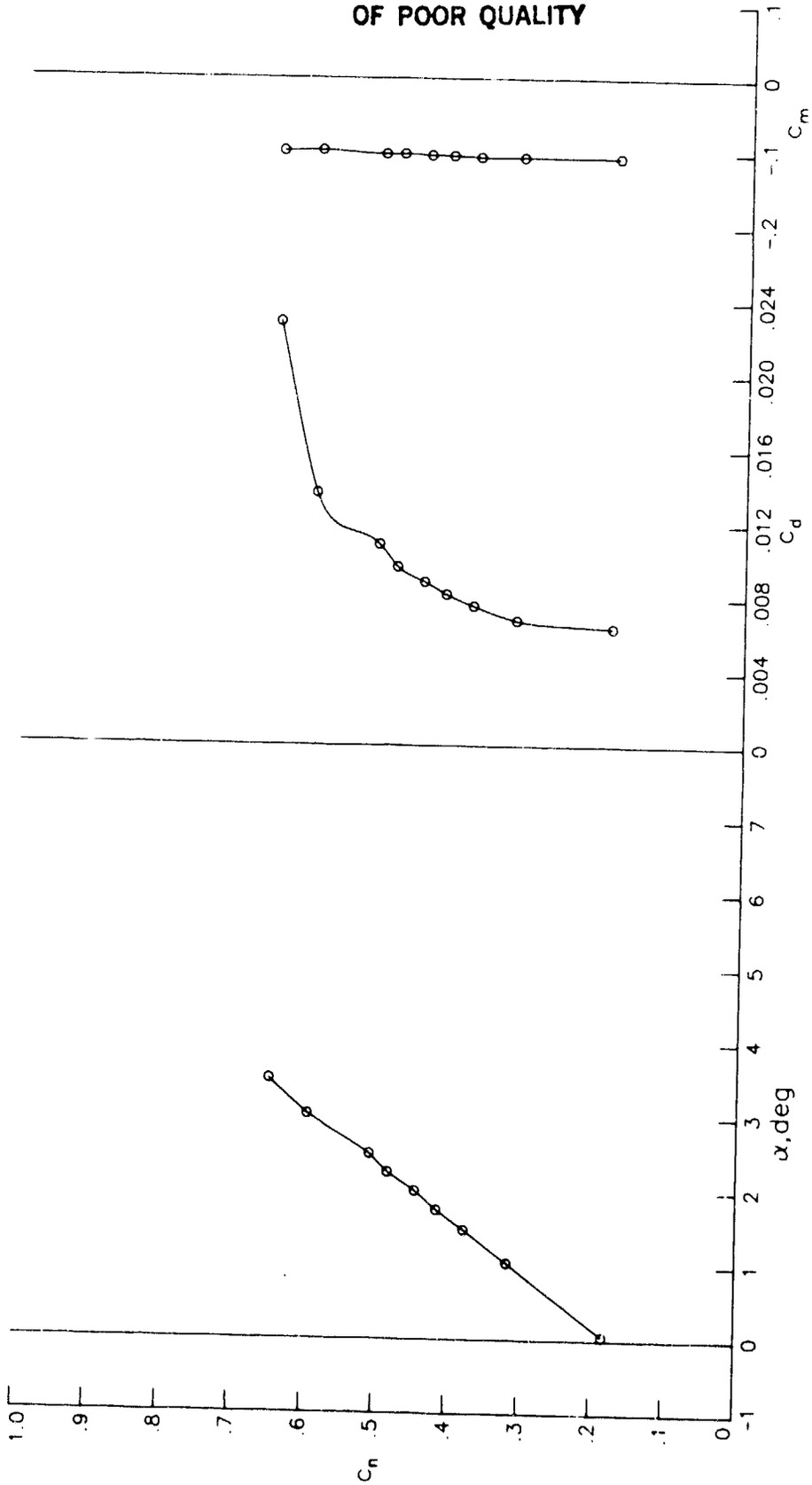

(a) R = 47.63 × 10^6; M = 0.6990.

Figure 10.- Section characteristics at Reynolds numbers above 47 × 10^6.

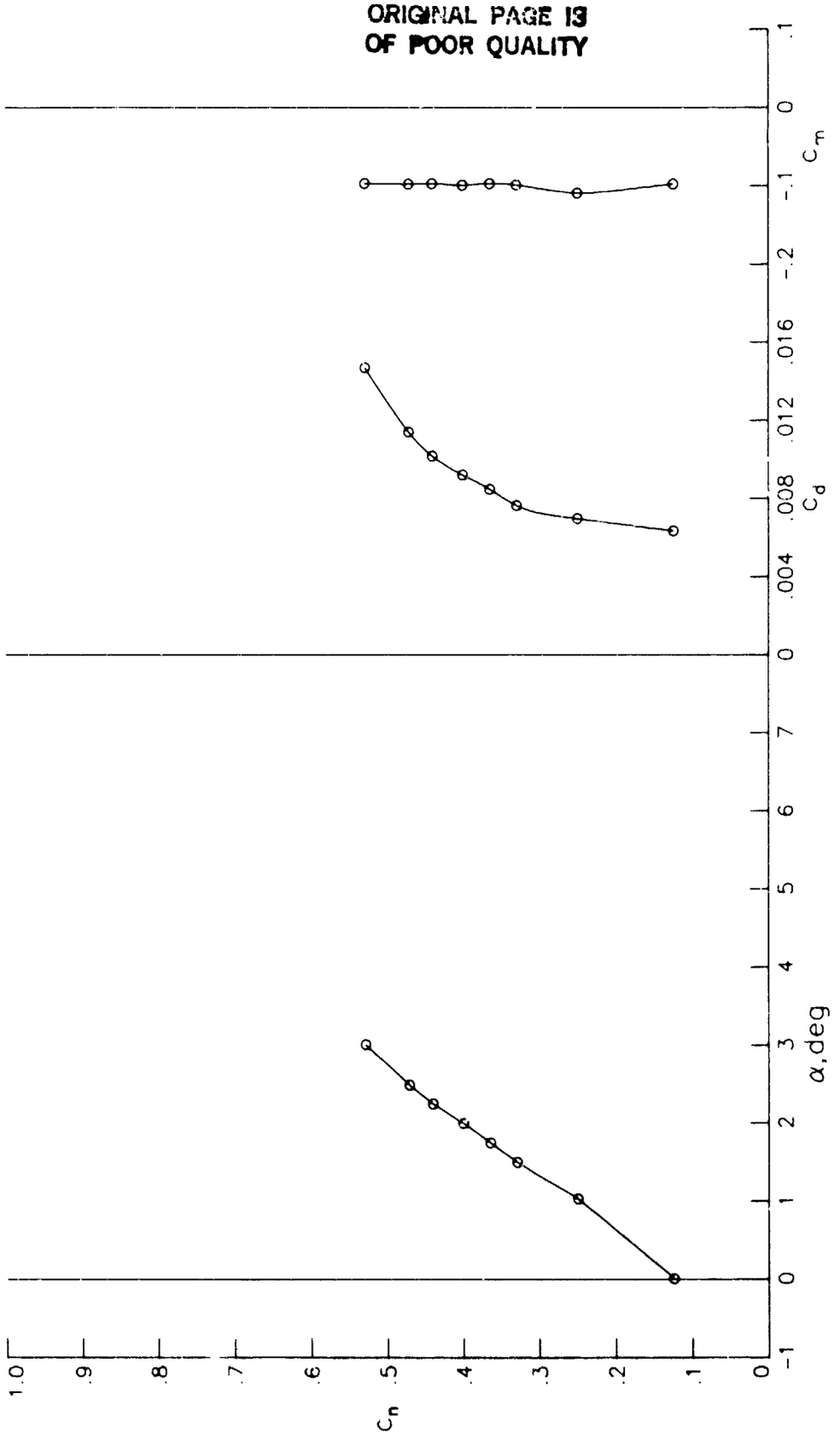

(b) R = 47.72 x 10^6; M = 0.7188.

Figure 10.- Continued.

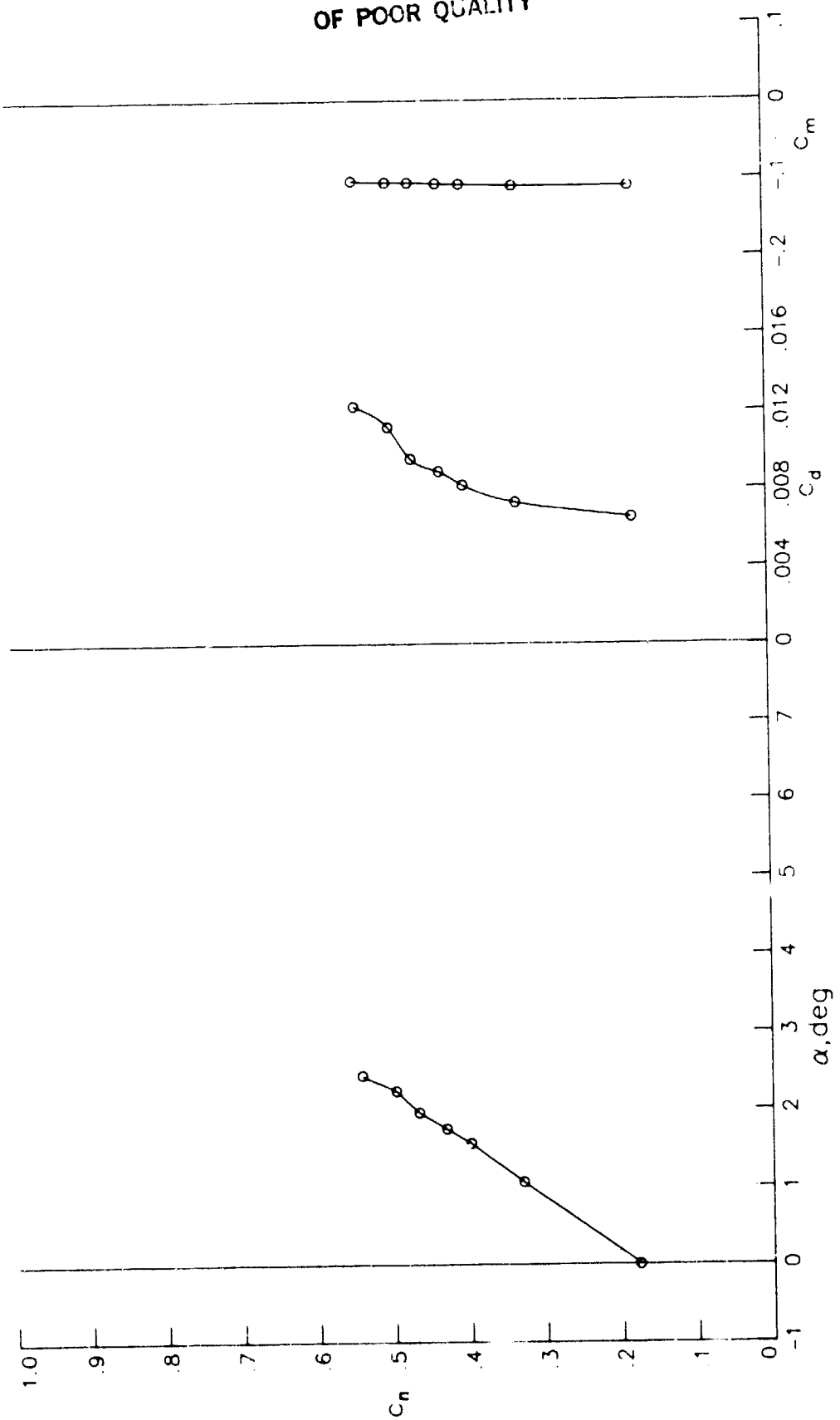

(c) R = 47.60 x 10^6; M = 0.7366.

Figure 10.- Continued.

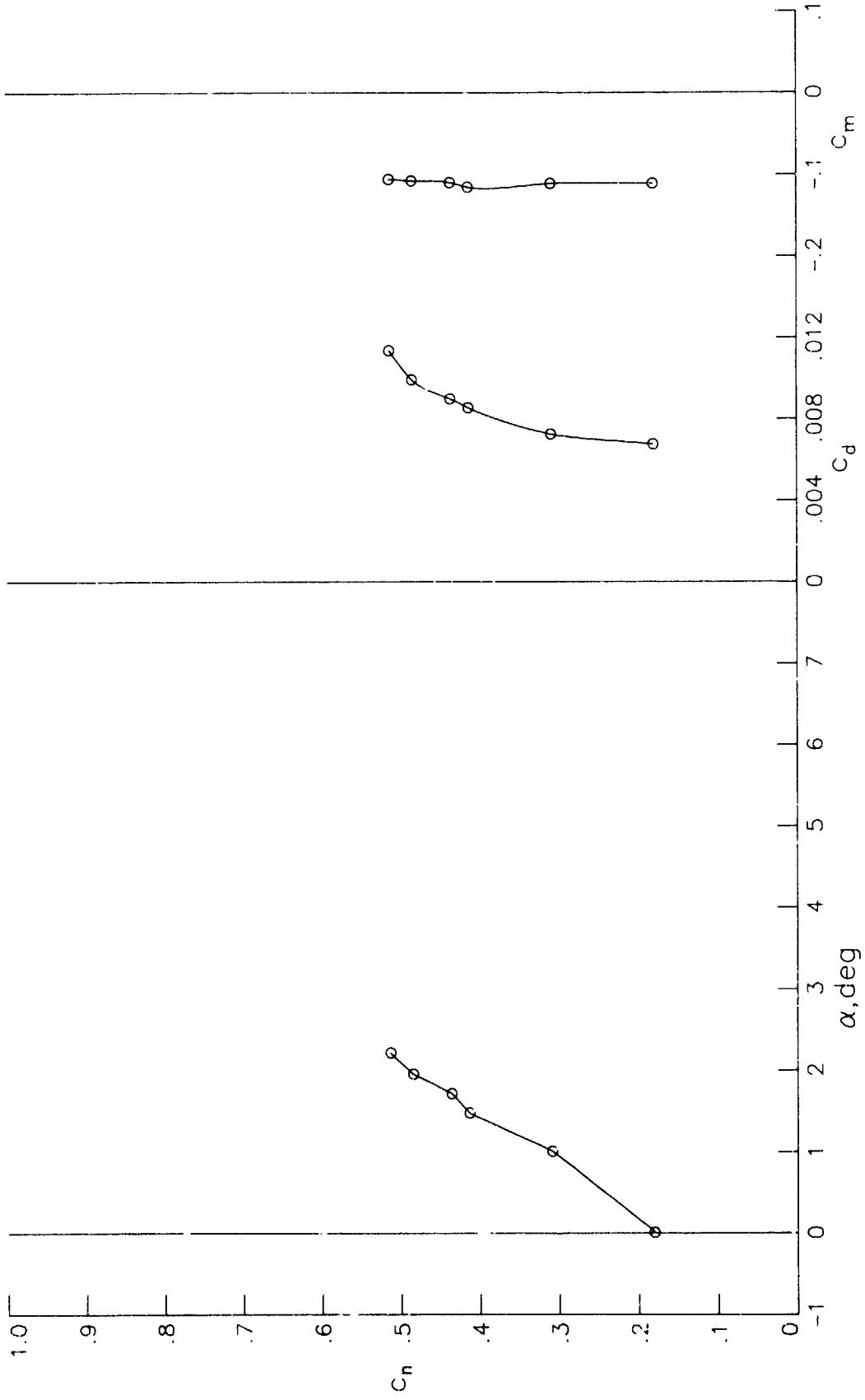

(d) R = 47.55 × 10^6; M = 0.7580.

Figure 10.- Continued.

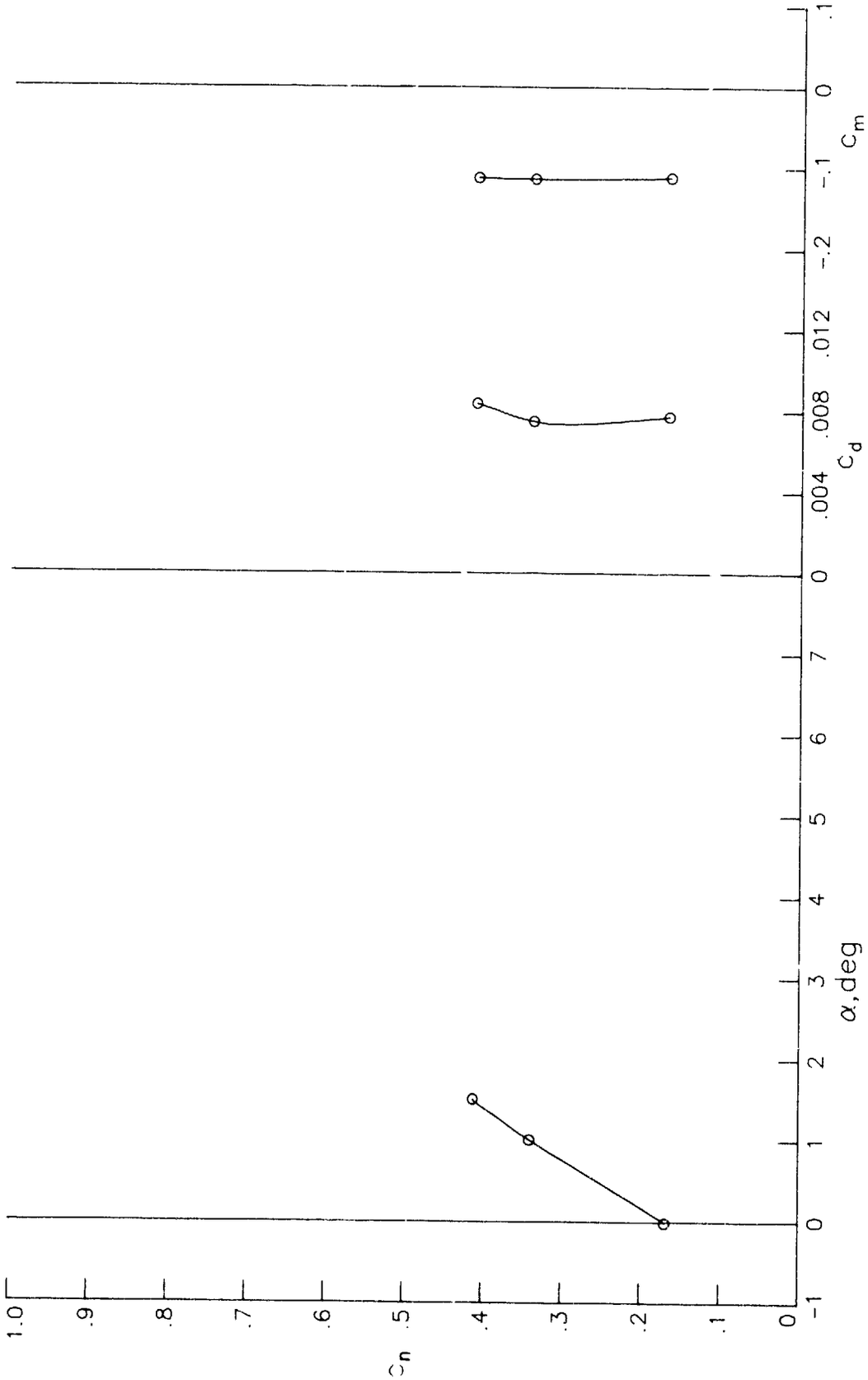

(e) R = 47.47 × 10^6; M = 0.7763.

Figure 10.- Concluded.

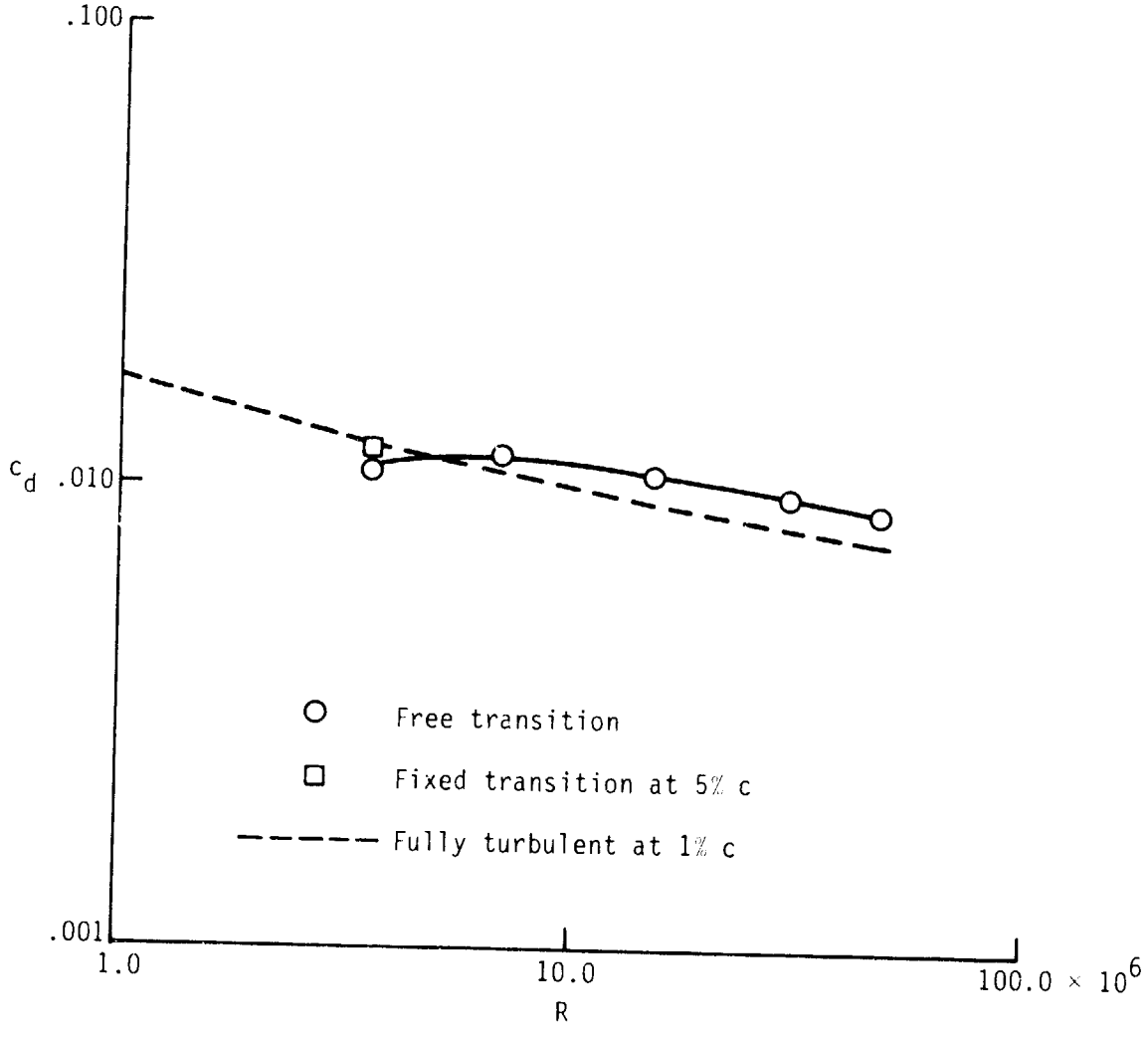

Figure 11.- Effect of free and fixed transition on section drag coefficient.

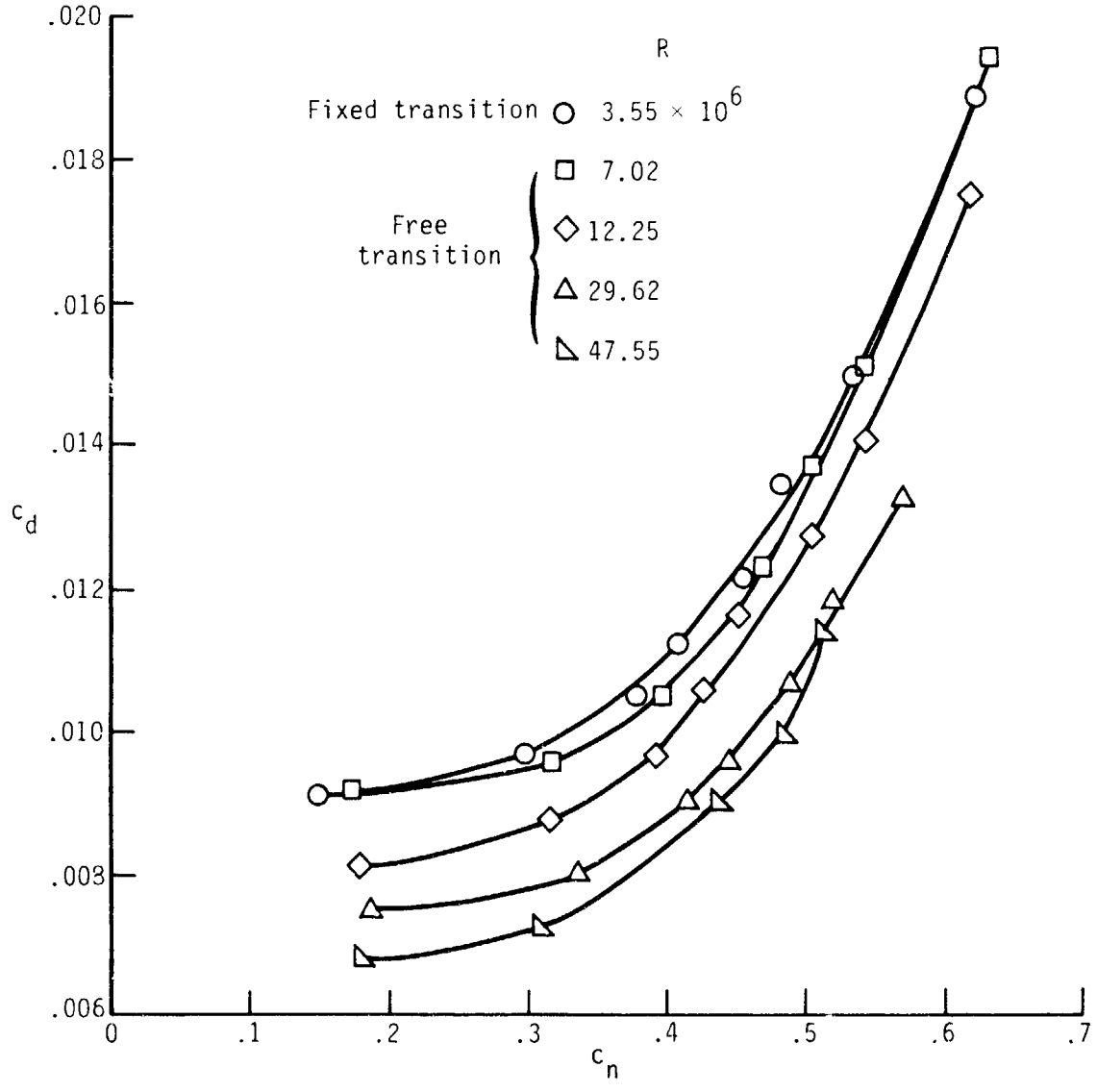

Figure 12.- Effect of Reynolds number on drag polars for M = 0.755.

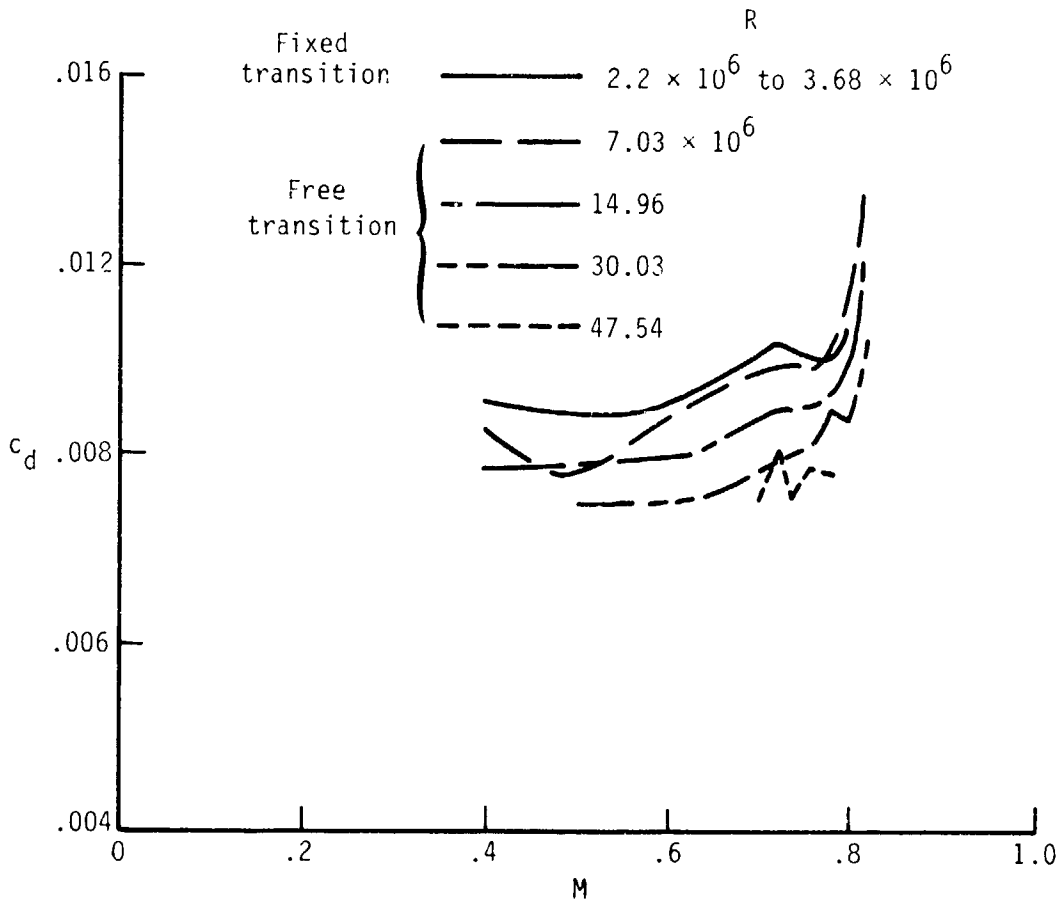

(a) $c_n = 0.35$.

Figure 13.- Effect of Reynolds number of drag-rise Mach number.

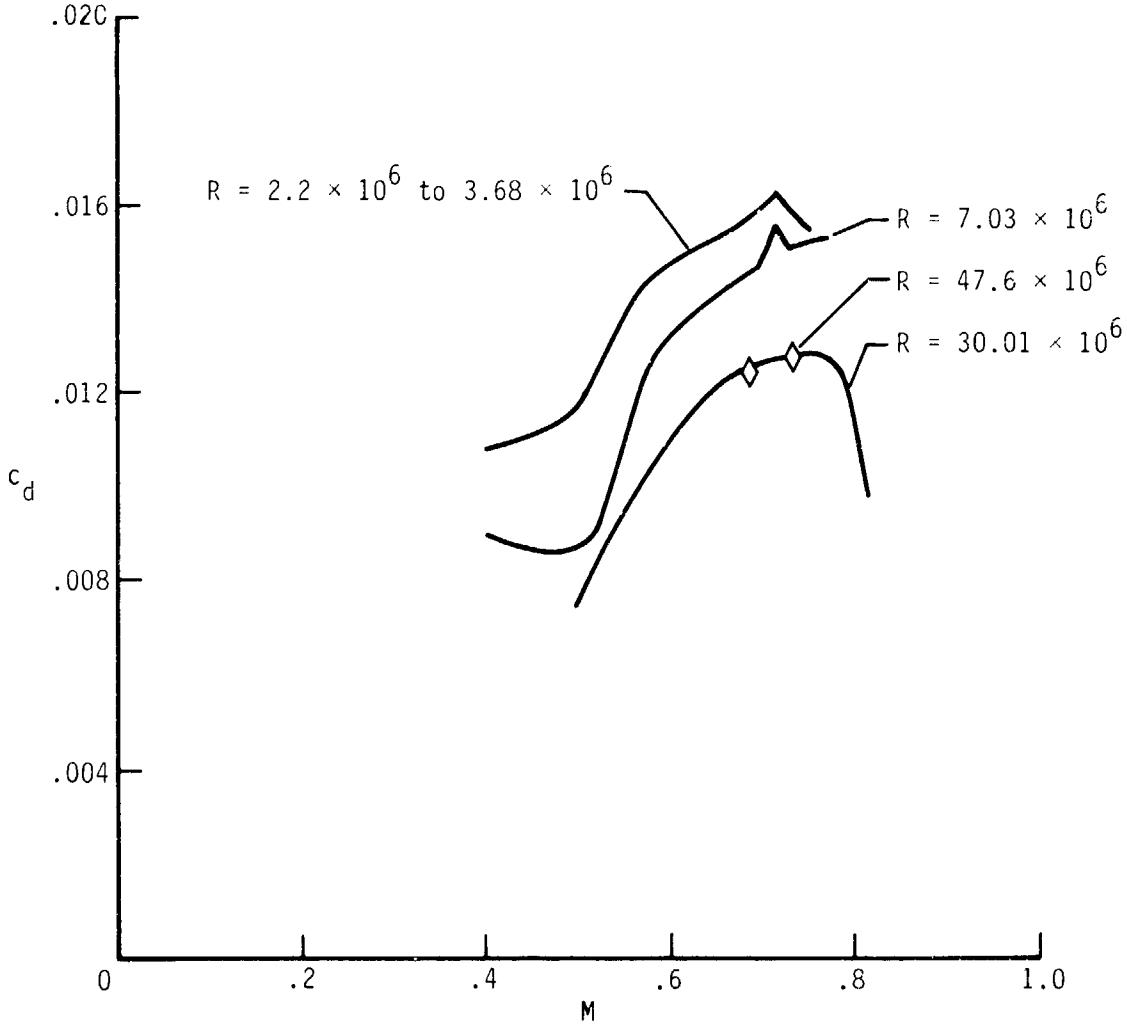

(b) c_n = 0.55.

Figure 13.- Concluded.

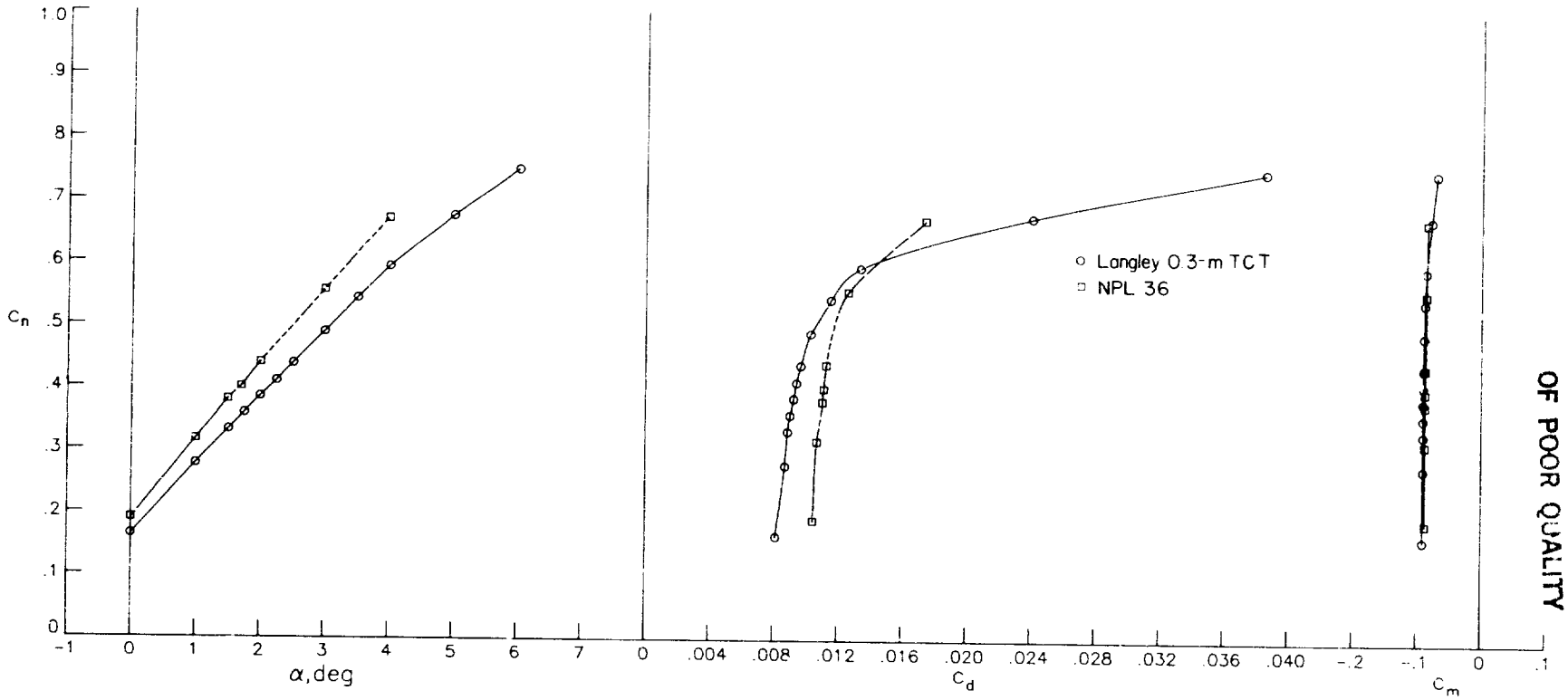

(a) $R = 2.66 \times 10^6$ and $M = 0.499$ from Langley data; $R = 2.50 \times 10^6$ and $M = 0.499$ from NPL data.

Figure 14.- Comparison of Langley coefficient data and NPL coefficient data.

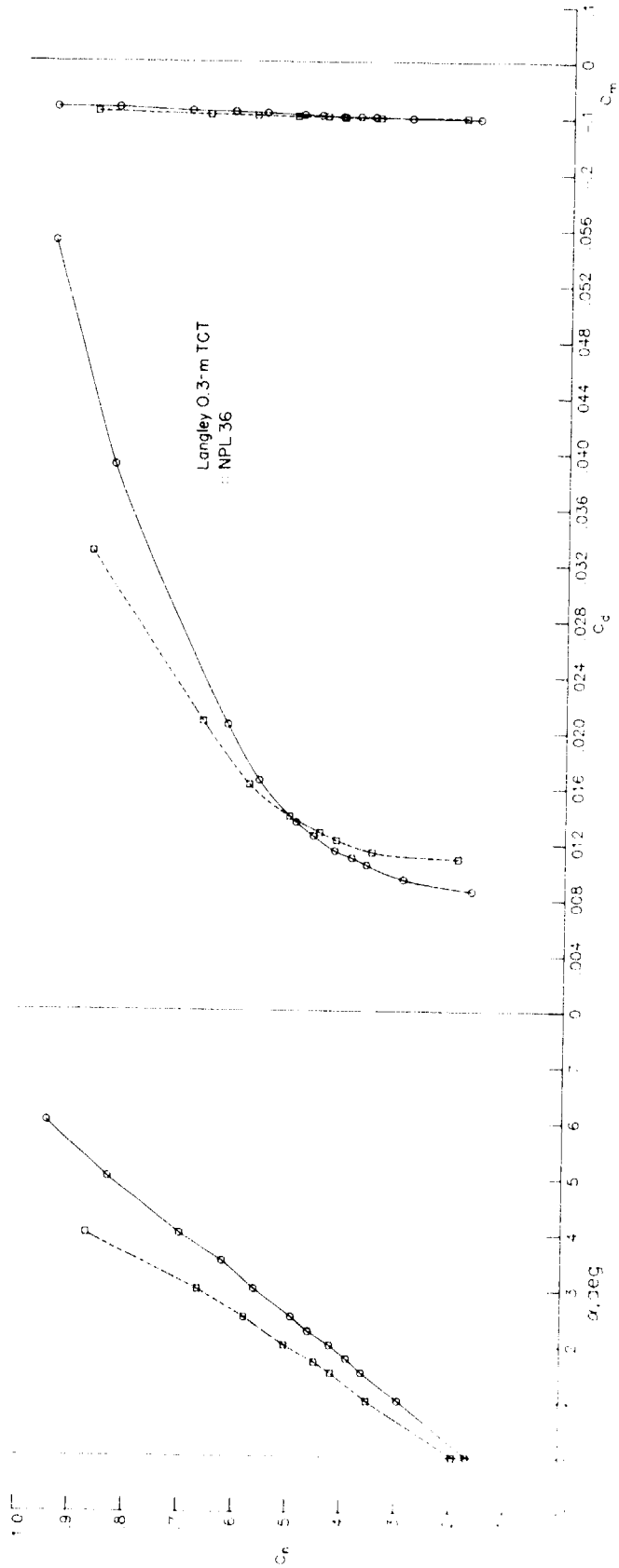

(b) R = 3.38 × 10^6 and M = 0.697 from Langley data; R = 3.20 × 10^6 and M = 0.699 from NPL data.

Figure 14.- Concluded.

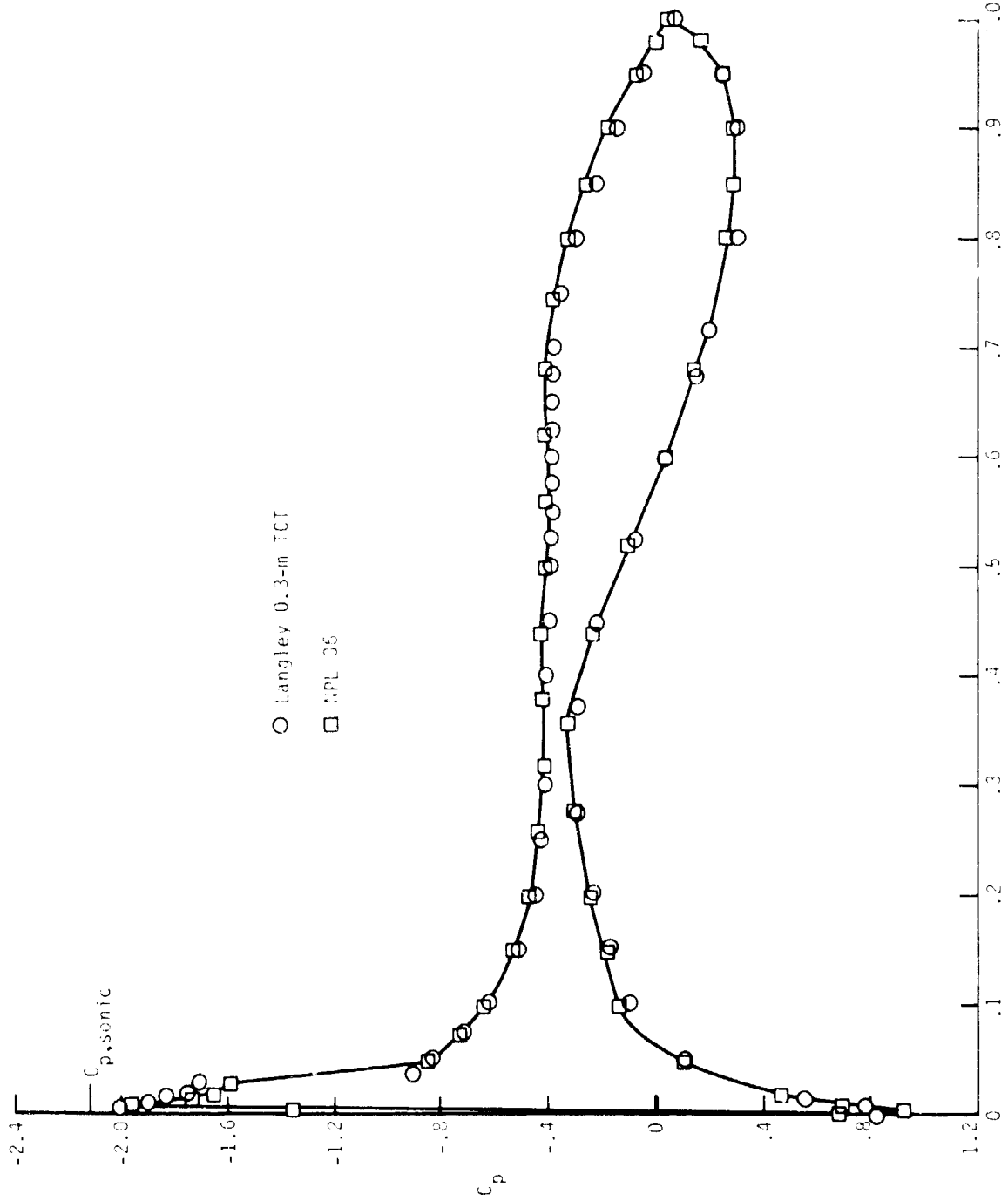

(a) M = 0.5; C_n = 0.44; R = 2.6 × 10^6; α = 2.0° from Langley data and α = 2.51° from NPL data.

Figure 15.- Comparison of pressure distributions from Langley data and NPL data.

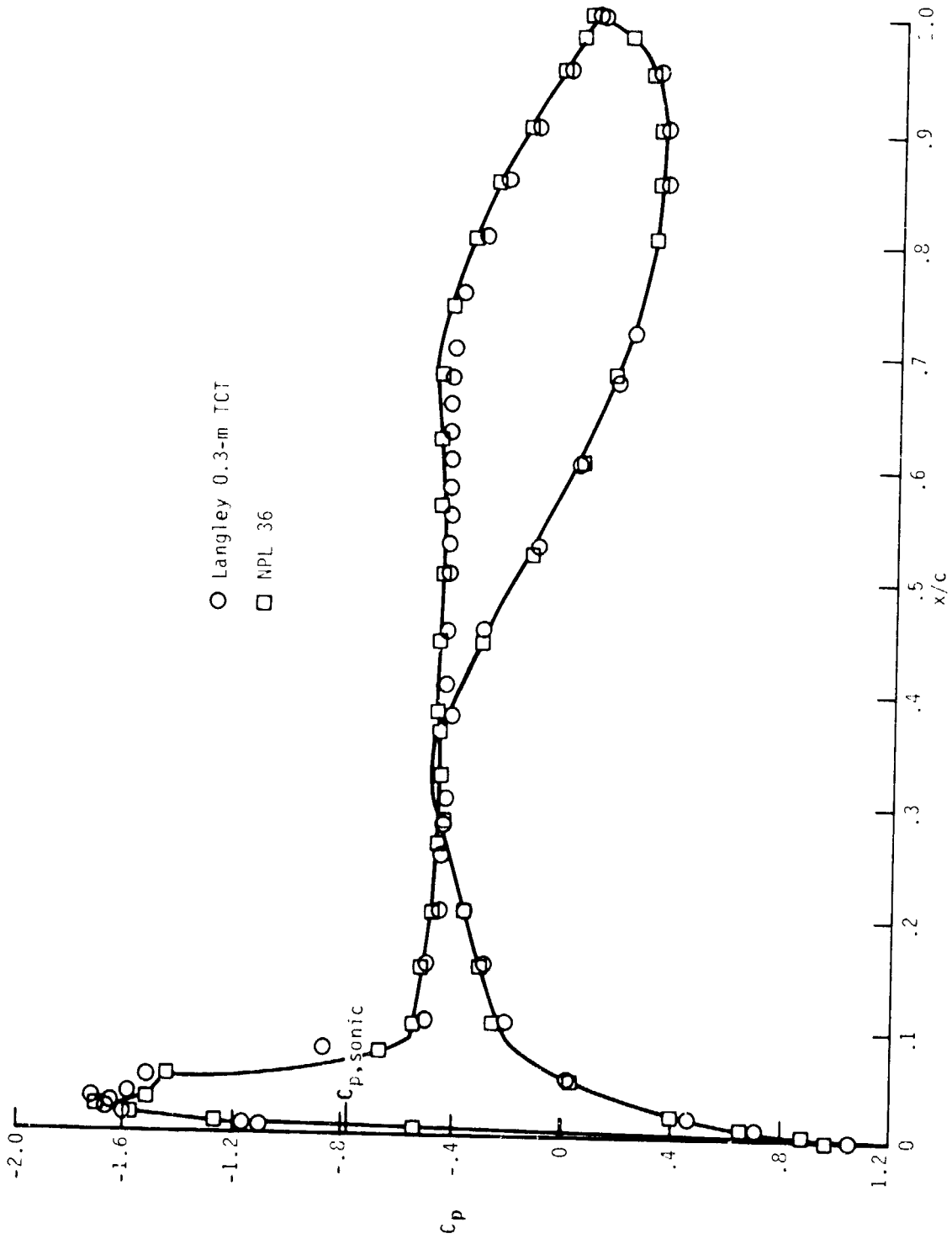

(b) M = 0.7; c_n = 0.42; R = 3.3 × 10^6; α = 2.00° from Langley data and α = 1.5° from NPL data.

Figure 15.- Concluded.

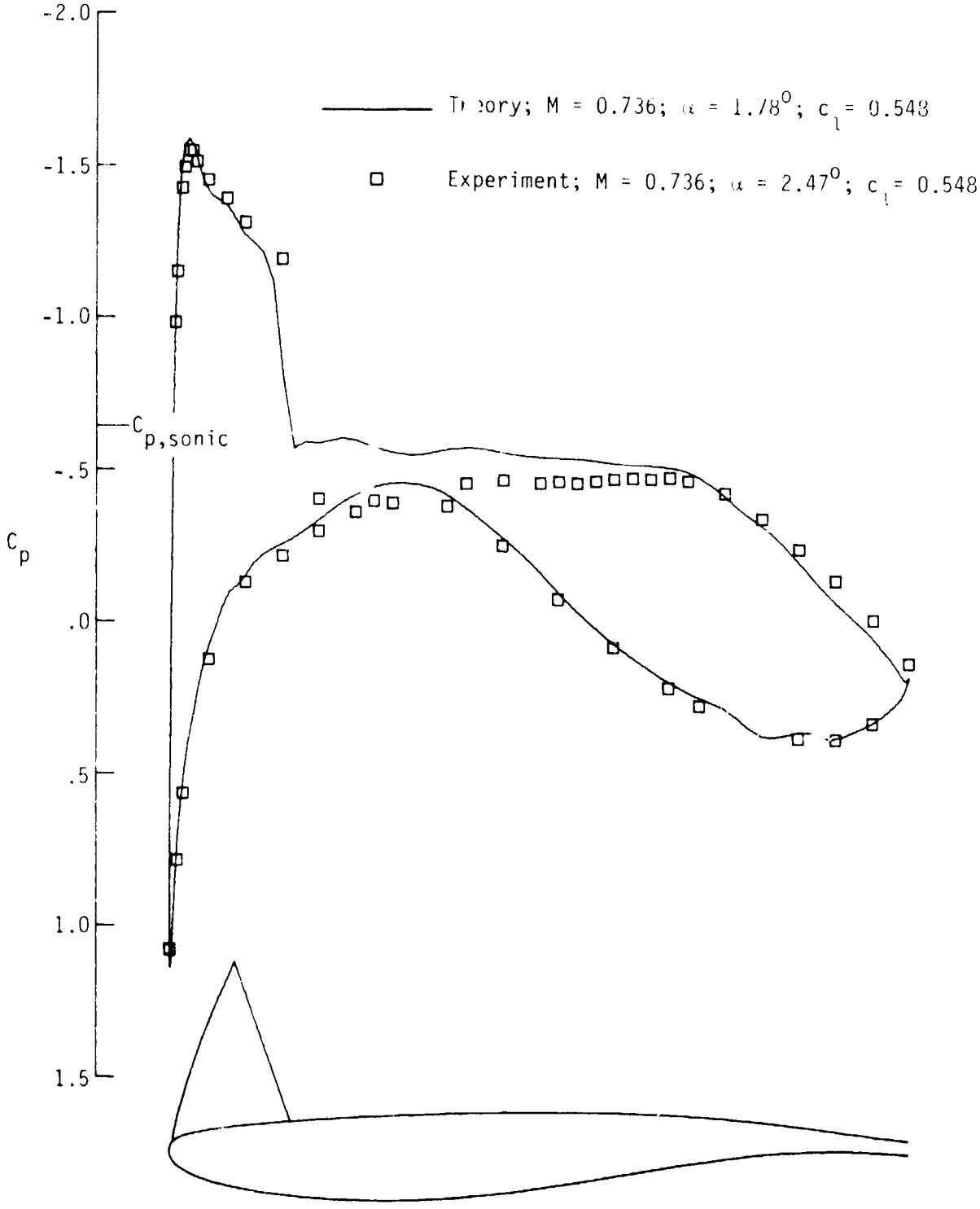

(a) Midrange of Mach number.

Figure 16.- Comparison of experimental and theoretical pressure distributions.

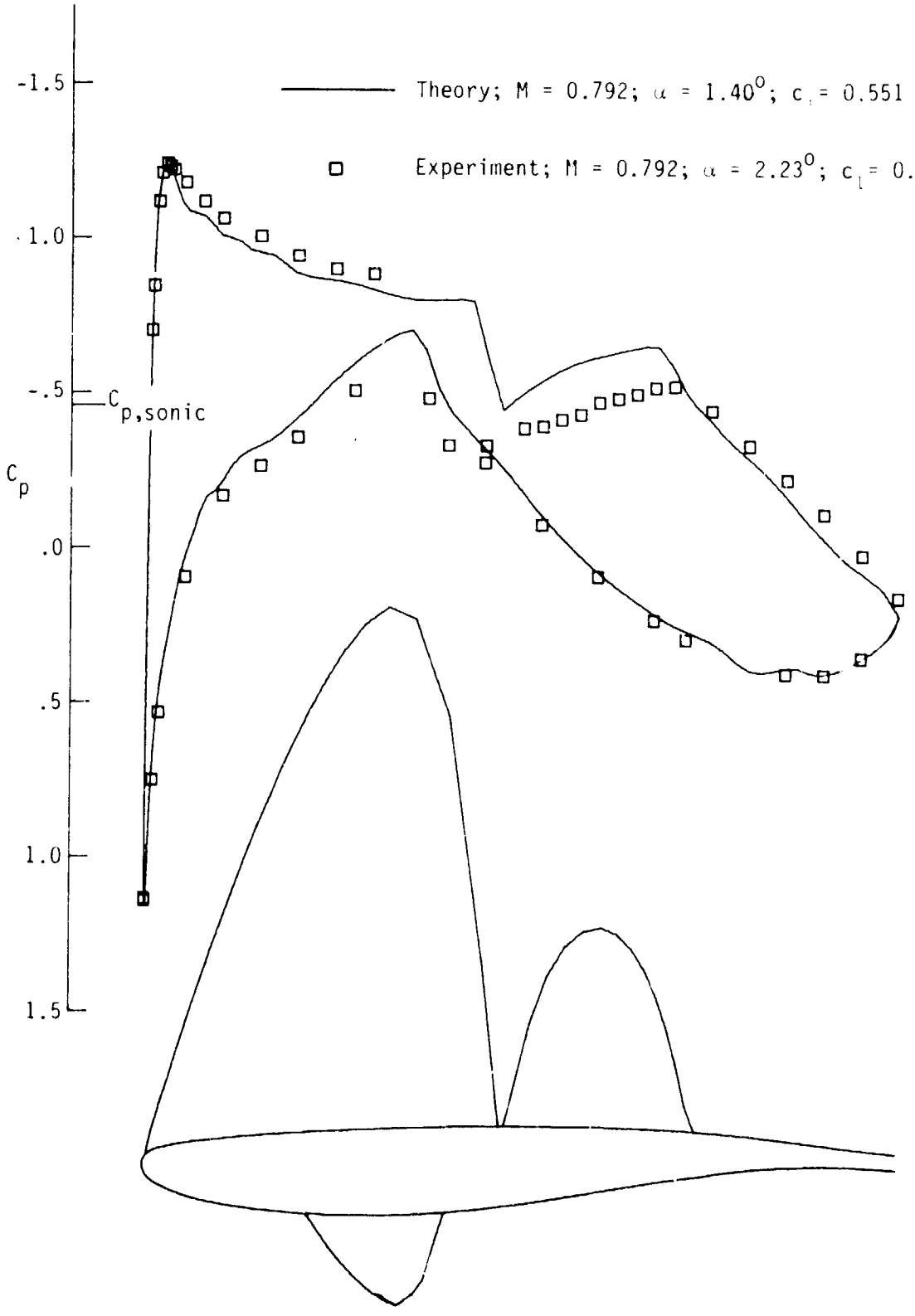

(b) Upper range of Mach number.

Figure 16.- Concluded.

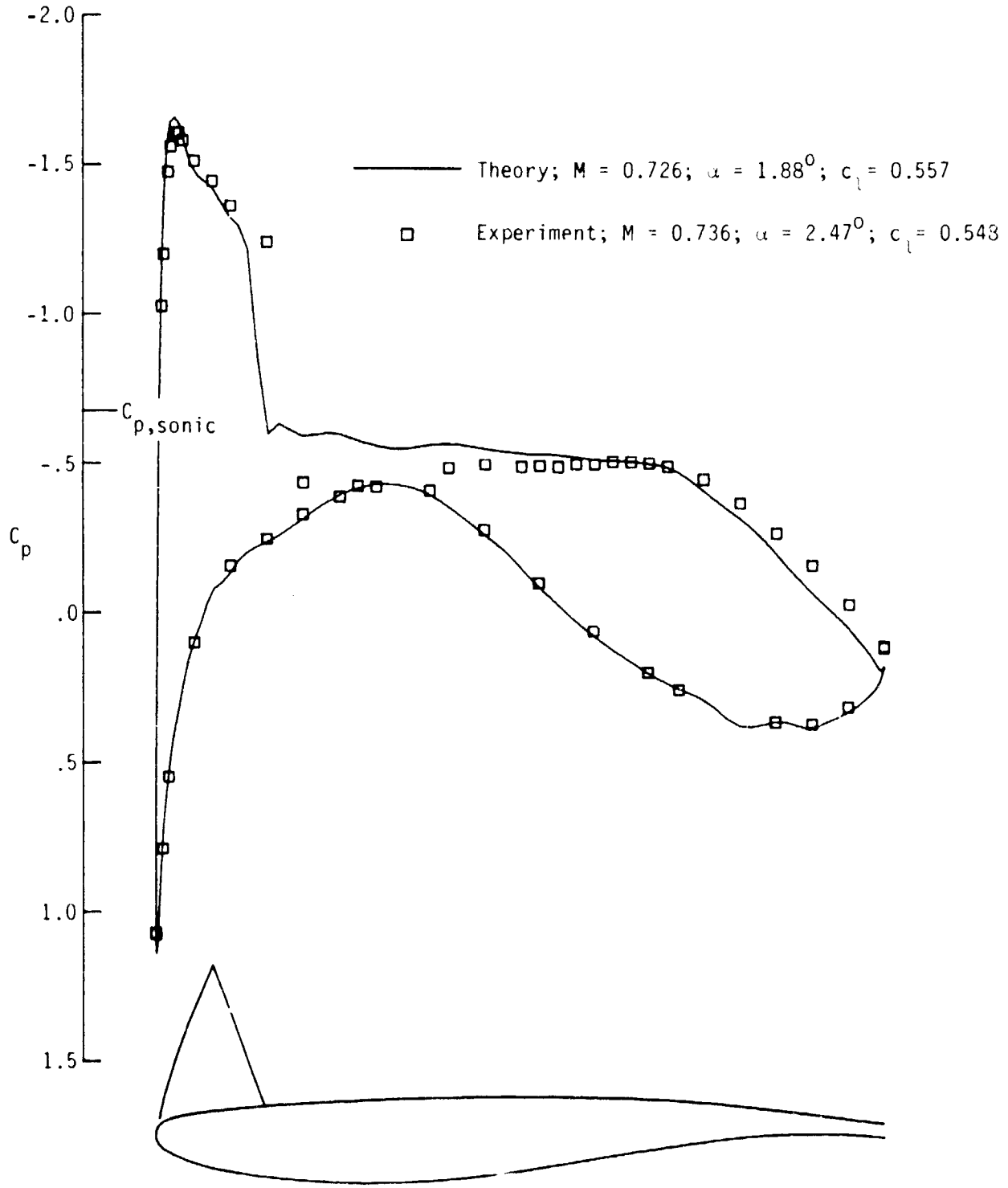

(a) Midrange of Mach number.

Figure 17.- Comparison ot theoretical and experimental pressure distributions for corrected Mach numbers and lift coefficients.

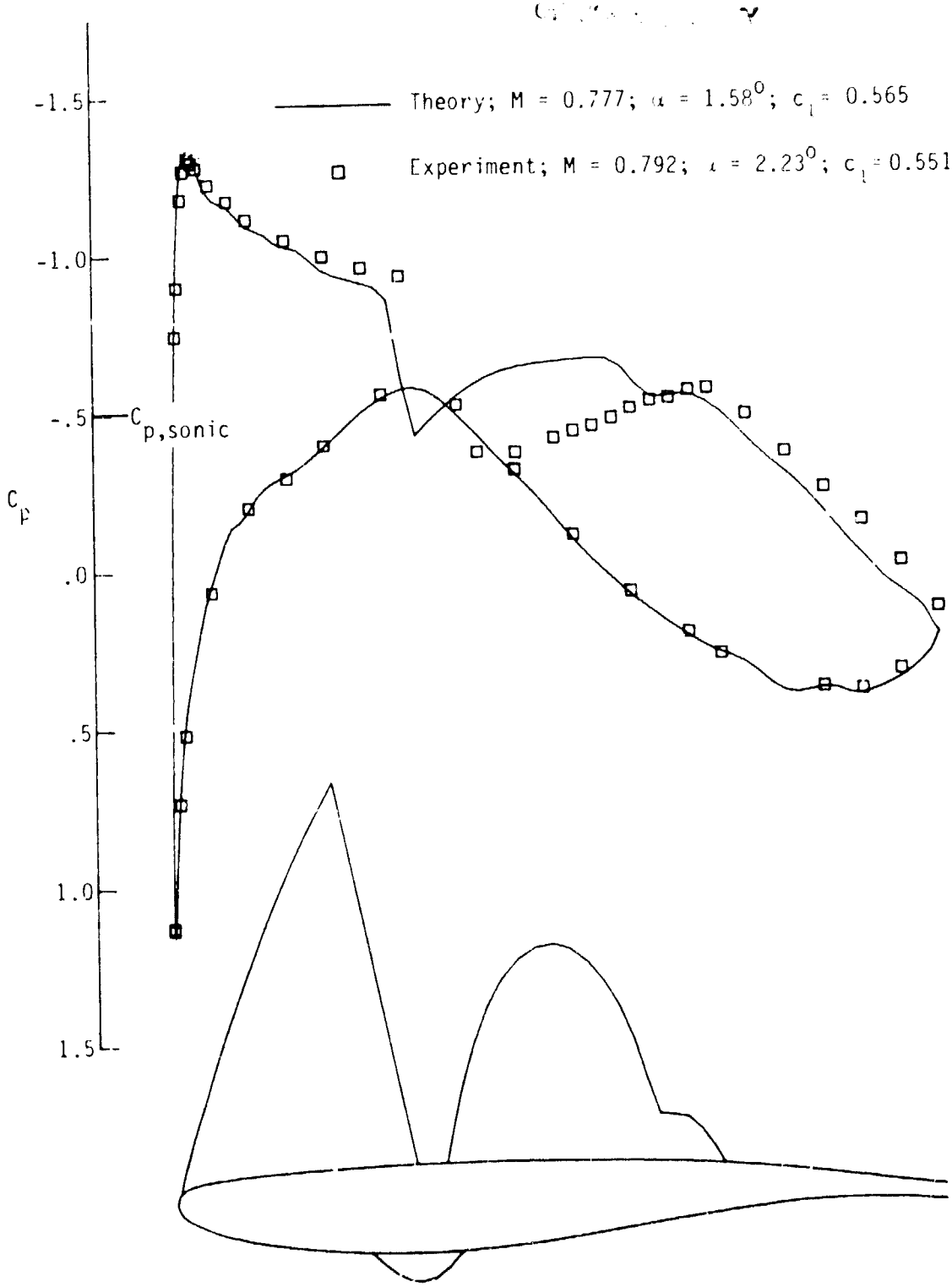

(b) Upper range of Mach number.

Figure 17.- Concluded.

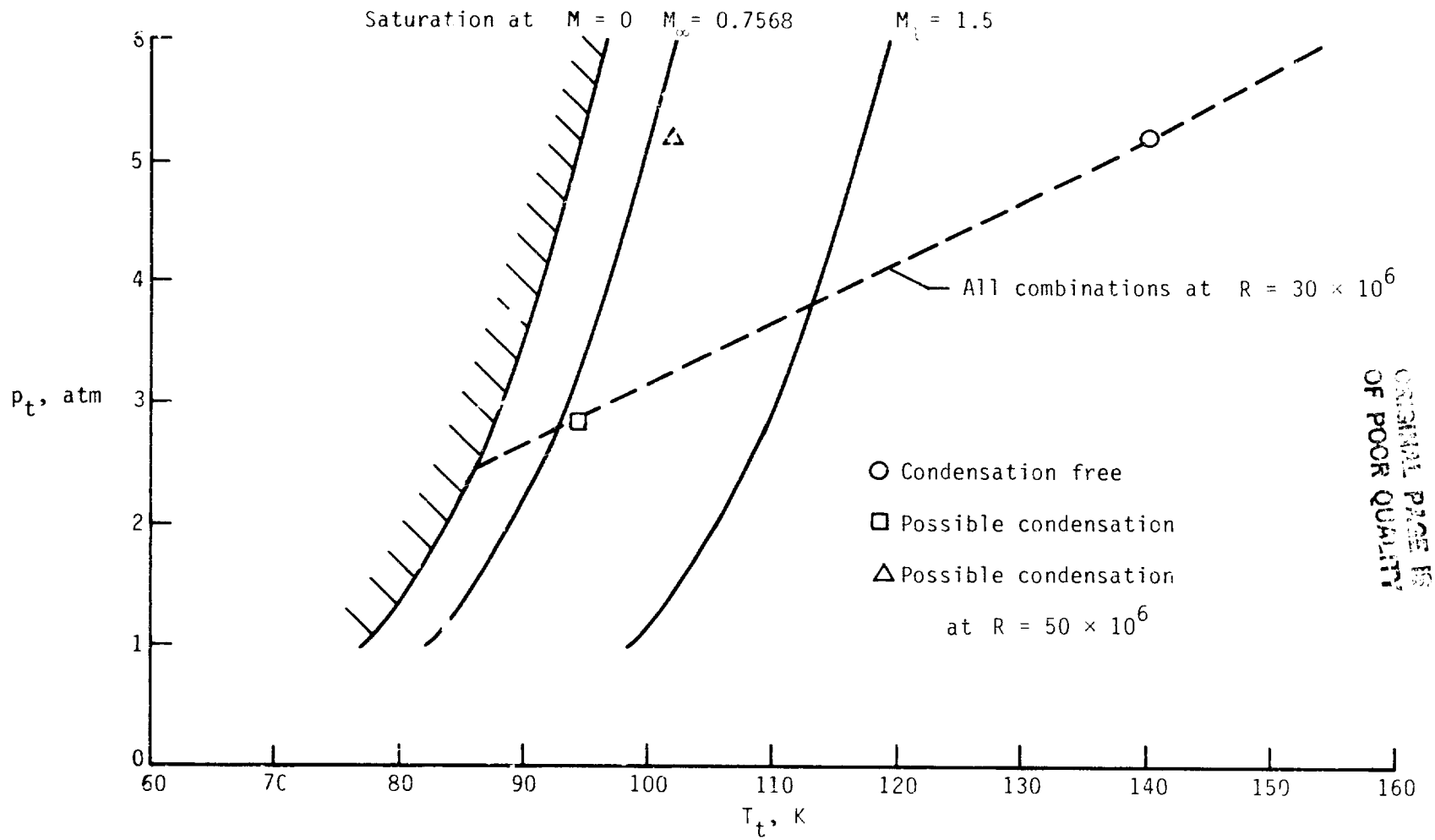

Figure 18.- Saturation curves.

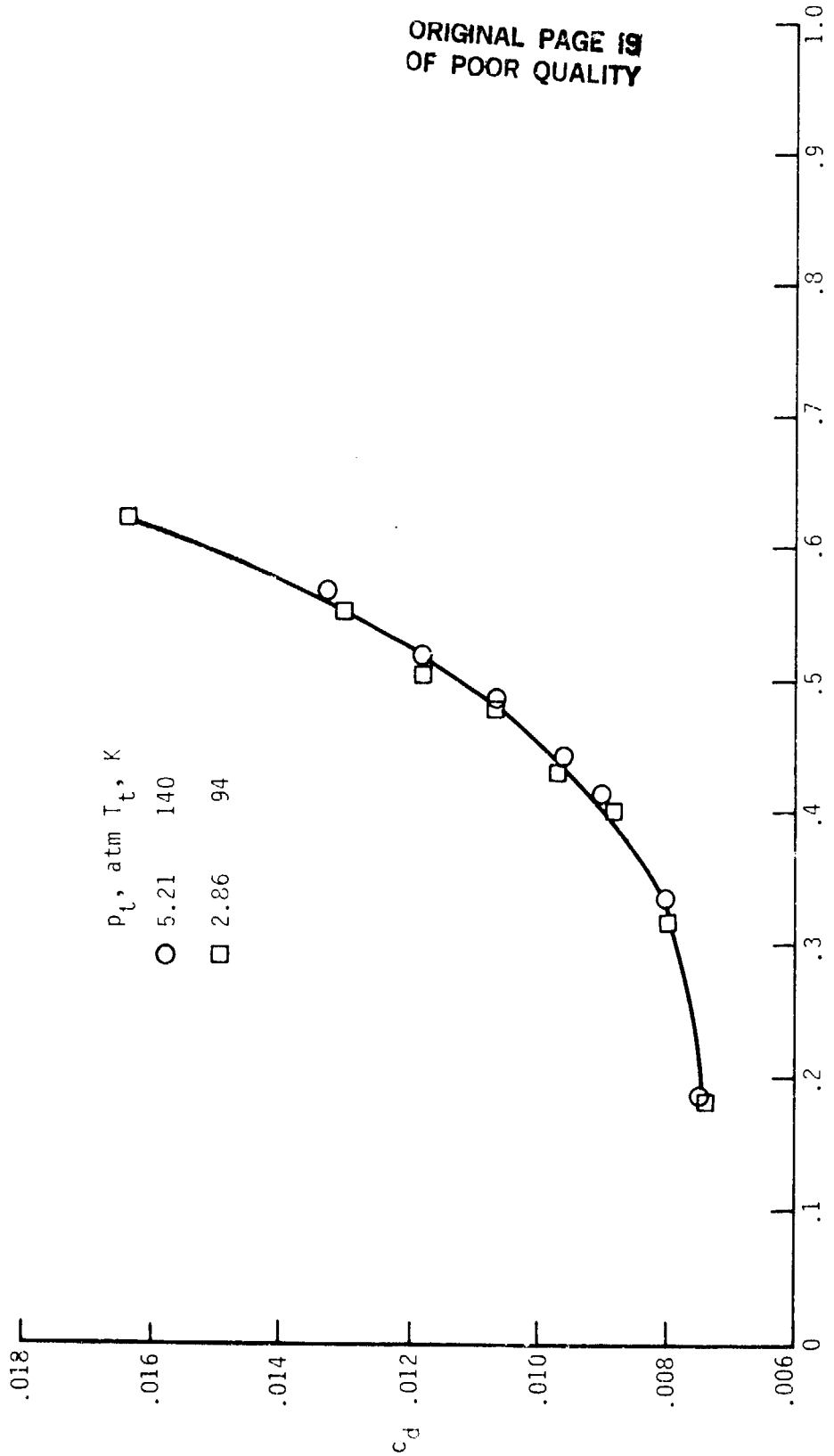

Figure 19.- Drag-force coefficients from a condensation study at $M_\infty = 0.7568$ and $R = 30 \times 10^6$.

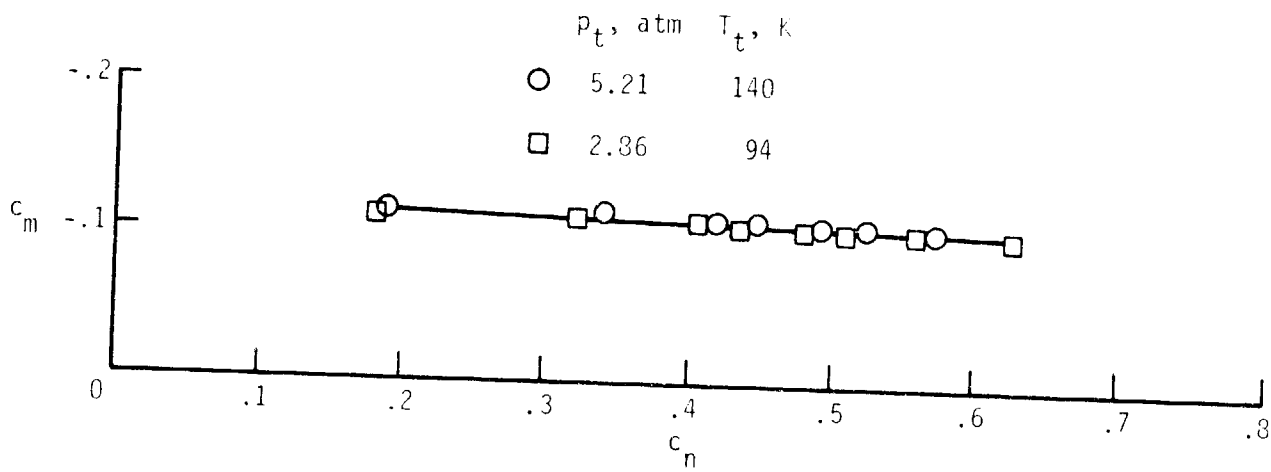

Figure 20.- Pitching-moment coefficients from a condensation study at $M_\infty = 0.7568$ and $R = 30 \times 10^6$.